

ELECTROMAGNETIC MESON PRODUCTION IN THE NUCLEON RESONANCE REGION

V. D. BURKERT

*Thomas Jefferson National Accelerator Facility,
12000 Jefferson Avenue, Virginia 23606, USA
burkert@jlab.org*

T.-S. H. LEE

*Physics Division, Argonne National Laboratory,
Argonne, Illinois 60439, USA
lee@theory.phy.anl.gov*

Received 22 July 2004

Recent experimental and theoretical advances in investigating electromagnetic meson production reactions in the nucleon resonance region are reviewed. We give a description of current experimental facilities with electron and photon beams and present a unified derivation of most of the phenomenological approaches being used to extract the resonance parameters from the data. The analyses of π and η production data and the resulting transition form factors for the $\Delta(1232)P_{33}$, $N(1535)S_{11}$, $N(1440)P_{11}$, and $N(1520)D_{13}$ resonances are discussed in detail. The status of our understanding of the reactions with production of two pions, kaons, and vector mesons is also reviewed.

Keywords: Nucleon resonances; meson production reactions.

1. Introduction

The quest for understanding the structure and interaction of hadrons has been the motivation of strong interaction physics for decades. The advent of Quantum Chromodynamics (QCD)¹ led to a general theoretical description of the strong interaction in terms of the fundamental constituents, quarks and gluons. At very high energies, perturbative methods have proven very effective in the description of many processes. However, because of the complexity of the theory, we are still a long way from being able to describe the strong force as it is manifest in the structure of baryons and mesons. The most fundamental approach to resolve this difficulty is to develop accurate numerical simulations of QCD on the Lattice (Lattice QCD).² Alternatively, hadron models with effective degrees of freedom have been constructed for interpreting data. For example, near threshold pion–pion scattering, pion–nucleon scattering, and pion photoproduction can be successfully described by chiral perturbation theory,³ which is formulated in terms of hadron degrees of free-

dom and constrained only by the symmetry properties of QCD. The constituent quark model^{4,5} is another successful, though not fully understood, example. In some cases, the results from these two different theoretical efforts are complementary in understanding the data and making predictions for future experiments.

For heavy quark systems, Lattice QCD (LQCD) can now predict accurate quantities for interpreting the data from, for example, B meson facilities. For light-quark systems, the small quark masses are difficult to implement, and approximations have been necessary in Lattice QCD calculations. Nevertheless, significant progress has been made in calculating some basic properties of baryons, such as masses of ground states, as well as of low lying excited states.^{6–9} Even the first LQCD calculation of the electromagnetic transition form factors from the ground state proton to the first excited state, the $\Delta(1232)$, has been attempted recently.¹⁰ However, reliable Lattice QCD calculations for electromagnetic meson production reactions, the subject of this paper, seem to be in the distant future. In the foreseeable future, models of hadron structure and reactions will likely continue to play an important role and provide theoretical guidance for experimenters.

The development of hadron models for the nucleon and nucleon resonances (N^*) has a long history. In the past three decades, the constituent quark model has been greatly refined to account for residual quark-quark interactions due to one-gluon-exchange^{4,5} and/or Goldstone boson exchange.^{11,12} Efforts are underway to reformulate the model within the relativistic quantum mechanics.^{13–15} Conceptually completely different models have also been developed, such as bag models,¹⁶ chiral bag models,^{17,18} algebraic models,¹⁹ soliton models,²⁰ color dielectric models,²¹ Skyrme models,²² and covariant models based on Dyson–Schwinger equations.²³ With suitable phenomenological procedures, most of these models are comparable in reproducing the *low-lying* N^* spectra as determined by the amplitude analyses of elastic πN scattering. However they have rather different predictions on the number and ordering of the highly excited N^* states. They also differ significantly in predicting some dynamical quantities such as the electromagnetic and mesonic N – N^* transition form factors. Clearly, accurate experimental information for these N^* observables is needed to distinguish these models. This information can be extracted from the data of electromagnetic meson production reactions. In the past few years, such data with high precision have been extensively accumulated at Thomas Jefferson National Accelerator Facility (JLab), MIT-Bates, and LEGS of Brookhaven National Laboratory in the United States, MAMI of Mainz and ELSA of Bonn in Germany, GRAAL of Grenoble in France, and LEPS of Spring-8 in Japan. In this paper we will review these experimental developments and the status of our understanding of the data accumulated in recent years. Our focus will be on the study of N^* excitations. The use of these data for other investigations will not be covered.

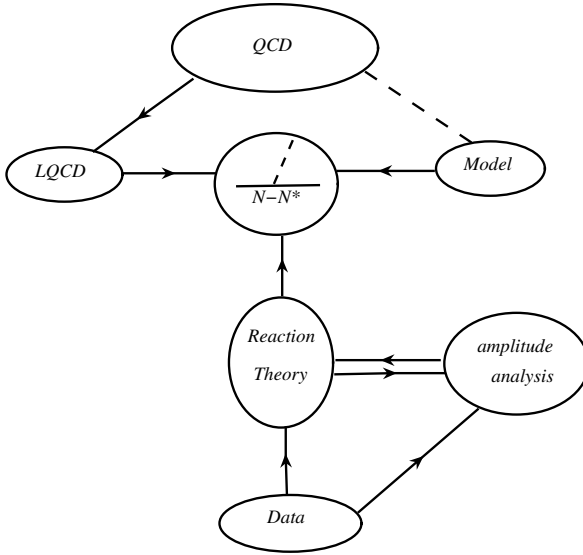
It is useful to briefly describe here the recent advances in using the new data to address some of the long-standing problems in the study of N^* physics. The first is the so-called *missing resonance problem*. This problem originated from the

observation that some of the N^* states predicted by the constituent quark model are not seen in the baryon spectra determined mainly from the amplitude analyses of πN elastic scattering. There are two possible solutions for this problem. First, it is possible that the constituent quark model has wrong effective degrees of freedom of QCD in describing the highly excited baryon states. Other models with fewer degrees of freedom, such as quark-diquark models or models based on alternative symmetry schemes,²⁰⁵ could be more accurate in reproducing the baryon spectra. The second possibility is that these missing resonances do not couple strongly with the πN channel and can only be observed in other processes, as suggested by Isgur and Koniuk¹⁶⁸ in 1980. Data from the experiments measuring as many meson-baryon channels as possible are needed to resolve the missing resonance problem.

The second outstanding problem in the study of N^* physics is that the partial decay widths of baryon resonances compiled and published periodically by the Particle Data Group (PDG) have very large uncertainties in most cases.²⁴ For some decay channels, such as ηN , $K\Sigma$ and ωN , the large uncertainties are mainly due to insufficient data. But the discrepancies between the results from using different amplitude analysis methods is also a source of the uncertainties. This problem can be resolved only with a sufficiently large database that allows much stronger constraints on amplitude analyses, and a strong reduction of the model dependence of the extracted partial decay widths as well as other N^* parameters. This requires that the data must be precise and must cover very large kinematic regions in scattering angles, energies, and momentum transfers. The data of polarization observables must also be as extensive as possible.

The above two experimental challenges have been met with the operations of the electron and photon facilities mentioned above. These facilities are also equipped with sophisticated detectors for measuring not only the dominant single pion channel but also kaon, vector meson, and two-pion channels. The CEBAF Large Acceptance Spectrometer (CLAS) at JLab is the most complete and advanced detector in the field.

The third long-standing problem is in the theoretical interpretations of the N^* parameters listed by the PDG. Most of the model predictions on $N^* \rightarrow \gamma N$ helicity amplitudes are only in a very qualitative agreement with the PDG values. In some cases, they disagree even in signs. One could attribute this to the large experimental uncertainties, as discussed above. However, the well determined empirical values of the simplest and most unambiguous $\Delta \rightarrow \gamma N$ helicity amplitudes are about 40% larger than the predictions from practically all of the hadron models mentioned above. This raises the question about how the hadron models as well as the Lattice QCD calculations are related to the N^* parameters extracted from empirical amplitude analyses. We need to evaluate critically their relationships from the point of view of fundamental reaction theory. The discrepancies in the $\Delta(1232)$ region must be understood before meaningful comparisons between theoretical predictions and empirical values can be made. Much progress has been made in this area. The results, as will be detailed in Sec. 5.1, strongly indicate that it is necessary

Fig. 1. Scheme for N^* study

to apply an appropriate reaction theory in making meaningful comparisons of the empirical values from amplitude analyses and the predictions from hadron models and LQCD.

Summing up the above discussions, it is clear that in the absence of a fundamental solution of QCD in the resonance regions, the study of N^* excitations needs close collaborations between theoretical and experimental efforts. This is illustrated in Fig. 1. On the theoretical side, we need to use Lattice QCD calculations and/or hadron structure models to predict properties of nucleon resonances, such as the $N-N^*$ transition form factors indicated in Fig. 1. On the experimental side, we need to accumulate sufficiently extensive and precise data of meson production reactions. We then must develop reaction models for interpreting the data in terms of hadron structure calculations. The development of empirical amplitude analyses of the data is an important part of this task.

In Sec. 2, the current experimental facilities will be reviewed. The general formulation for calculating cross-sections of electromagnetic meson production is presented in Sec. 3. Section 4 is devoted to providing a unified derivation of models used in the interpretation of the data. Results are presented in Sec. 5. Concluding remarks and the outlook are given in Sec. 6.

2. Experimental Facilities

2.1. Thomas Jefferson National Accelerator Facility

The Thomas Jefferson National Accelerator Facility (JLab) in Newport News, Virginia, operates a CW electron accelerator with energies in the range up to 6 GeV.²⁷

Three experimental Halls receive highly polarized electron beams with the same, or with different but correlated energies, simultaneously. Beam currents in the range from 0.1 nA to 150 μ A can be delivered to the experiments, simultaneously.

2.1.1. *Experimental Hall A — HRS²*

Hall A houses a pair of identical focussing magnetic spectrometers²⁸ with high resolution (HRS²), each with a momentum resolution of $\Delta p/p \sim 2 \times 10^{-4}$; one of them is instrumented with a gas Cerenkov counter and a shower counter for the identification of electrons. The hadron arm is instrumented with a proton recoil polarimeter. The detector package allows identification of charged pions, kaons, and protons. A polarized ³He target is used for experiments that require polarized neutron targets. The HRS² spectrometers have been used to measure the reaction $\bar{e}p \rightarrow e\bar{p}\pi^0$ in the $\Delta(1232)$ region and to extract various single and double polarization response functions.

2.1.2. *Experimental Hall B — CLAS*

Hall B houses the CEBAF Large Acceptance Spectrometer (CLAS) detector, and a photon energy tagging facility.²⁹ CLAS can be operated with electron beams and with energy tagged photon beams. The photon beam can be either unpolarized or can be linearly or circularly polarized. The detector system was designed specifically with the detection of multiple particle final states in mind. The driving motivation for the construction of CLAS was the nucleon resonances (N^{*}) program, with the emphasis on the study of the γNN^* and $\gamma N\Delta^*$ transition form factors, and the search for *missing resonances*. Figure 2 shows the CLAS detector. At the core of the detector is a toroidal magnet consisting of six superconducting coils symmetrically arranged around the beam line. Each of the six sectors is instrumented as an independent spectrometer with 34 layers of tracking chambers allowing for the full reconstruction of the charged particle 3-momentum vectors. Charged hadron identification is accomplished by combining momentum and time-of-flight, and the measured path length from the target to the plastic scintillation counters which surround the entire tracking chambers. Timing resolutions of $\Delta T = 120\text{--}200$ psec (rms) are achieved, depending on the length of the scintillator bar, which ranges from 30 cm to 350 cm. Mass and charge number (Z) reconstruction is shown in the left panel of Fig. 3. Protons and pions can be separated for momenta up to 4 GeV/ c , and pions and kaons up to about 2 GeV/ c . The wide range of particle identification allows to study the complete range of reactions relevant to the N^{*} program. In the polar angle range of up to 70° photons and neutrons can be detected using the electromagnetic calorimeters. The forward angular range from about 10° to 50° is instrumented with gas Cerenkov counters for the identification of electrons.

In the N^{*} program, CLAS is often used as a “missing mass” spectrometer, where all final state particles except one particle are detected. The undetected particle is

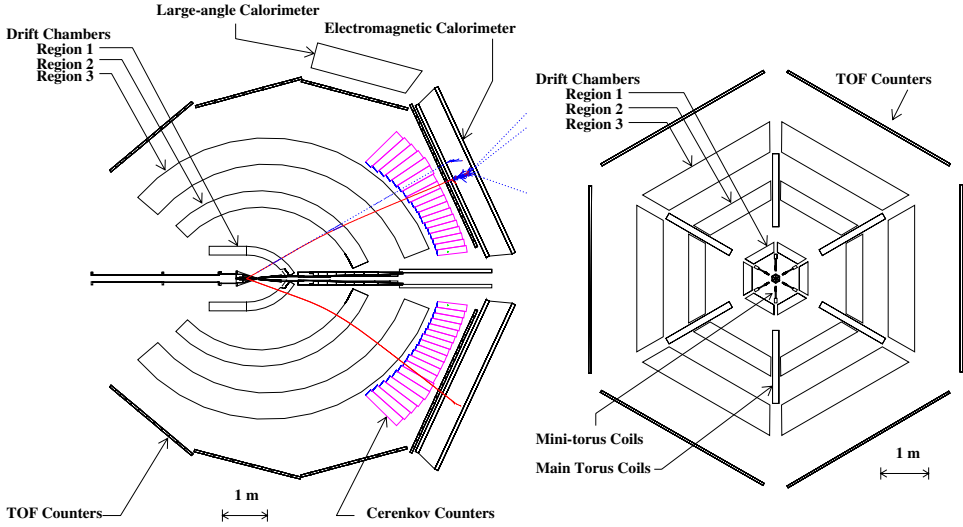


Fig. 2. The CLAS detector at JLab. Left panel: The longitudinal cut along the beam line shows the three drift chamber regions, the Cherenkov counter at forward angles, the time-of-flight (TOF) system, and the electromagnetic calorimeters. A simulated event shows an electron (upper) and a positively charged hadron. Right panel: Transverse cut through CLAS. The six superconducting coils provide a six sector structure with independent detectors. A polarized target can be inserted into the large bore near the center.

inferred through the overdetermined kinematics, making use of the good momentum and angle resolution. The right panel in Fig. 3 shows an example of the kinematics covered in the reaction $ep \rightarrow epX$. It shows the invariant hadronic mass W versus the missing mass M_X . The undetected particles π^0 , η , and ω are clearly visible as bands of constant M_X . The correlation of certain final states with specific resonance excitations is also clearly seen.

2.1.3. *Experimental Hall C — HMS and SOS*

Hall C houses the high momentum spectrometer (HMS) and the short orbit spectrometer (SOS). The HMS reaches a maximum momentum of 7 GeV/ c , while the SOS is limited to about 1.8 GeV/ c . The spectrometer pair has been used to measure the $\gamma^*N\Delta(1232)$ and $\gamma^*NN^*(1535)$ transition at high Q^2 values. For these kinematics the SOS was used as electron spectrometer and the HMS to detect the proton. To achieve a large kinematics coverage, the spectrometers have to be moved in angles, and the spectrometer optics has to be adjusted to accommodate different particle momenta. This makes such a two spectrometer setup most useful for studying meson production at high momentum transfer, or close to threshold. In either case, the Lorentz boost guarantees that particles are produced in a relatively narrow cone around the virtual photon, and can be detected in magnetic spectrometers with relatively small solid angles.

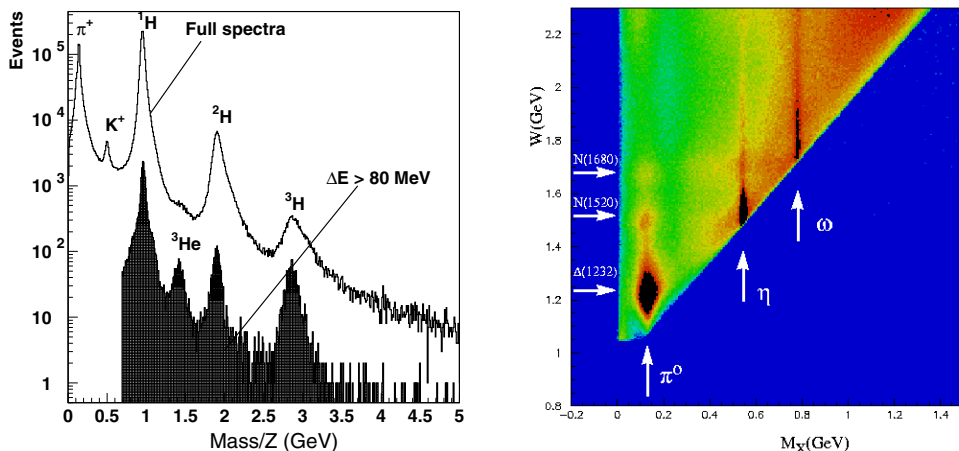


Fig. 3. Left panel: Charged particle identification in CLAS. The reconstructed mass/ Z (charge number) for positive tracks from a carbon target is shown. Additional sensitivity to high-mass particles is obtained by requiring large energy loss in the scintillators (shaded histogram). Right panel: Invariant mass versus missing mass for $ep \rightarrow epX$ at an electron beam energy of 4 GeV.

2.2. MAMI-B

The MAMI-B microtron electron accelerator³⁰ at Mainz in Germany reaches a maximum beam energy of 850 MeV. There are experimental areas for electron scattering experiments with three focussing magnetic spectrometers with high resolution.³¹ A two-spectrometer configuration has been used in cross-section and polarization asymmetry measurements of π^0 electroproduction from protons in the $\Delta(1232)$ region.

Another experimental area is equipped for physics with an energy-tagged photon bremsstrahlung beam.³² Experimental setups with BaF_2 crystals (TAPS) have been employed for measurements of differential cross-sections for π^0 and η production and for beam asymmetry measurements using a linearly polarized coherent bremsstrahlung beam.

2.3. MIT-Bates

The Bates 850 MeV linear electron accelerator has been used to study π^0 production in the $\Delta(1232)$ region using an out-of-plane spectrometer setup.³³ A set of four independent focussing spectrometers was used to measure various response functions, including the beam helicity-dependent out-of-plane response function. Because of the small solid angles covered by this setup, a limited range of the polar angles in the center of mass frame of the $p\pi^0$ subsystem could be covered. These spectrometers are no longer in use, but data are still being analyzed.

2.4. *Laser backscattering photon facilities*

Electron storage rings built as light sources for material science studies are often used parasitically to produce high energy photons for nuclear physics applications. An intense laser beam is directed tangentially at the electron beam circulating in the storage ring producing high energy Compton backscattered photons in an energy range dependent upon the wavelength of the laser light. While the photon intensities are quite modest, the energy spectrum is peaked at the high energy end providing an efficient source of high energy photons for nuclear physics experiments. The laser light is easily polarized linearly or circularly. In the Compton backscattering process the polarization of the laser light is transferred to the high energy photon beam providing a convenient source of polarized photons.

2.4.1. *The Graal tagged photon facility*

The Grenoble Synchrotron Light Source facility is used to generate a laser backscattered polarized photon beam of up to 1470 MeV energy for nuclear physics applications. A BGO crystal detector is used for the detection of photons³⁴ covering a large portion of 4π . Multi-wire proportional chambers allow charged particle tracking. Particle identification is achieved by time-of-flight measurements at forward angles, and by energy loss measurements at large angles. The large solid angle coverage allows the study of reactions with multiple photons in the final state which is important for nucleon resonance studies in π^0 and η production.³⁵

2.4.2. *The LEGS at Brookhaven National Laboratory*

Brookhaven National Laboratory operates an electron synchrotron as a light source with an energy of 2.8 GeV/c. A laser backscattered real photon beam with an energy up to 470 MeV is used for nuclear physics experiments.³⁶ A tagging system measures the energy of the Compton-scattered electron from which the photon energy is inferred. The photon beam is used with an unpolarized hydrogen or nuclear target, and with a polarized HD target.³⁷ Several arrays of NaI(Tl) crystal detectors have been used to measure Compton scattering and π^0 production off protons in the $\Delta(1232)$ region.

2.4.3. *LEPS at Spring-8*

Spring-8 operates an 8 GeV electron synchrotron near Osaka in Japan. A laser-backscattered, energy-tagged polarized photon beam with an energy up to 2.4 GeV is produced for nuclear and particle physics applications.³⁸ The LEPS detector consists of a plastic scintillator to detect charged particles produced in the target, an aerogel Cerenkov counter for particle identification, charged-particle tracking counters, a large dipole magnet, and a time-of-flight wall for particle identification.

The LEPS detector has been used for ω , and near-threshold ϕ production, and for strange particle production.

2.5. *Electron stretcher and accelerator (ELSA)*

The University of Bonn operates a 2.5 GeV electron synchrotron and a stretcher ring and post accelerator to obtain a high duty factor beam and an energy of 3 GeV. Three experimental setups have been used for meson production experiments during the past decade.

2.5.1. *The SAPHIR detector*

SAPHIR is a large acceptance detector with 2π azimuthal coverage. An external electron beam was used to generate an energy-tagged real photon beam for experiments with the SAPHIR detector.³⁹ At the core of the detector is a large-gap dipole magnet. Tracking is provided by a central drift chamber located inside the dipole magnet, and additional chambers outside the magnetic field region. Scintillation counters are used for triggering and to provide time-of-flight information for particle identification.

2.5.2. *The Crystal Barrel detector at ELSA*

The Crystal Barrel (CB-ELSA) detector was originally used at the LEAR $p\bar{p}$ ring at CERN. The detector was recently brought to ELSA for operation in an energy-tagged bremsstrahlung photon beam.⁴⁰ The detector consists of CsI crystals providing nearly full solid angle coverage for neutral particle detection. The main focus is the detection of multiple neutral particle final states.

2.5.3. *The Elan apparatus*

The Elan apparatus has been used for studies of single pion electroproduction in the $\Delta(1232)$ region. A focussing magnetic spectrometer detects the scattered electrons, and electromagnetic shower detectors measure photons from π^0 decays. Protons and charged pions are detected as well. Charged hadrons are not magnetically analyzed. This setup has been used for measurements of π^0 and π^+ in the $\Delta(1232)$ region.

3. General Formalism

The bulk of data from the facilities described in the previous section are from experiments with a single meson and baryon in the final state. We therefore only present the formulation for such reactions. The generalization of the formulation to the cases that the final states are three-body states is straightforward.

We consider the process $N(e, e'M)B$ illustrated in Fig. 4. The final meson-baryon states are two-body states, such as $\pi N, \eta N, K\Lambda, \omega N$ and ϕN . Within Relativistic

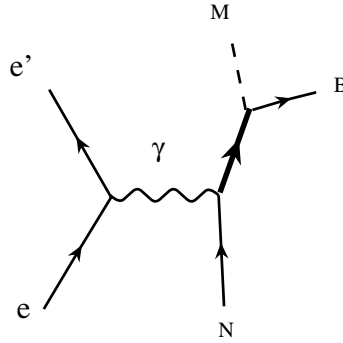


Fig. 4. One-photon exchange mechanism for meson electroproduction from a nucleon.

Quantum Field Theory, the Hamiltonian density for describing this process can be concisely written as

$$H_{em}(x) = eA_\mu(x)[j^\mu(x) + J^\mu(x)], \tag{1}$$

where A_μ is the photon field, and

$$j^\mu(x) = \bar{\psi}_e(x)\gamma^\mu\psi_e(x) \tag{2}$$

is the lepton current, and the electromagnetic interactions involving hadrons are induced by the hadron current J^μ .

With the convention of Bjorken and Drell,⁴¹ the Hamiltonian density Eq. (1) leads to

$$\langle kp' | \int dx A^\mu(x) J_\mu(x) | qp \rangle = (2\pi)^4 \delta^4(p + q - k - p') \langle kp' | \epsilon_\mu(q) J^\mu(0) | qp \rangle, \tag{3}$$

where q , p , k , and p' are the momenta for the initial photon, initial nucleon, final meson, and final nucleon, respectively, $\epsilon_\mu(q)$ is the photon polarization vector. Throughout this paper, we will suppress the spin and isospin indices unless they are needed for detailed explanations.

It is convenient to write

$$\begin{aligned} \langle kp' | \epsilon_\mu(q) J^\mu(0) | qp \rangle &= \frac{1}{(2\pi)^6} \sqrt{\frac{m_N}{E_N(p')}} \frac{1}{\sqrt{2E_\pi(k)}} \epsilon_\mu(q) J^\mu(k, p'; q, p) \\ &\times \sqrt{\frac{m_N}{E_N(p)}} \frac{1}{\sqrt{2\omega}}. \end{aligned} \tag{4}$$

The expression for calculating electromagnetic meson production cross-sections can be expressed in terms of $J^\mu(k, p'; q, p)$. For evaluating electroproduction cross-sections, it is common and convenient to choose a coordinate system that the virtual photon is in the quantization z -direction, and the angle between the e - e' plane and M - B plane is ϕ_M , as illustrated in Fig. 5. With some straightforward but lengthy

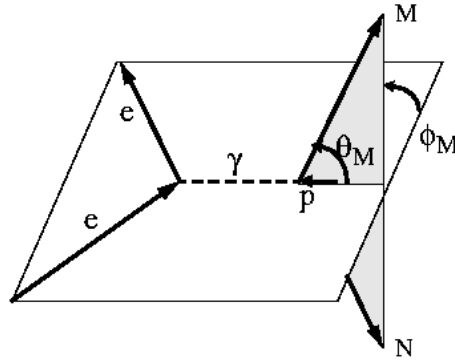


Fig. 5. Kinematics of meson electroproduction reaction.

derivations, it is possible to write the differential cross-section of $N(\bar{e}, e'M)B$ reaction in the following form:

$$\frac{d^5\sigma_h}{dE_{e'}d\Omega_{e'}d\Omega_M^*} = \Gamma \frac{d\sigma_h}{d\Omega_M^*}$$

with

$$\frac{d\sigma_h}{d\Omega_M^*} = \left[\frac{d\sigma_{\text{unpol}}}{d\Omega_M^*} + h\sqrt{2\epsilon(1-\epsilon)} \frac{d\sigma_{LT'}}{d\Omega_M^*} \sin\phi_M \right], \quad (5)$$

where h is the helicity of the incoming electron. The kinematic factors associated with the incoming and outgoing electrons are only contained in the following two variables

$$\epsilon = \left\{ 1 + \frac{2|\mathbf{q}|^2}{Q^2} \tan^2 \frac{\theta_e}{2} \right\}^{-1}, \quad (6)$$

$$\Gamma = \frac{\alpha K_H}{2\pi^2 Q^2} \frac{E'_e}{E_e} \frac{1}{1-\epsilon}, \quad (7)$$

where $K_H = \omega - Q^2/2m_N$ is the virtual photon flux, $\alpha = 1/137$ is the electromagnetic coupling constant, $q^\mu = (\omega, \mathbf{q})$ is the momentum of the photon, and $Q^2 = -q^2 = |\mathbf{q}|^2 - \omega^2$. The incident and outgoing electron energies are related to q^μ by

$$\omega = E_e - E'_e, \quad (8)$$

$$Q^2 = 4E_e E'_e \sin^2 \frac{\theta_e}{2}, \quad (9)$$

where θ_e is the angle between the incident and outgoing electrons.

For investigating N^* excitations, the kinematics is often characterized by the initial γ^*N invariant mass W and Q^2 . For such a choice, the energy transfer is then defined by

$$\omega = \frac{W^2 + Q^2 - m_N^2}{2m_N}. \quad (10)$$

The corresponding electron kinematics for conducting experiments with a given (Q^2, W) can then be evaluated by using Eqs. (8) and (9).

Note that the differential cross-sections in the right-hand side of Eq. (5) are defined in the center of mass (c.m.) frame of the initial γ^*N and the final MB systems. These quantities must be evaluated in terms of the momenta in that c.m. frame. For the coordinate system chosen as $\mathbf{q} \parallel \hat{z}$, all momenta needed in calculating $d\sigma/d\Omega_M^*$ must be transformed by a Lorentz boost with $\beta = \hat{z}|\mathbf{q}|/(\omega + m_N)$. In terms of variables W and Q^2 , a momentum p_c^μ in the considered c.m. frame is related to a momentum p^μ in the laboratory frame by

$$p_c^0 = \frac{m_N + \omega}{W} p^0 - \frac{|\mathbf{q}|}{W} p^z, \quad (11)$$

$$p_c^x = p^x, \quad (12)$$

$$p_c^y = p^y, \quad (13)$$

$$p_c^z = -\frac{|\mathbf{q}|}{W} p^0 + \frac{m_N + \omega}{W} p^z. \quad (14)$$

Specifically, we have for the virtual photon:

$$|\mathbf{q}_c| = \frac{m_N}{W} |\mathbf{q}|, \quad (15)$$

$$\omega_c = \frac{\omega m_N - Q^2}{W}. \quad (16)$$

It is easy to see that $Q^2 = \mathbf{q}^2 - \omega^2 = \mathbf{q}_c^2 - \omega_c^2$.

We next present formulae for calculating the c.m. differential cross-sections in the right-hand-side of Eq. (5). The unpolarized cross-section is given by

$$\frac{d\sigma_{\text{unpol}}}{d\Omega_M^*} = \frac{d\sigma_T}{d\Omega_M^*} + \epsilon \frac{d\sigma_L}{d\Omega_M^*} + \epsilon \frac{d\sigma_{\text{TT}}}{d\Omega_M^*} \cos 2\phi_M + \sqrt{2\epsilon(1+\epsilon)} \frac{d\sigma_{\text{LT}}}{d\Omega_M^*} \cos \phi_M, \quad (17)$$

where σ_T , σ_L , σ_{TT} , and σ_{LT} are called the transverse, longitudinal, polarization, and interference cross-sections. These four cross-sections and the $d\sigma_{\text{LT}'}/d\Omega^*$ in Eq. (5) can be written as

$$\frac{d\sigma_\beta}{d\Omega_M^*} = \frac{|\mathbf{k}_c|}{q_c^\gamma} M_\beta(k_c, p'_c; q_c, p_c), \quad (18)$$

where $q_c^\gamma = (W^2 - m_N^2)/(2m_N) = K_H$ is the effective photon c.m. momentum, $\beta = T, L, \text{TT}, \text{LT}$ and LT' , and the c.m. momenta k_c, p'_c, q_c , and p_c can be calculated

from the corresponding momenta in the laboratory frame by using Eqs. (11)–(14). Obviously $q_c^\gamma = |\mathbf{q}_c|$ at the photon point $Q^2 = 0$.

The meson production dynamics is contained in M_β of Eq. (18). They are calculated from various combinations of current matrix elements evaluated on the $\phi_M = 0$ plane (see Fig. 5):

$$\begin{aligned}
 M_T(k_c, p'_c; q_c, p_c) &= \frac{F}{4} \sum_{\text{spins}} [|J^x(k_c, p'_c; q_c, p_c)|^2 + |J^y(k_c, p'_c; q_c, p_c)|^2]_{\phi_M=0} \\
 M_L(k_c, p'_c; q_c, p_c) &= \frac{F}{2} \sum_{\text{spins}} \frac{Q^2}{\omega^2} [|J^z(k_c, p'_c; q_c, p_c)|^2]_{\phi_M=0} \\
 M_{TT}(k_c, p'_c; q_c, p_c) &= \frac{F}{4} \sum_{\text{spins}} [|J^x(k_c, p'_c; q_c, p_c)|^2 - |J^y(k_c, p'_c; q_c, p_c)|^2]_{\phi_M=0} \\
 M_{LT}(k_c, p'_c; q_c, p_c) &= -\frac{F}{2} \sum_{\text{spins}} \sqrt{\frac{Q^2}{\omega^2}} \text{Re}\{ J^z(k_c, p'_c; q_c, p_c) J^{x*}(k_c, p'_c; q_c, p_c) \}_{\phi_M=0} \\
 M_{LT'}(k_c, p'_c; q_c, p_c) &= \frac{F}{2} \sum_{\text{spins}} \sqrt{\frac{Q^2}{\omega^2}} \text{Im}\{ J^z(k_c, p'_c; q_c, p_c) J^{x*}(k_c, p'_c; q_c, p_c) \}_{\phi_M=0}
 \end{aligned} \tag{19}$$

with

$$F = \frac{e^2}{(2\pi)^2} \frac{1}{2E_M(k_c)} \frac{m_B}{E_B(p'_c)} \frac{m_N}{E_N(p_c)} \frac{E_M(k_c)E_B(p'_c)}{2W} \tag{20}$$

where $E_a(p) = \sqrt{\mathbf{p}^2 + m_a^2}$ with m_a denoting the mass of particle a .

The differential cross-sections of $N(\bar{e}, e'M)B$ are often expressed in terms of response functions⁴² R_α which are related to the differential cross-sections of Eq. (18) by

$$\begin{aligned}
 \frac{d\sigma_T}{d\Omega_M^*} &= \frac{|\mathbf{k}_c|}{q_c^\gamma} R_T, \\
 \frac{d\sigma_{TT}}{d\Omega_M^*} &= \frac{|\mathbf{k}_c|}{q_c^\gamma} R_{TT}, \\
 \frac{d\sigma_L}{d\Omega_M^*} &= \frac{|\mathbf{k}_c|}{q_c^\gamma} \frac{Q^2}{\omega_c^2} R_L, \\
 \frac{d\sigma_{LT}}{d\Omega_M^*} &= \frac{|\mathbf{k}_c|}{q_c^\gamma} \sqrt{\frac{Q^2}{\omega_c^2}} R_{LT}, \\
 \frac{d\sigma_{LT'}}{d\Omega_M^*} &= \frac{|\mathbf{k}_c|}{q_c^\gamma} \sqrt{\frac{Q^2}{\omega_c^2}} R_{LT'}.
 \end{aligned} \tag{21}$$

The above formulation can be readily used to calculate various polarization observables with a polarized initial nucleon. For observables with a polarized recoiled final baryon, the situation is more complicated. They have been explicitly derived for pseudo-scalar meson production.^{43,44} Formulations for analyzing spin observables of vector meson production were developed in Ref. 45.

We also note that the unpolarized photoproduction cross-section is given by $d\sigma_T/d\Omega_M^*$ evaluated at $Q^2 = 0$ and $q_C^\gamma \rightarrow |\mathbf{q}_C|$. For polarized photons, one needs to choose an appropriate combination of J^x and J^y . For instance, $d\sigma_\perp/d\Omega_M^*$ ($d\sigma_\parallel/d\Omega_M^*$) for the photon polarization normal (parallel) to the hadron plane is calculated from keeping only J^y (J^x) contribution and multiplying the resulting cross-section by a factor of two. The photon asymmetry is defined as

$$\Sigma_\gamma = \frac{\sigma_\perp - \sigma_\parallel}{\sigma_\perp + \sigma_\parallel}. \quad (22)$$

Calculations of other photoproduction polarization observables are given, for example, in the Appendix C of Ref. 66.

We next present formulae which are often used in analyzing the production of pseudo-scalar mesons, such as MB = π N, η N, KY. The Lorentz invariance and gauge invariance allow us to write the hadron current matrix elements as

$$\epsilon_\mu(q)J^\mu(k, p'; q, p) = \sum_{i=1,6} \bar{u}(\mathbf{p}')A_i(s, t, u)M_i]u(\mathbf{p}), \quad (23)$$

where $u(\mathbf{p})$ is the Dirac spinor, $A_i(s, t, u)$ are Lorentz invariant functions, and M_i are independent invariances formed from γ^μ , γ_5 , and momenta variables. The expressions for M_i are irrelevant to this paper and hence are omitted here. But they can be found, for example, on page 5 of Ref. 46. For π production, the amplitudes defined above can be further classified by isospin quantum numbers. There are $A^{(0)}$ for the isoscalar photon, and for the isovector the two amplitudes $A^{(1/2)}$ and $A^{(3/2)}$ for the final π N system with total isospin $I = 1/2$ and $I = 3/2$, respectively. Each invariant amplitude in Eq. (23) can be expanded as

$$A_i = \frac{1}{2}A_i^{(-)}[\tau_\alpha, \tau_3] + A_i^{(+)}\delta_{\alpha,3} + A_i^{(0)}\tau_\alpha, \quad (24)$$

where τ is the isospin Pauli operator, and α is the isospin quantum number associated with the produced pion. Equation (24) then leads to $A_i^{(1/2)} = A_i^{(+)} + 2A_i^{(-)}$ and $A_i^{(3/2)} = A_i^{(+)} - A_i^{(-)}$. It is useful to further define proton ${}_pA^{(1/2)}$ and neutron ${}_nA^{(1/2)}$ amplitudes with total isospin $I = 1/2$:

$$\begin{aligned} {}_pA_i^{(1/2)} &= A_i^{(0)} + \frac{1}{3}A_i^{(1/2)}, \\ {}_nA_i^{(1/2)} &= A_i^{(0)} - \frac{1}{3}A_i^{(1/2)}. \end{aligned} \quad (25)$$

Then the amplitudes for four physical processes can be written as

$$\begin{aligned}
 A_i(\gamma^* p \rightarrow n\pi^+) &= \sqrt{2} \left[{}_p A_i^{(1/2)} - \frac{1}{3} A_i^{(3/2)} \right], \\
 A_i(\gamma^* p \rightarrow n\pi^0) &= {}_p A_i^{(1/2)} + \frac{2}{3} A_i^{(3/2)}, \\
 A_i(\gamma^* n \rightarrow n\pi^-) &= \sqrt{2} \left[{}_n A_i^{(1/2)} + \frac{1}{3} A_i^{(3/2)} \right], \\
 A_i(\gamma^* n \rightarrow n\pi^0) &= -{}_n A_i^{(1/2)} + \frac{2}{3} A_i^{(3/2)}.
 \end{aligned} \tag{26}$$

The above invariant functions $A_i^{(\pm,0)}$ are the starting point for developing dispersion relation approach which will be given in Sec. 4.7. The isospin relations Eqs. (24)–(26) are valid for all of the amplitudes we are going to discuss. However, the isospin quantum numbers as well as spin quantum numbers will be suppressed in the remainder of this article.

For investigating nucleon resonances, it is useful to have a formulation expressing the meson production cross-sections in terms of multipole amplitudes. If the final hadron state consists of only a pseudo-scalar and a spin 1/2 baryon, such as πN , KY and ηN states, such a formulation has been well developed. This is accomplished by casting Eq. (23) into the Chew, Goldberger, Low and Nambu (CGLN)⁴⁷ form defined in the c.m. frame of the final meson–baryon system:

$$\epsilon^\mu J^\mu(k_c, p'_c; q_c, p_c) = \sum_{i=1,6} F_i(s, t, Q^2) \bar{u}(\mathbf{p}_c') O_i u(\mathbf{p}_c), \tag{27}$$

where $F_i(s, t, u)$ are the Lorentz invariant CGLN amplitudes and O_i are operators defined in the baryon spin space:

$$O_1 = i\sigma \cdot \mathbf{b}, \tag{28}$$

$$O_2 = \sigma \cdot \hat{\mathbf{k}}_c \sigma \cdot (\hat{\mathbf{q}} \times \mathbf{b}), \tag{29}$$

$$O_3 = i\sigma \cdot \hat{\mathbf{q}}_c \hat{\mathbf{k}}_c \cdot \mathbf{b}, \tag{30}$$

$$O_4 = i\sigma \cdot \hat{\mathbf{k}}_c \hat{\mathbf{k}}_c \cdot \mathbf{b}, \tag{31}$$

$$O_5 = -i\sigma \cdot \hat{\mathbf{k}}_c b_0, \tag{32}$$

$$O_6 = -i\sigma \cdot \hat{\mathbf{q}}_c b_0, \tag{33}$$

with

$$b^\mu = \epsilon^\mu(q_c) - \frac{\vec{\epsilon} \cdot \vec{q}_c}{|\mathbf{q}_c|} q_c^\mu. \tag{34}$$

Obviously we have $\mathbf{b} \cdot \mathbf{q}_c = 0$. The CGLN amplitudes $F_i(s, t, Q^2)$ can be expanded in terms of multipole amplitudes characterized by the angular momentum quantum numbers of the initial γ^*N and the final MB systems. The relations are found to be

$$F_1 = \sum_{\ell} [P'_{\ell+1}(x)E_{\ell+} + P'_{\ell-1}(x)E_{\ell-} + P'_{\ell+1}(x)M_{\ell+} + (\ell + 1)P'_{\ell-1}(x)M_{\ell-}], \quad (35)$$

$$F_2 = \sum_{\ell} [(\ell + 1)P'_{\ell}(x)M_{\ell+} + \ell P'_{\ell}(x)M_{\ell}], \quad (36)$$

$$F_3 = \sum_{\ell} [P''_{\ell+1}(x)E_{\ell+} + P''_{\ell-1}(x)E_{\ell-} - P''_{\ell+1}(x)M_{\ell+} + P''_{\ell-1}(x)M_{\ell-}], \quad (37)$$

$$F_4 = \sum_{\ell} [-P''_{\ell}(x)E_{\ell+} - P''_{\ell}(x)E_{\ell-} + P''_{\ell}(x)M_{\ell+} - P''_{\ell}(x)M_{\ell-}], \quad (38)$$

$$F_5 = \sum_{\ell} [-(\ell + 1)P'_{\ell}(x)S_{\ell+} + \ell P'_{\ell}(x)S_{\ell-}], \quad (39)$$

$$F_6 = \sum_{\ell} [(\ell + 1)P'_{\ell+1}(x)S_{\ell+} - \ell P'_{\ell-1}(x)S_{\ell-}]. \quad (40)$$

In the above equations, the multipole amplitudes $E_{\ell\pm}$, $M_{\ell\pm}$ and $S_{\ell\pm}$ are functions of W and Q^2 only. They describe the transitions which can be classified according to the character of the photon, transverse or scalar (or longitudinal), and the total angular momentum $J = \ell \pm 1/2$ of the final state. In addition, the transverse photon states can either be electric with parity $(-1)^{L_\gamma}$, or magnetic, with parity $(-1)^{L_\gamma+1}$, where L_γ is the orbital angular momentum of the γ^*N system. In Table 1, we list how each multipole amplitude with $J \leq 3/2$ is related to the initial L_γ and final (ℓ, J) angular momentum quantum numbers. The longitudinal multipoles are related to the scalar multipoles by $L_{\ell\pm} = (\omega/|\mathbf{q}|)S_{\ell\pm}$.

We now note that the matrix elements J^i with $i = x, y, z$ for evaluating Eq. (19) can be obtained from Eq. (27) by setting $\epsilon^\mu = (0, \hat{x})$, $\epsilon^\mu = (0, \hat{y})$, $\epsilon^\mu = (0, \hat{z})$, respectively. By further using the relations Eqs. (35)–(40), the differential cross-

Table 1. Angular momentum quantum numbers associated with $\gamma^*N \rightarrow \pi N$ multipole amplitudes. See text for the explanations.

ℓ	J	L_γ	Notation
0	1/2	1	E_{0+}
1	3/2	2	E_{1+}
1	1/2	1	M_{1-}
1	3/2	1	M_{1+}
0	1/2	1	S_{0+}
1	1/2	0	S_{1-}
1	3/2	2	S_{1+}

sections Eq. (5) or Eq. (18) can then be expressed in terms of multipole amplitudes. For example, Eq. (5) can lead to the total inclusive cross-section:

$$\frac{d\sigma}{dE'_e d\Omega'_e} = \Gamma \left[\sigma_T + \frac{Q^2}{|\mathbf{q}|^2} \epsilon \sigma_L \right], \quad (41)$$

where

$$\begin{aligned} \sigma_T &= \frac{2\pi k_c}{|\mathbf{q}_c|} \sum_{\ell} \ell(\ell+1) [|M_{\ell+}|^2 + |E_{(\ell+1)-}|^2 + \ell^2(\ell+1) [|M_{\ell-}|^2 + |E_{(\ell-1)+}|^2]] \\ \sigma_L &= \frac{4\pi k_c}{|\mathbf{q}_c|} \sum_{\ell} [(\ell+1)^3 |L_{(\ell+1)-}|^2 + \ell^3 |L_{(\ell-1)+}|^2]. \end{aligned} \quad (42)$$

With the above formulation, we then turn to describe various theoretical models for analyzing electromagnetic meson production reactions.

4. Theoretical Models

The development of theoretical models for investigating electromagnetic pion production reactions began in 1950's with the pioneering work by Chew, Goldberger, Low and Nambu (CGLN).⁴⁷ In the subsequent years, their dispersion-relation approach was the basis of many analyses⁴⁹ of pion production data in the Δ excitation region. This approach has been revived^{50,51} recently and extended^{52,53} to also analyze η production. For investigating the data at higher energies where the production of two pions and other mesons (η and K , ω , and ϕ) could arise, the isobar models⁴⁸ were developed to extract the parameters of higher mass nucleon resonances. During the years around 1980, the K-matrix effective Lagrangian models^{54,55} were developed to study the Δ excitation. The K-matrix method and isobar parameterization have been used subsequently to develop tools for performing amplitude analyses of the data and determining the resonance parameters. Examples are the very useful dial-in codes SAID⁵⁶ and MAID.⁵⁷ Progress has also been made in extracting resonance parameters using the multi-channel K-matrix method⁵⁸⁻⁶⁰ and the unitary coupled-channel isobar model.⁶¹⁻⁶³

In recent years, a rather different theoretical point of view has been taken to develop dynamical models⁶⁴⁻⁷⁸ of meson production reactions. These models account for the off-shell scattering effects and can therefore provide a much more direct way to interpret the resonance parameters in terms of the existing hadron structure models. So far, the dynamical reaction model has been able to interpret the resonance parameters, in particular the Δ resonance, in terms of constituent quark models. Its connection with the results from quenched and unquenched Lattice QCD calculations remains to be established.

In the first part of this section, we will give a general derivation of most of the existing models in order to clarify their differences. We then give some detailed formula for the dynamical model which are needed for discussing the results in Sec. 5. The analyses based on the dispersion relation approach will be described at the end of this section.

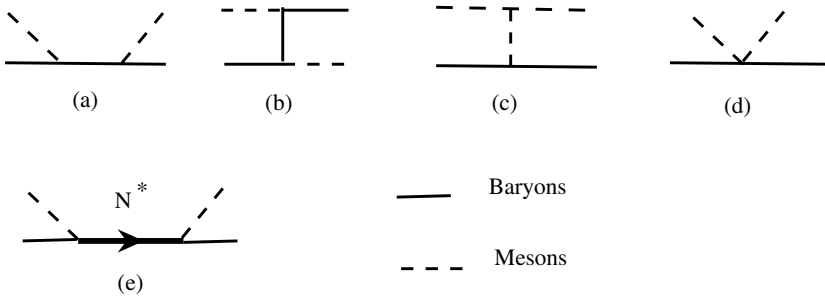


Fig. 6. Tree diagrams for meson–baryon interactions. N^* is a nucleon resonance.

4.1. Hamiltonian formulation

Most of the existing models for analyzing the data of electromagnetic meson production reactions can be schematically derived from a Hamiltonian formulation of the problem. The starting point of our derivation is to assume that the meson–baryon (MB) reactions can be described by a Hamiltonian of the following form

$$H = H_0 + V, \tag{43}$$

where H_0 is the free Hamiltonian and

$$V = v^{\text{bg}} + v^R. \tag{44}$$

Here v^{bg} is the non-resonant (background) term due to the mechanisms such as the tree-diagram mechanisms illustrated in Fig. 6(a)–(d), and v^R describes the N^* excitation in Fig. 6(e). Schematically, the resonant term can be written as

$$v^R(E) = \sum_{N_i^*} \frac{\Gamma_i^\dagger \Gamma_i}{E - M_i^0}, \tag{45}$$

where Γ_i defines the decay of the i th N^* state into meson–baryon states, and M_i^0 is a mass parameter related to the resonance position.

The next step is to define a channel space spanned by the considered meson–baryon (MB) channels: γN , πN , ηN , $\pi \Delta$, ρN , σN , \dots . The S-matrix of the meson–baryon reaction is defined by

$$S(E)_{a,b} = \delta_{a,b} - 2\pi i \delta(E - H_0) T_{a,b}(E), \tag{46}$$

where (a, b) denote MB channels, and the scattering T-matrix is defined by the following coupled-channel equation:

$$T_{a,b}(E) = V_{a,b} + \sum_c V_{a,c} g_c(E) T_{c,b}(E). \tag{47}$$

Here the meson–baryon propagator of channel c is

$$g_c(E) = \langle c | g(E) | c \rangle$$

with

$$\begin{aligned}
 g(E) &= \frac{1}{E - H_0 + i\epsilon} \\
 &= g^P(E) - i\pi\delta(E - H_0),
 \end{aligned}
 \tag{48}$$

where

$$g^P(E) = \frac{P}{E - H_0}.
 \tag{49}$$

Here P denotes taking the principal-value part of any integration over the propagator. We can also define K-matrix as

$$K_{a,b}(E) = V_{a,b} + \sum_c V_{a,c}g_c^P(E)K_{c,b}(E).
 \tag{50}$$

Equations (47)–(50) then define the following relation between the K-matrix and T-matrix:

$$T_{a,b}(E) = K_{a,b}(E) - \sum_c T_{a,c}(E)[i\pi\delta(E - H_0)]_cK_{c,b}(E).
 \tag{51}$$

By using the two potential formulation,⁹⁴ one can cast Eq. (47) into the following form

$$T_{a,b}(E) = t_{a,b}^{\text{bg}}(E) + t_{a,b}^R(E)
 \tag{52}$$

with

$$t_{a,b}^R(E) = \sum_{N_i^*, N_j^*} \bar{\Gamma}_{N_i^*, a}^\dagger(E)[G(E)]_{i,j}\bar{\Gamma}_{N_j^*, b}(E).
 \tag{53}$$

The first term of Eq. (52) is determined only by the non-resonant interaction,

$$t_{a,b}^{\text{bg}}(E) = v_{a,b}^{\text{bg}} + \sum_c v_{a,c}^{\text{bg}}g_c(E)t_{c,b}^{\text{bg}}(E).
 \tag{54}$$

The resonant amplitude Eq. (53) is determined by the dressed vertex,

$$\bar{\Gamma}_{N^*, a}(E) = \Gamma_{N^*, a} + \sum_b \Gamma_{N^*, b}g_b(E)t_{b,a}^{\text{bg}}(E),
 \tag{55}$$

and the dressed propagator,

$$[G(E)^{-1}]_{i,j}(E) = (E - M_{N_i^*}^0)\delta_{i,j} - \Sigma_{i,j}(E).
 \tag{56}$$

Here $M_{N^*}^0$ is the bare mass of the resonance state N^* , and the self-energy is

$$\Sigma_{i,j}(E) = \sum_a \Gamma_{N^*, a}^\dagger g_a(E)\bar{\Gamma}_{N_j^*, a}(E).
 \tag{57}$$

Note that the meson–baryon propagator $g_a(E)$ for channels including an unstable particle, such as $\pi\Delta$, ρN and σN , must be modified to include a width due to their decay into $\pi\pi N$ channel. In the Hamiltonian formulation, this amounts to the following replacement

$$g_a(E) \rightarrow \left\langle a \left| \frac{1}{E - H_0 - \Sigma_V(E)} \right| a \right\rangle, \quad (58)$$

where the energy shift is

$$\Sigma_V(E) = \sum_i \Gamma_V^+(i) \frac{P_{\pi\pi N}}{E - H_0 + i\epsilon} \Gamma_V(i). \quad (59)$$

Here Γ_V describes the decay of ρ , σ or Δ in the quasi-particle channels.

Equations (47), (52)–(59) and (51) are the starting points of our derivations. From now on, we consider the formulation in the partial-wave representation. The channel labels (a, b, c) will also include the usual angular momentum and isospin quantum numbers.

4.2. Tree-diagram models

The tree-diagram models are based on the simplification that $T \sim V = v^{\text{bg}} + v^R$. The resonant effect is included by modifying the mass parameter of v^R , defined in Eq. (45), to include a width, such as $M_i^0 = M_i - \frac{i}{2}\Gamma_i^{\text{tot}}(E)$. Equation (47) is then simplified into

$$T_{a,b}(\text{tree}) = v_{a,b}^{\text{bg}} + \sum_{N_i^*} \frac{\Gamma_{i,a}^{\dagger} \Gamma_{i,b}}{E - M_i^0 + \frac{i}{2}\Gamma_i^{\text{tot}}(E)}, \quad (60)$$

where v^{bg} is calculated from the tree-diagrams (Fig. 6(a)–(d)) of a chosen Lagrangian, and Γ_i^{tot} is the total decay width of the i th N^* .

In recent years, the tree-diagram models have been applied mainly to investigate the photoproduction and electroproduction of K mesons,^{79–84} vector mesons^{85–87} (ω , ϕ) and two pions.⁹⁰ At high energies, the t-channel amplitudes (Fig. 6(b)–(c)) are replaced by the Regge parameterization in some tree-diagram models.^{88,89} The validity of using the tree-diagram models to investigate nucleon resonances is obviously very questionable, as discussed in a study of ω photoproduction⁸⁷ and kaon photoproduction.⁷⁴

4.3. Unitary Isobar Models (UIM)

4.3.1. MAID

The Unitary Isobar Model developed⁵⁷ by the Mainz group is based on the on-shell relation Eq. (51). By including only one hadron channel, πN (or ηN), Eq. (51)

leads to

$$\begin{aligned} T_{\pi N, \gamma N} &= \frac{1}{1 + iK_{\pi N, \pi N}} K_{\pi N, \gamma N} \\ &= e^{i\delta_{\pi N}} \cos \delta_{\pi N} K_{\pi N, \gamma N}. \end{aligned} \quad (61)$$

Here we have used the relation $K_{\pi N, \pi N} = -\tan \delta_{\pi N}$ with $\delta_{\pi N}$ being the pion-nucleon scattering phase shift. By further assuming that $K = V = v^{\text{bg}} + v^R$, one can cast the above equation into the following form

$$T_{\pi N, \gamma N}(\text{UIM}) = e^{\delta_{\pi N}} \cos \delta_{\pi N} [v_{\pi N, \gamma N}^{\text{bg}}] + \sum_{N_i^*} T_{\pi N, \gamma N}^{N_i^*}(E). \quad (62)$$

Clearly, the non-resonant multi-channel effects, such as $\gamma N \rightarrow (\rho N, \pi \Delta) \rightarrow \pi N$, which could be important in the second and third resonance regions are neglected in MAID. In addition, they calculate the non-resonant amplitude $v_{\pi N, \gamma N}^{\text{bg}}$ using an energy-dependent mixture of PV and PS (pseudo-scalar) πNN coupling:

$$L_{\pi NN} = \frac{\Lambda_m^2}{\Lambda_m^2 + q_0^2} L_{\pi NN}^{\text{PV}} + \frac{q_0^2}{\Lambda_m^2 + q_0^2} L_{\pi NN}^{\text{PS}}, \quad (63)$$

where q_0 is the on-shell photon momentum. With cutoff $\Lambda_m = 450$ MeV, one then gets PV coupling at low energies and PS coupling at high energies.

For resonant terms in Eq. (62), MAID uses the following Walker's parameterization⁴⁸

$$T_{\pi N, \gamma N}^{N_i^*}(E) = f_{\pi N}^i(E) \frac{\Gamma_{\text{tot}} M_i e^{i\Phi}}{M_i^2 - E^2 - iM_i \Gamma_{\text{tot}}} f_{\gamma N}^i(E) \bar{A}^i, \quad (64)$$

where $f_{\pi N}^i(E)$ and $f_{\gamma N}^i(E)$ are the form factors describing the decays of N^* , Γ_{tot} is the total decay width, \bar{A}^i is the $\gamma N \rightarrow N^*$ excitation strength. The phase Φ is determined by the unitary condition and the assumption that the phase ψ of the total amplitude is related to πN phase shift $\delta_{\pi N}$ and inelasticity $\eta_{\pi N}$ by

$$\psi(E) = \tan^{-1} \left[\frac{1 - \eta_{\pi N}(E) \cos 2\delta_{\pi N}(E)}{\eta_{\pi N}(E) \sin 2\delta_{\pi N}(E)} \right]. \quad (65)$$

4.3.2. JLab/Yerevan UIM

The Jlab/Yerevan UIM⁵³ is similar to MAID. But it implements the Regge parameterization in calculating the amplitudes at high energies. It also uses a different procedure to unitarize the amplitudes.

Both MAID and JLab/Yerevan UIM have been applied extensively to analyze the data of π and η production reactions, as will be discussed in Sec. 5. Very useful new information on N^* have been extracted.

4.4. Multi-channel *K*-matrix models

4.4.1. SAID

The model employed in SAID⁵⁶ is based on the on-shell relation Eq. (51) with three channels: γN , πN , and $\pi\Delta$, which represents all other open channels. The solution of the resulting 3×3 matrix equation can be written as

$$T_{\gamma N, \pi N}(\text{SAID}) = A_I(1 + iT_{\pi N, \pi N}) + A_R T_{\pi N, \pi N}, \quad (66)$$

where

$$A_I = K_{\gamma N, \pi N} - \frac{K_{\gamma N, \pi\Delta} K_{\pi N, \pi N}}{K_{\pi N, \pi\Delta}}, \quad (67)$$

$$A_R = \frac{K_{\gamma N, \pi\Delta}}{K_{\pi N, \pi\Delta}}. \quad (68)$$

In actual analyses, they simply parameterize A_I and A_R as

$$A_I = [v_{\gamma N, \pi N}^{\text{bg}}] + \sum_{n=0}^M \bar{p}_n z Q_{l_\alpha+n}(z), \quad (69)$$

$$A_R = \frac{m_\pi}{k_0} \left(\frac{q_0}{k_0}\right)^{l_\alpha} \sum_{n=0}^N p_n \left(\frac{E_\pi}{m_\pi}\right)^n, \quad (70)$$

where k_0 and q_0 are the on-shell momenta for pion and photon respectively, $z = \sqrt{k_0^2 + 4m_\pi^2}/k_0$, $Q_L(z)$ is the legendre polynomial of second kind, $E_\pi = E_\gamma - m_\pi(1 + m_\pi/(2m_N))$, and p_n and \bar{p}_n are free parameters. SAID calculates $v_{\gamma N, \pi N}^{\text{bg}}$ of Eq. (69) from the standard PS Born term and ρ and ω exchanges. The empirical πN amplitude $T_{\pi N, \pi N}$ needed to evaluate Eq. (66) is also available in SAID.

Once the parameters \bar{p}_n and p_n in Eqs. (69) and (70) are determined, the N^* parameters are then extracted by fitting the resulting amplitude $T_{\gamma N, \pi N}$ at energies near the resonance position to a Breit–Wigner parameterization (similar to Eq. (64)). Very extensive data of pion photoproduction have been analyzed by SAID. The extension of SAID to also analyze pion electroproduction data is being pursued.

4.4.2. Giessen model

The coupled-channel model developed by the Giessen group⁶⁰ can be obtained from Eq. (51) by taking the approximation $K = V$; namely, neglecting all multiple-scattering effects included in Eq. (50) for *K*-matrix. This leads to a matrix equation involving only the on-shell matrix elements of V :

$$T_{a,b}(\text{Giessen}) = \sum_c [(1 + iV(E))^{-1}]_{a,c} V_{c,b}(E). \quad (71)$$

The interaction $V = v^{\text{bg}} + v^R$ is evaluated from tree-diagrams of various effective Lagrangians. The form factors, coupling constants, and resonance parameters are

adjusted to fit both the πN and γN reaction data. They include up to five channels in some fits, and have identified several new N^* states. But further confirmations are needed to establish their findings conclusively, as will be discussed later in Sec. 5.6.

4.4.3. KSU model

The Kent State University (KSU) model⁵⁸ can be derived by noting that the non-resonant amplitude t^{bg} , defined by a *hermitian* v^{bg} in Eq. (54), define a S-matrix with the following properties:

$$S_{a,b}^{\text{bg}}(E) = \delta_{a,b} - 2\pi i \delta(E - H_0) t_{a,b}^{\text{bg}}(E) \quad (72)$$

$$= \sum_c \omega_{a,c}^{(+T)}(E) \omega_{c,b}^{(+)}(E), \quad (73)$$

where the non-resonant scattering operator is

$$\omega_{a,c}^{(+)}(E) = \delta_{a,c} + g_a(E) t_{a,c}^{\text{bg}}(E). \quad (74)$$

With some derivations, the S-matrix Eq. (46) and the scattering T-matrix defined by Eqs. (52)–(57) can then be cast into following form:

$$S_{a,b}(E) = \sum_{c,d} \omega_{a,c}^{(+T)}(E) R_{c,d}(E) \omega_{c,b}^{(+)}(E) \quad (75)$$

with

$$R_{c,d}(E) = \delta_{c,d} + 2iT_{c,d}^R(E). \quad (76)$$

$$(77)$$

Here, we have defined

$$T_{c,d}^R(E) = \sum_{i,j} \Gamma_{N_i^*,c}^\dagger(E) [G(E)]_{i,j} \Gamma_{N_j^*,d}(E). \quad (78)$$

The above set of equations is identical to that used in the KSU model of Ref. 58. In practice, the KSU model fits the data by parameterizing T^R as a Breit–Wigner resonant form $T^R \sim x\Gamma/2/(E - M - i\Gamma/2)$ and setting $\omega^{(+)} = B = B_1 B_2 \cdots B_n$, where $B_i = \exp(iX\Delta_i)$ is a unitary matrix.

The KSU model has been applied to πN reactions, including pion photoproduction. It is now being extended to investigate $\bar{K}N$ reactions.

4.5. The CMB model

A unitary multi-channel isobar model with analyticity was developed⁶¹ in 1970's by the Carnegie-Mellon Berkeley (CMB) collaboration to analyze the πN data. The CMB model can be derived by assuming that the non-resonant potential v^{bg} is also of the separable form of v^R of Eq. (45):

$$v_{a,b}^{\text{bg}} = \frac{\Gamma_{L,a}^\dagger \Gamma_{L,b}}{E - M_L} + \frac{\Gamma_{H,a}^\dagger \Gamma_{H,b}}{E - M_H}. \quad (79)$$

The resulting coupled-channel equations are identical to Eqs. (52)–(59), except that $t_{a,b}^{\text{bg}} = 0$ and the sum over N_i^* is now extended to include these two distance poles L and H .

By changing the integration variables and adding a subtraction term, Eq. (57) for the self-energy can lead to CMB’s dispersion relations:

$$\Sigma_{i,j}(s) = \sum_c \gamma_{i,c} \Phi_c(s) \gamma_{j,c}, \quad (80)$$

$$\text{Re}[\Phi_c(s)] = \text{Re}[\Phi_c(s_0)] + \frac{s - s_0}{\pi} \int_{s_{\text{th}}}^\infty \frac{\text{Im}[\Phi_c(s')]}{(s' - s)(s' - s_0)} ds', \quad (81)$$

where $\gamma_{i,c}$ is a coupling constant defining the decay of N_i^* into channel c . Thus the CMB model is analytic in structure, which marks its difference with all K-matrix models described above.

The CMB model has been revived in recent years by the Zagreb group⁶² and a Pittsburgh-ANL collaboration⁶³ to extract the N^* parameters from fitting the recent empirical πN and γN reaction amplitudes. The resulting N^* parameters have very significant differences with what are listed by PDG in some partial waves. In particular, several important issues concerning the extraction of the N^* parameters in S_{11} channel have been analyzed in detail.

4.6. Dynamical models

4.6.1. In the Δ region

Keeping only one resonance $N^* = \Delta$ and two channels $a, b = \pi N, \gamma N$, Eqs. (52)–(57) are reduced to what were developed in the Sato–Lee (SL) model.^{68,70}

Explicitly, we have

$$T_{\pi N, \pi N}(E) = t_{\pi N, \pi N}^{\text{bg}}(E) + \frac{\bar{\Gamma}_{\Delta, \pi N}^\dagger(E) \bar{\Gamma}_{\Delta, \pi N}(E)}{E - M_\Delta^0 - \Sigma_\Delta(E)}, \quad (82)$$

$$T_{\gamma N, \pi N}(E) = t_{\gamma N, \pi N}^{\text{bg}}(E) + \frac{\bar{\Gamma}_{\Delta, \gamma N}^\dagger(E) \bar{\Gamma}_{\Delta, \pi N}(E)}{E - M_\Delta^0 - \Sigma_\Delta(E)}, \quad (83)$$

with

$$\bar{\Gamma}_{\Delta, \gamma N}(E) = \Gamma_{\Delta, \gamma N} + \Gamma_{\Delta, \pi N} G_{\pi N}(E) t_{\pi N, \gamma N}^{\text{bg}}(E), \quad (84)$$

$$\bar{\Gamma}_{\Delta, \pi N}(E) = \Gamma_{\Delta, \pi N} + \Gamma_{\Delta, \pi N} G_{\pi N}(E) t_{\pi N, \pi N}^{\text{bg}}(E), \quad (85)$$

$$t_{\pi N, \gamma N}^{\text{bg}}(E) = v_{\pi N, \gamma N}^{\text{bg}} + t_{\pi N, \pi N}^{\text{bg}}(E) G_{\pi N}(E) v_{\pi N, \gamma N}^{\text{bg}}, \quad (86)$$

$$t_{\pi N, \pi N}^{\text{bg}}(E) = v_{\pi N, \pi N}^{\text{bg}} + v_{\pi N, \pi N}^{\text{bg}} G_{\pi N}(E) t_{\pi N, \pi N}^{\text{bg}}(E), \quad (87)$$

and

$$\Sigma_{\Delta}(E) = \Gamma_{\Delta, \pi N}^{\dagger}(E) G_{\pi N}(E) \bar{\Gamma}_{\Delta, \pi N}(E). \quad (88)$$

The above equations clearly indicate how the non-resonant interaction modify the resonant amplitude. Specifically, Eq. (84) for the dressed $\Delta \rightarrow \gamma N$ within the SL model is illustrated in Fig. 7.

Alternatively, we can also cast Eq. (47) in the Δ region as

$$T_{\gamma N, \pi N}(E) = t_{\gamma N, \pi N}^B(E) + t_{\gamma N, \pi N}^R(E) \quad (89)$$

with

$$t_{\gamma N, \pi N}^B(E) = v_{\gamma N, \pi N}^{bg} + v_{\gamma N, \pi N}^{bg} G_{\pi N}(E) T_{\pi N, \pi N}(E), \quad (90)$$

$$t_{\gamma N, \pi N}^R(E) = v_{\gamma N, \pi N}^R + v_{\gamma N, \pi N}^R G_{\pi N}(E) T_{\pi N, \pi N}(E). \quad (91)$$

The above equations are used by the Dubna–Mainz–Taipei (DMT) model^{71,73} except that they depart from a consistent Hamiltonian formulation and replace the term $t_{\gamma N, \pi N}^R$ by the Walker’s parameterization⁴⁸:

$$t_{\gamma N, \pi N}^R(E) = f_{\pi N}(E) \frac{\Gamma_{\text{tot}} M_{\Delta} e^{i\Phi}}{M_{\Delta}^2 - E^2 - i M_{\Delta} \Gamma_{\text{tot}}} f_{\gamma N}(E) \bar{A}_{\gamma N}. \quad (92)$$

Other differences between the SL Model and the DMT model are in the employed πN potential and how the non-resonant $\gamma N \rightarrow \pi N$ amplitudes are regularized. In the DMT model, the non-resonant $\gamma N \rightarrow \pi N$ amplitudes are calculated by using MAID’s mixture Eq. (63) of PS and PV couplings, while their πN potential is from a model⁹⁵ using PV coupling. In the SL model, the standard PV coupling is used in a consistent derivation of both the πN potential and $\gamma N \rightarrow \pi N$ transition interaction using a unitary transformation method.

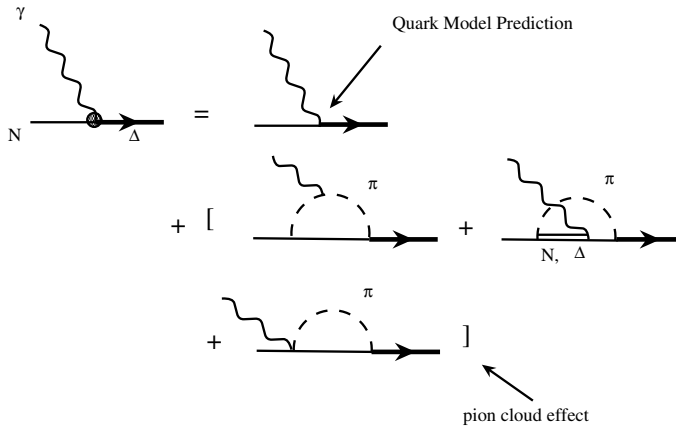


Fig. 7. Graphic representation of the dressed $\gamma N \rightarrow \Delta$ vertex.

We now turn to giving relevant formula which are needed for our discussions in Sec. 5.1 on the Δ resonance. The Δ excitation is parameterized in terms of Rarita-Schwinger field. In the Δ rest frame where $m_\Delta = q_0 + E_N(\vec{q})$, the resulting $\gamma N \rightarrow \Delta$ vertex function can be written in the following more transparent form:

$$\begin{aligned} \langle \Delta | \Gamma_{\gamma N \rightarrow \Delta} | q \rangle = & -\frac{e}{(2\pi)^{3/2}} \sqrt{\frac{E_N(\vec{q}) + m_N}{2E_N(\vec{q})}} \frac{1}{\sqrt{2\omega}} \frac{3(m_\Delta + m_N)}{4m_N(E_N(\vec{q}) + m_N)} T_3 \\ & \times \left[iG_M(q^2) \vec{S} \times \vec{q} \cdot \vec{\epsilon} + G_E(q^2) (\vec{S} \cdot \vec{\epsilon} \vec{\sigma} \cdot \vec{q} + \vec{S} \cdot \vec{q} \vec{\sigma} \cdot \vec{\epsilon}) \right. \\ & \left. + \frac{G_C(q^2)}{m_\Delta} \vec{S} \cdot \vec{q} \vec{\sigma} \cdot \vec{q} \epsilon_0 \right], \end{aligned} \tag{93}$$

where $e = \sqrt{4\pi/137}$, $q = (\omega, \vec{q})$ is the photon four-momentum, and $\epsilon = (\epsilon_0, \vec{\epsilon})$ is the photon polarization vector. The transition operators \vec{S} and \vec{T} are defined by the reduced matrix element $\langle \Delta || \vec{S} || N \rangle = \langle \Delta || \vec{T} || N \rangle = 2$ in Edmonds' convention.^a By using Eq. (93) and the standard definitions^{96,97} of the multipole amplitudes, it is straightforward to evaluate the magnetic M1, electric E2 and Coulomb C2 amplitudes of the $\gamma N \rightarrow \Delta$ transition. We find⁷⁰ that

$$G_M(q^2) = \frac{1}{N} [\Gamma_{\gamma N \rightarrow \Delta}]_{M1}, \tag{94}$$

$$G_E(q^2) = \frac{-1}{N} [\Gamma_{\gamma N \rightarrow \Delta}]_{E2}, \tag{95}$$

$$G_C(q^2) = \frac{2m_\Delta}{|\vec{q}|N} [\Gamma_{\gamma N \rightarrow \Delta}]_{C2}, \tag{96}$$

with

$$N = \frac{e}{2m_N} \sqrt{\frac{m_\Delta |\vec{q}|}{m_N}} \frac{1}{[1 - q^2/(m_N + m_\Delta)^2]^{1/2}}.$$

At $q^2 = 0$, the above relations agree with that given in Appendix A of Ref. 66. Equations (93)–(96) can also be used to relate the dressed vertex $\bar{\Gamma}_{\gamma N \rightarrow \Delta}$, defined by Eq. (84), to the corresponding dressed form factors:

$$G_M^*(q^2) = \frac{1}{N} [\bar{\Gamma}_{\gamma N \rightarrow \Delta}]_{M1},$$

$$G_E^*(q^2) = \frac{-1}{N} [\bar{\Gamma}_{\gamma N \rightarrow \Delta}]_{E2},$$

$$G_C^*(q^2) = \frac{2m_\Delta}{|\vec{q}|N} [\bar{\Gamma}_{\gamma N \rightarrow \Delta}]_{C2}.$$

^aWe use Edmond's convention $\langle J' M' | T_{kq} | J M \rangle = (-1)^{2k} \langle J' M' | J k M q \rangle / \sqrt{2J' + 1} \langle J' | T | J \rangle$.

At the $q^2 = 0$ photon point, we will also compare our results with the helicity amplitudes defined by PDG.²⁴ They are related to the multipole amplitudes defined above by

$$A_{3/2} = \frac{\sqrt{3}}{2} [[\bar{\Gamma}_{\gamma N \rightarrow \Delta}]_{E2} - [\bar{\Gamma}_{\gamma N \rightarrow \Delta}]_{M1}], \quad (97)$$

$$A_{1/2} = -\frac{1}{2} [3[\bar{\Gamma}_{\gamma N \rightarrow \Delta}]_{E2} + [\bar{\Gamma}_{\gamma N \rightarrow \Delta}]_{M1}]. \quad (98)$$

At the Δ resonance position $E = M_R = 1236$ MeV, the πN phase shift in the P_{33} channel goes through 90 degrees. This leads to a relation, as derived in detail in Ref. 68, that the multipole components of the dressed vertex $\bar{\Gamma}_{\gamma N \rightarrow \Delta}$ are related to the imaginary (Im) parts of the $\gamma N \rightarrow \pi N$ multipole amplitudes in the $\pi N P_{33}$ channel

$$G_M^*(q^2) = \frac{1}{N} [\bar{\Gamma}_{\gamma N \rightarrow \Delta}^K]_{M1} = \frac{1}{N} \sqrt{\frac{8\pi m_\Delta k \Gamma_\Delta}{3m_N q}} \times \text{Im}(M_{1+}^{3/2}), \quad (99)$$

$$G_E^*(q^2) = \frac{1}{N} [\bar{\Gamma}_{\gamma N \rightarrow \Delta}^K]_{E2} = -\frac{1}{N} \sqrt{\frac{8\pi m_\Delta k \Gamma_\Delta}{3m_N q}} \times \text{Im}(E_{1+}^{3/2}), \quad (100)$$

$$\frac{|\vec{q}|}{2m_\Delta} G_C^*(q^2) = \frac{1}{N} [\bar{\Gamma}_{\gamma N \rightarrow \Delta}^K]_{C2} = \frac{1}{N} \sqrt{\frac{8\pi m_\Delta k \Gamma_\Delta}{3m_N q}} \times \text{Im}(S_{1+}^{3/2}), \quad (101)$$

where Γ_Δ is the Δ width, k and q are respectively the momenta of the pion and photon in the rest frame of the Δ . Note that the upper index K in $\Gamma_{\Delta, \gamma N}^K$ in Eqs. (99)–(101) means taking only the principal-value integration in evaluating the second term of Eq. (84). Details are discussed in Ref. 68.

From the above relations, we obtain a very useful relation that the E2/M1 ratio R_{EM} and C2/M1 ratio R_{SM} of the dressed $\gamma N \rightarrow \Delta$ transition at $W = 1232$ MeV can be evaluated directly by using the $\gamma N \rightarrow \pi N$ multipole amplitudes:

$$R_{EM} = \frac{[\bar{\Gamma}_{\gamma N \rightarrow \Delta}^K]_{E2}}{[\bar{\Gamma}_{\gamma N \rightarrow \Delta}^K]_{M1}} = \frac{\text{Im}(E_{1+}^{3/2})}{\text{Im}(M_{1+}^{3/2})}, \quad (102)$$

$$R_{SM} = \frac{[\bar{\Gamma}_{\gamma N \rightarrow \Delta}^K]_{C2}}{[\bar{\Gamma}_{\gamma N \rightarrow \Delta}^K]_{M1}} = \frac{\text{Im}(S_{1+}^{3/2})}{\text{Im}(M_{1+}^{3/2})}. \quad (103)$$

Eqs. (99)–(103) can be used in the empirical amplitude analyses to extract the form factors and the E2/M1 and C2/M1 ratios of the $\gamma N \rightarrow \Delta$ transition. The extractions of the bare vertices, which can be compared with the predictions from most of the constituent quark model calculations, can only be achieved by using the dynamical model through Eq. (84). This indicates why an appropriate reaction theory is needed in the N^* study, as illustrated in Fig. 1.

4.6.2. *In the second and third resonance regions*

In these regions, we need to include more than the πN channel to solve Eq. (47) or Eqs. (52)–(59). In addition, these formulae must be extended to include explicitly the $\pi\pi N$ channel, instead of using the quasi two-particle channels $\pi\Delta$, ρN , and σN to simulate the $\pi\pi N$ continuum. This, however, is still being developed.⁷⁶ Here we continue to explain the current investigations in the second and third resonance regions within the formulation defined by Eqs. (52)–(59).

Equations (52)–(59) are used in a 2- N^* and 3-channel (πN , ηN , and $\pi\Delta$) study⁶⁹ of πN scattering in S_{11} partial wave, aiming at investigating how the quark–quark interaction in the constituent quark model can be determined directly by using the reaction data. Eqs. (52)–(59) are also the basis of examining the N^* effects⁸⁶ and one-loop coupled-channel effects⁸⁷ on ω meson photoproduction and the coupled-channel effects on K photoproduction.⁷⁴

The coupled-channel study of both πN scattering and $\gamma N \rightarrow \pi N$ in the S_{11} channel by Chen *et al.*⁷² includes πN , ηN , and γN channels. Their πN scattering calculation is performed by using Eq. (47), which is of course equivalent to Eqs. (52)–(59). In their $\gamma N \rightarrow \pi N$ calculation, they neglect the $\gamma N \rightarrow \eta N \rightarrow \pi N$ coupled-channel effect, and follow the procedure of the DMT model to evaluate the resonant term in terms of the Walker’s parameterization (Eq. (64)). They find that four N^* are needed to fit the empirical amplitudes in the S_{11} channel up to $W = 2$ GeV.

A coupled-channel calculation based on Eq. (47) has been carried out by Jülich group¹⁰³ for πN scattering. They are able to describe the πN phase shifts up to $W = 1.9$ GeV by including πN , ηN , $\pi\Delta$, ρN and σN channels and 5 N^* resonances: $P_{33}(1232)$, $S_{11}(1535)$, $S_{11}(1530)$, $S_{11}(1650)$ and $D_{13}(1520)$. They find that the Roper resonance $P_{11}(1440)$ is completely due to the meson-exchange coupled-channel effects.

A coupled channel calculation based on Eq. (47) for both πN scattering and $\gamma N \rightarrow \pi N$ up to $W = 1.5$ GeV has been reported by Fuda and Alharbi.⁷⁵ They include πN , γN , ηN , and $\pi\Delta$ channels and 4 N^* resonances: $P_{33}(1232)$, $P_{11}(1440)$, $S_{11}(1535)$, and $D_{13}(1520)$. The parameters are adjusted to fit the empirical multipole amplitudes in a few low partial waves.

Much simpler coupled-channel calculations have been performed by using separable interactions. In the model of Gross and Surya,⁶⁷ such separable interactions are from simplifying the meson-exchange mechanisms in Figs. 6(a)–(c) as a contact term like Fig. 6(d). They include only πN and γN channels and 3 resonances: $P_{33}(1232)$, $P_{11}(1440)$ and $D_{13}(1520)$, and restrict their investigation up to $W < 1.5$ GeV. To account for the inelasticities in P_{11} and D_{13} , the $N^* \rightarrow \pi\Delta$ coupling is introduced in these two partial waves. The inelasticities in other partial waves are neglected.

A similar separable simplification is also used in the chiral coupled-channel models^{77,78} for strange particle production. There the separable interactions are

directly determined from the leading contact terms of SU(3) effective chiral Lagrangian and hence only act on s-wave partial waves. They are able to fit the total cross-section data for various strange particle production reaction channels without introducing resonance states. It remains to be seen whether these models can be further improved to account for higher partial waves, which are definitely needed to give an accurate description of the data even at energies near production threshold. Some progress in this direction has been made recently.²⁰⁷

4.7. Dispersion-relation approaches

Historically, the approach based on dispersion relations is defined within the S-matrix theory which was introduced as an alternative to the relativistic quantum field theory in investigating non-perturbative hadron interactions. This approach was first applied to investigate pion photoproduction by Chew, Goldberger, Low and Nambu⁴⁷ (CGLN) and electroproduction by Amaldi, Fubini and Furlan.⁹⁷ It was fully developed^{49,104} in the years around 1970 to analyze the data at energies near the Δ resonance. In recent years, it has been revived by Aznauryan,^{51,52} and by Hanstein, Drechsel, and Tiator⁵⁰ for investigating pion photoproduction and η photoproduction.⁵³

The dispersion relation approach assumes that the scattering amplitude is unitary and possesses various established symmetry properties such as Lorentz invariance and gauge invariance. The dynamics is defined by the assumed analytical property and crossing symmetry. For π and η production, the starting point is the fixed- t dispersion relation¹⁰⁵ for the invariant amplitudes A_i defined in Eq. (24):

$$\text{Re}[A_k^I(s, t)] = A_k^{I,\text{pole}}(s, t) + \frac{1}{\pi} P \int_{s_{\text{thr}}}^{\infty} ds' \left[\frac{1}{s' - s} + \frac{\epsilon^I \xi_k}{s' - u} \right] \text{Im}[A_k^I(s', t)], \quad (104)$$

where $A_k^{I,\text{pole}}(s, t)$ is calculated from pseudo-scalar Born term, $I = 0, +, -$ denote the isospin component, and $\xi_1 = \xi_2 = -\xi_3 = -\xi_4 = 1$ and $\epsilon^+ = \epsilon^0 = -\epsilon^- = 1$ are defined such that the crossing symmetry relation $A_k^I(s, t, u) = \xi_k \epsilon^I A_k^I(u, t, s)$ is satisfied. With the definitions Eqs. (23) and (27) and the multipole expansion defined by Eqs. (35)–(40), the above fixed- t dispersion relation leads to the following set of coupled equations relating the real part and imaginary parts of multipole amplitudes:

$$\text{Re}[M_\ell^I(W)] = M_\ell^{I,\text{pole}}(W) + \frac{P}{\pi} \int_{W_{\text{thr}}}^{\infty} dW' \sum_{\ell'} K_{\ell\ell'}^I(W, W') \text{Im}[M_{\ell'}^I(W)], \quad (105)$$

where M_ℓ^I is the multipole amplitude, $M_\ell^{I,\text{pole}}(W)$ is calculated from pseudo-scalar Born term, and $K_{\ell\ell'}^I$ contains various kinematic factors. In the recent work of Ref. 50, the procedures of Ref. 104 are used to solve the above equations by using the method of Omnes.¹⁰⁶ It assumes that the multipole amplitude can be written as

$$M_\ell^I(W) = \exp^{i\phi_\ell(W)} \frac{1}{r_{\ell I}} M_\ell^I(W), \quad (106)$$

where M_ℓ^I is a real function and $r_{\ell I}$ is some kinematic factor, and hence

$$\text{Im}[M_\ell^I(W)] = h_\ell^{I*}(W)M_\ell^I(W), \quad (107)$$

with $h_\ell^I(w) = \sin(\phi_\ell^I) \exp^{i\phi_\ell^I(W)}$. The phase ϕ_ℓ^I is assumed to be

$$\phi_\ell^I(W) = \arctan\left(\frac{1 - \eta_\ell^I(W) \cos 2\delta_\ell^I(W)}{\eta_\ell^I(W) \sin 2\delta_\ell^I(W)}\right), \quad (108)$$

where δ_ℓ^I and η_ℓ^I are the phase and inelasticity of πN scattering in the partial-wave with quantum numbers (ℓ, I) .

The next approximation is to limit the sum over ℓ' in the right-hand side of Eq. (105) to a cutoff ℓ_{max} . For investigating production below $E_\gamma = 500$ MeV, $\ell_{\text{max}} = 1$ is taken. Another approximation is needed to handle the integration over W in Eq. (105). In Ref. 50, the integration is cutoff at $W = \Lambda = 2$ GeV such that all needed phase Φ_ℓ can be determined by the empirical πN phase shifts. The neglected contribution from $W > 2$ GeV is then accounted for by adding vector meson exchange terms. Equation (105) then becomes

$$M_\ell^I(W) = M_\ell^{I,\text{pole}}(W) + \frac{1}{\pi} \int_{W_{\text{thr}}}^\Lambda \frac{h_\ell^{I*}(W')M_\ell^I(W')dW'}{W' - W - i\epsilon} + \frac{1}{\pi} \sum_{\ell', I'} \int_{W_{\text{thr}}}^\Lambda dW' K_{\ell\ell'}^{I, I'}(WW')h_{\ell'}^{I'*}(W') + M_\ell^{I, V}(W). \quad (109)$$

The method for solving Eqs. (109) is given in Ref. 50. With the above procedures, the model contains ten adjustable parameters. An excellent fit to all $\gamma N \rightarrow \pi N$ data up to $E_\gamma = 500$ MeV has been obtained in Ref. 50.

The calculation in Ref. 51 follow the same approach with additional simplification that the coupling between different multipoles and the contribution from $W > \Lambda$ to the integration are neglected; setting $K_{\ell, \ell'}^{I, I'} = 0$ and $M_\ell^{I, V} = 0$ in solving Eq. (109). These simplifications are justified in calculating the dominant Δ excitation amplitude $M_{1+}^{(3/2)}$. But it is questionable if they can be applied for calculating weaker amplitudes. Thus no attempt was made in Refs. 51 and 52 to fit the data directly using dispersion relations. Rather, the emphasis was in the interpretation of the empirical amplitudes $M_{1+}^{(3/2)}$, $E_{1+}^{(3/2)}$ in terms of rescattering effects and constituent quark model prediction. By assuming the multipole expansion is also valid in electroproduction, the Q^2 -dependence of these Δ excitation amplitudes are then predicted. There are questions regarding the validity of multipole expansion at $E_\gamma > 500$ MeV and large Q^2 .¹⁰⁷

The dispersion relation approach is also used in Ref. 52 to analyze the pion photoproduction and electroproduction data in the second and third resonance region. It is assumed that the imaginary parts of the amplitudes in $M_N + m_\pi < W < 2$ GeV are from the resonant amplitudes parameterized as the Walker's Breit-Wigner form Eq. (64), and in $2.5 \text{ GeV} < \infty$ from Regge-pole model. The imaginary part of the amplitude in $2 \text{ GeV} < W < 2.5 \text{ GeV}$ is obtained by interpolation.

The real part of the amplitude is then calculated from the dispersion relation described above. The empirical amplitudes are then fitted by adjusting the resonant parameters. It turns out that the resulting parameters are close to what were determined in the single channel K-matrix model described in Sec. 4.3.2.

With appropriate modifications, the dispersion relation approach can be applied to investigate the production of other pseudo-scalar mesons. This has been achieved in Ref. 53 in analyzing the data of η production reactions.

5. Data and Results of Analyses

A large volume of data of electromagnetic meson production reactions is needed to extract the fundamental physics on resonance transition form factors or discover new baryon states. Efforts in this direction in the 1970s and 80s at various laboratories were hampered by the low duty cycle synchrotrons that were available for these studies, and by the use of magnetic spectrometers with relatively small acceptance. For a discussion on these results see the excellent review by F. Foster and G. Hughes.¹⁰⁸ The construction of CW electron accelerators and the advances in detector technologies have made it possible to use detector system with nearly 4π solid angle coverage, and the ability to operate at high luminosity. Moreover, the detection of multiple photons from π^0 or η decays with high resolution has become feasible with the development of high density crystals with sufficient light output, such as BGO, CsI, and PbF₂. These detectors have become powerful tools in the study of baryon spectroscopy and structure. In this section we will highlight the data and review the results from the analyses. We will only consider meson productions from nucleon targets. An extensive review of meson production from nuclei has been published recently.¹⁰⁹

5.1. Single pion production

Single pion photoproduction and electroproduction have been the main processes in the study of the electromagnetic transition amplitudes of the lower mass nucleon resonances such as $\Delta(1232)$, $P_{11}(1440)$, $D_{13}(1520)$, $S_{11}(1535)$, and $F_{15}(1680)$. Data on pion photoproduction now exist from LEGS¹¹⁰ and MAMI,¹¹¹ and from GRAAL,^{112,35} including results from measurements of polarized beam asymmetries and beam-target double polarization observables.^{113,114}

During the past few years high statistics data of pion electroproduction have been collected at JLab. The $ep \rightarrow ep\pi^0$ data cover a large range in invariant mass W from threshold to 2.5 GeV, a wide range in momentum-transfer $Q^2 = 0.1\text{--}6$ GeV², and the full range in azimuthal and polar angles in the $p\pi^0$ center-of-mass.

In the past there have been very limited data on $n\pi^+$, mostly at forward center of mass angles,^{119–121} some at backward angles.¹²² Even less data exist in π^- production from deuterium.¹²³ This has limited our ability to extract reliable resonance transition amplitudes in the high mass region where many isospin $\frac{1}{2}$ states exist, which couple more strongly to $n\pi^+$ than to $p\pi^0$. New $n\pi^+$ data from CLAS¹²⁴ have

Table 2. Summary of the single pion electroproduction data.

Reaction	Observable	W range (GeV)	Q^2 range (GeV ²)	Lab/experiment
$ep \rightarrow ep\pi^0$	$d\sigma/d\Omega$	< 1.8	0.4–1.8	JLab-CLAS ¹²⁵
	$d\sigma/d\Omega$	$\Delta(1232)$	0.1–0.9	ELSA-Elan ¹³⁰
	$d\sigma/d\Omega$	$\Delta(1232)$	2.8, 4.0	JLab-Hall C ¹¹⁶
	$d\sigma/d\Omega$	< 2.5 GeV	2–6	JLab-CLAS ¹³¹
	$d\sigma/d\Omega$	$\Delta(1232)$	7.5	JLab-CLAS ¹³²
	$d\sigma/d\Omega$	< 2.0	1.0	JLab-Hall A ¹¹⁷
$ep \rightarrow en\pi^+$	$d\sigma/d\Omega$	< 1.6	0.3–0.65	JLab-CLAS ¹²⁴
	$d\sigma/d\Omega$	$\Delta(1232)$	0.1–0.9	ELSA-Elan ¹³⁰
	$d\sigma/d\Omega$	< 2.5 GeV	2–6	JLab-CLAS ¹³¹
$\bar{e}p \rightarrow ep\pi^0$	A_e, A_{TT}, A_{TL}	$\Delta(1232)$	0.2	MAMI-A1 ¹²⁷
	$\sigma_{LT'}$	$\Delta(1232)$	0.3–0.65	JLab-CLAS ¹²⁶
	A_e	$\Delta(1232)$	0.126	Bates-OOPS ¹²⁸
$\bar{e}p \rightarrow en\pi^+$	$\sigma_{LT'}$	< 1.6	0.3–0.65	JLab-CLAS ¹²⁹
$\bar{e}p \rightarrow e\bar{p}\pi^0$	pol. resp. fct.	$\Delta(1232)$	1.0	JLab-Hall A ¹³³
$\bar{e}\bar{p} \rightarrow ep\pi^0$	A_p, A_{ep}	$\Delta(1232)$	0.5–1.5	JLab-CLAS ¹³⁵
$\bar{e}\bar{p} \rightarrow en\pi^+$	A_{ep}	< 1.85	0.4, 0.65, 1.1	JLab-CLAS ¹³⁴

nearly full angular coverage and span the range $W = 1.1$ – 1.6 GeV and $Q^2 = 0.3$ – 0.6 GeV². They vastly increased the covered kinematics with high statistics, and will be extended to $W \leq 2.5$ GeV² and $Q^2 = 0.1$ – 6 GeV².

For the first time there are also significant amounts of polarized beam asymmetries data and data on the beam helicity response function $\sigma_{LT'}$ available, both for $p\pi^0$ ^{125–128} and for $n\pi^+$.¹²⁹ The most complete data sets will come from JLab for both the $\bar{e}p \rightarrow ep\pi^0$, and the $\bar{e}p \rightarrow en\pi^+$ channels. Some response functions at few low Q^2 have also been measured at MIT-Bates and Mainz. In particular, the experiments using the OOPS of MIT-Bates yield rather precise data of A_{TT} and A_{TL} at $Q^2 = 0.126$ (GeV/c)² covering a limited angular range. In Table 2, we summarize these new data.

One of the main outcomes from the analyses of these single pion production data is a more detailed understanding of the $\Delta(1232)$ resonance. The focus has been on the determination of the magnetic M1, electric E2, and Coulomb C2 form factors of the $\gamma N \rightarrow \Delta$ transition. This development will be discussed in detail in this section. The single pion production in the second and third resonance regions will be covered mainly in Sec. 5.3 where some N^* parameters extracted from a combined analysis including the data of η production will be discussed.

5.1.1. Pion photoproduction

The high statistics of the photon asymmetry data is essential in determining the small E_{1+} amplitude of the $\gamma N \rightarrow \pi N$ reaction, which determines the electric E2

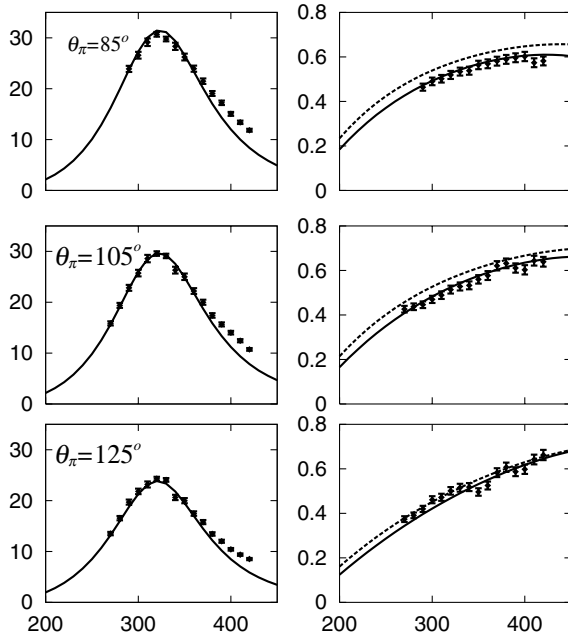


Fig. 8. The differential cross-section ($d\sigma/d\Omega$, left panel) and photon asymmetry (Σ , right panel) of the $p(\gamma, \pi^0)p$ reaction, calculated from the Sato-Lee model, are compared with the data of Mainz.¹¹¹ The photon asymmetry data of LEGS¹¹⁰ agree with those shown here and hence are not displayed. The dashed curves are obtained from setting $R_{EM} = 0$. The dashed and solid curves for $d\sigma/d\Omega$ are indistinguishable. The photon energy in MeV is labelled on the x -axis.

strength of the $\gamma N \rightarrow \Delta$ transition through Eq. (100). Figure 8 shows the comparison of the results from the Sato-Lee (SL) model⁶⁸ and the $\gamma p \rightarrow p\pi^0$ data from Mainz and LEGS. When the E_{1+} amplitude is turned off in the SL model, the predicted photon asymmetries (dotted curves) deviate from the data. By performing the amplitude analyses of these new data by several groups, we now have a world averaged value of the R_{EM} ratio, defined by Eq. (102), $R_{EM} = (-2.38 \pm 0.27)\%$ ¹¹⁵ at photon point. The magnetic M1 transition strength, defined by Eq. (99), has also been determined as $G_M^*(0) = 3.18 \pm 0.04$.

For the dynamical models, it is possible to also get the bare transition strengths $G_M(0)$ and $G_E(0)$ which are obtained by separating the pion cloud effects from the full (dressed) transition strengths, as defined by Eq. (84) and illustrated in Fig. 7. In Table 3, we show the importance of the pion cloud. We see that the helicity amplitude $A_{3/2}$ extracted from three different analyses are very close to each other and are about 40% larger than the bare strengths extracted within the dynamical models of Refs. 68 and 71. We now note that these bare values are within the ranges predicted by two constituent quark models. This suggests that the bare parameters of the dynamical model are more likely to be identified with the current hadron structure calculations. In Table 3 we also see that the differences between

Table 3. Helicity amplitude $A_{3/2}$ and E2/M1 ratio R_{EM} for the $\gamma N \rightarrow \Delta$ transition at $Q^2 = 0$ photon point. $A_{3/2}$ is in unit of $10^{-3} \text{ GeV}^{-1/2}$ and R_{EM} in %.

	$A_{3/2}$		R_{EM}		Refs.
	Dressed	Bare	Dressed	Bare	
Dynamical model	-258*	-153	-2.7	-1.3	68
	-256	-136	-2.4	0.25	71
K-matrix	-255	–	-2.1	–	55
Dispersion	-252	–	-2.5	–	50
Quark model	–	-186	–	~ 0	101
	–	-157	–	~ 0	19

*This value differs from the value 226 listed in Ref. 68, because of a kinematic factor is not included correctly.

dressed and bare values of R_{EM} are even larger. The bare values from two dynamical model analyses are quite different, indicating some significant differences in their formulations as discussed in Sec. 4.

5.1.2. Pion electroproduction

As can be seen in Table 2, pion electroproduction data are now very extensive and of high quality. In Figs. 9, 10 and 11, we show some sample data from CLAS at JLab. As an example for a spectrum with high statistics data on π^0 electroproduction at a fixed backward angle of $\theta_{\pi^0}^{\text{cm}} = 170^\circ$ we show in Fig. 12 response functions recently obtained from JLab Hall A.¹¹⁷

In Figs. 9 and 11, the predictions from the SL, MAID, and DMT models are also displayed to illustrate the status of current reaction models. The analyses of these new data in the past few years have led to rather accurate determinations of the $\gamma N \rightarrow \Delta$ transition form factors. We now discuss this advance in more detail.

5.1.3. The $\gamma N \rightarrow \Delta(1232)$ transition form factors

With the fairly extensive coverage over angles and energies, the data from JLab have allowed nearly model-independent determinations of $\gamma N \rightarrow \Delta(1232)$ form factors. These analyses by the CLAS collaboration are based on the following considerations. At the Δ peak, the dominant amplitude is M_{1+} and the small E_{1+} and S_{1+} can become accessible through their interference with the dominant M_{1+} amplitude. One thus can start the analysis by using a truncation, in which only terms involving M_{1+} are retained. With the partial-wave decomposition defined by Eqs. (35)–(40), the differential cross-section in Eq. (17) can then be written as

$$\frac{d\sigma}{d\Omega^*} = \sum_{\ell=0}^2 A_\ell P_\ell(\cos \theta^*) + \left[\sum_{\ell=1}^2 B_\ell P'_\ell(\cos \theta^*) \right] \cos \phi_M + [C_2 P_2''(\cos \theta^*)] \cos 2\phi_M. \quad (110)$$

The coefficients of the above equation are related to $|M_{1+}|^2$ and its projection onto the other s- and p-wave multipoles E_{1+} , S_{1+} , M_{1-} , E_{0+} , S_{0+} :

$$|M_{1+}|^2 = A_0/2, \quad (111)$$

$$\text{Re}(E_{1+}M_{1+}^*) = (A_2 - 2C_2/3)/8, \quad (112)$$

$$\text{Re}(M_{1-}M_{1+}^*) = -[A_2 + 2(A_0 + C_2/3)]/8, \quad (113)$$

$$\text{Re}(E_{0+}M_{1+}^*) = A_1/2, \quad (114)$$

$$\text{Re}(S_{0+}M_{1+}^*) = B_1, \quad (115)$$

$$\text{Re}(S_{1+}M_{1+}^*) = B_2/6. \quad (116)$$

The partial wave coefficients of Eq. (110) are determined by fitting the differential cross-section data such as those displayed in Figs. 9–11. From the relations Eqs. (111)–(116), one then obtains the M_{1+} , E_{1+} and S_{1+} amplitudes for determining the $\gamma N \rightarrow \Delta$ form factors through Eqs. (99)–(101).

The results from using the above procedure must be corrected for the systematic errors due to the truncation of higher multipoles. This can be accomplished by calculating the effects of higher partial waves using a realistic parametrization of the higher mass resonances and a realistic model for the background amplitudes. For not too large Q^2 values, this method results in reliable multipoles.

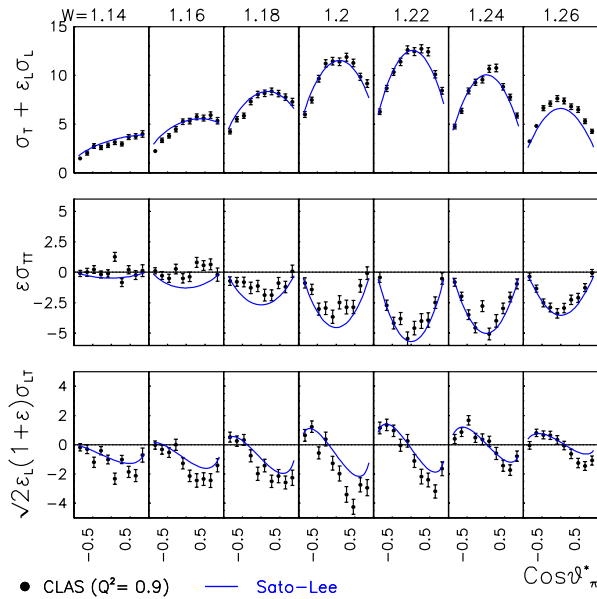


Fig. 9. $p(e, e' \pi^0)$ cross-section data from CLAS at JLab are compared with the predictions from the SL Model.

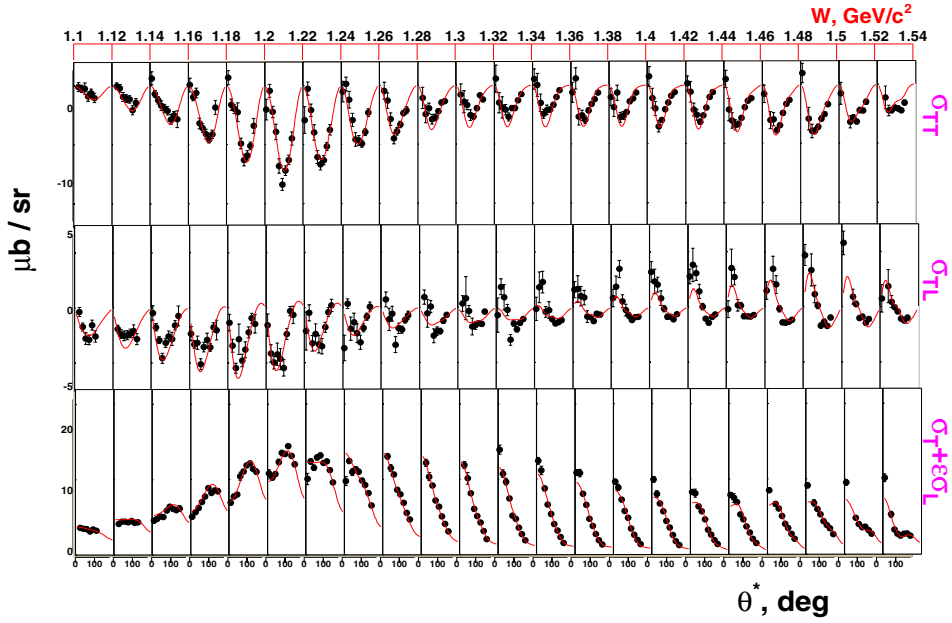


Fig. 10. $ep \rightarrow e n \pi^+$ data from CLAS. Separated response functions $\sigma_T + \epsilon\sigma_L$, σ_{TT} , and $\sigma_{TT} + \epsilon\sigma_{LL}$ are shown. The curve represents a fit to the data using the JLab/Yeveran unitary isobar model.

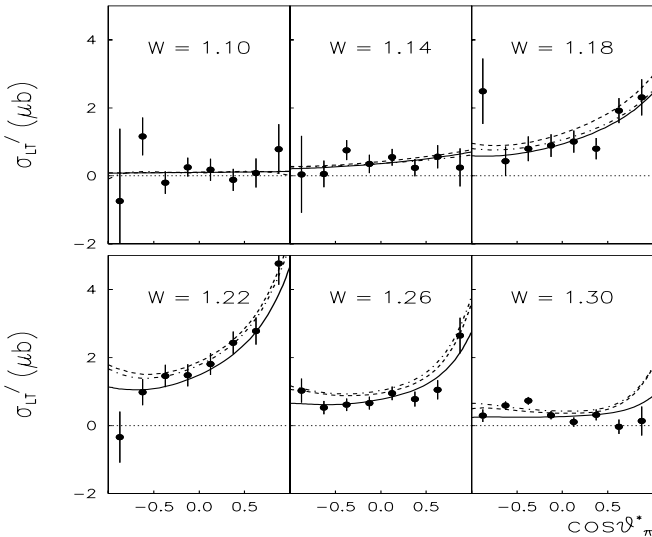


Fig. 11. CLAS data on σ_{TT}' of $p(e, e' \pi^+) n$ reaction in the $\Delta(1232)$ region are compared with predictions from SL (solid), MAID (dashed), and DMT (dashed-dotted) models.

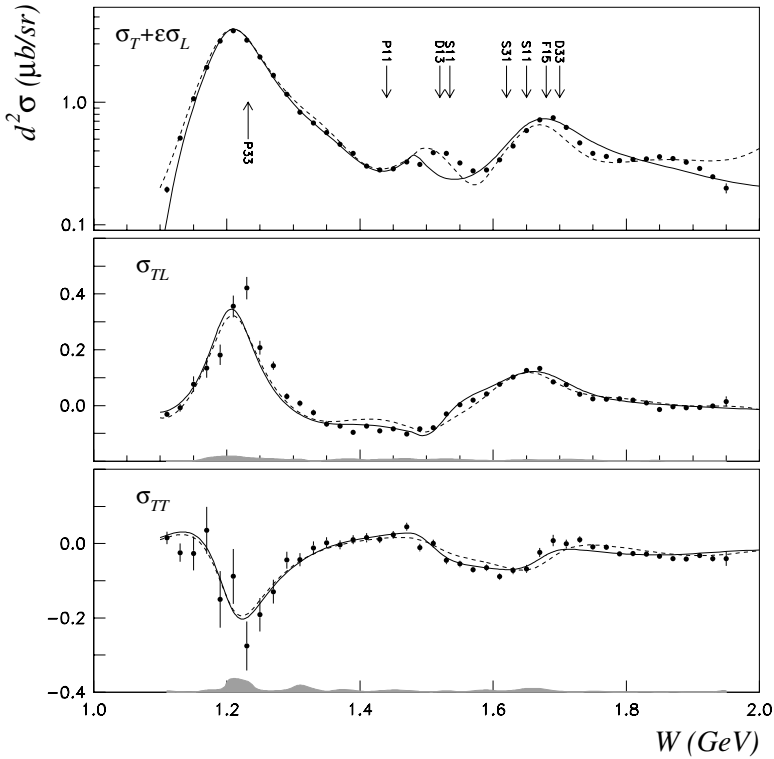


Fig. 12. Unpolarized response functions for $p\pi^0$ at $\theta_{\pi^0}^{\text{cm}} = 170^\circ$ from JLab Hall A. The solid line corresponds to a fit to the data using the MAID03 implementation. The dashed line corresponds to the SAID solution.

With the above largely model-independent procedure, results for G_M^* up to $Q^2 = 6 \text{ GeV}^2$ and the ratios R_{EM} and R_{SM} , defined in Eqs. (102) and (103), up to $Q^2 = 4 \text{ GeV}^2$ have been obtained at JLab and are compared with various theoretical predictions in Figs. 13 and 14. We now explain how the displayed results from SL, MAID, and DMT models are obtained. Within the MAID model, the Q^2 -dependence of the $\gamma N \rightarrow N^*$ transition strengths \bar{A}^α of Walker's parameterization Eq. (64) is determined from fitting the differential cross-section data. The resulting multipole amplitudes are then used to extract the $\gamma N \rightarrow \Delta$ form factors by using Eqs. (99)–(101). On the other hand, within the SL and DMT dynamical models, the parameters of the bare quantities $G_M(Q^2)$, $G_E(Q^2)$ and $G_C(Q^2)$, defined by Eq. (93), are adjusted to fit the data. The dressed form factors of the SL model are then predicted by using Eq. (84) to calculate the meson cloud effect. As shown in Ref. 68, at the Δ mass $W = 1.232 \text{ GeV}$ this procedure is equivalent to that based on Eqs. (99)–(101). The parameters of these three models have been determined by using the data up to $Q = 4 \text{ GeV}^2$. The results at $Q^2 > 4 \text{ GeV}^2$ are their predictions.

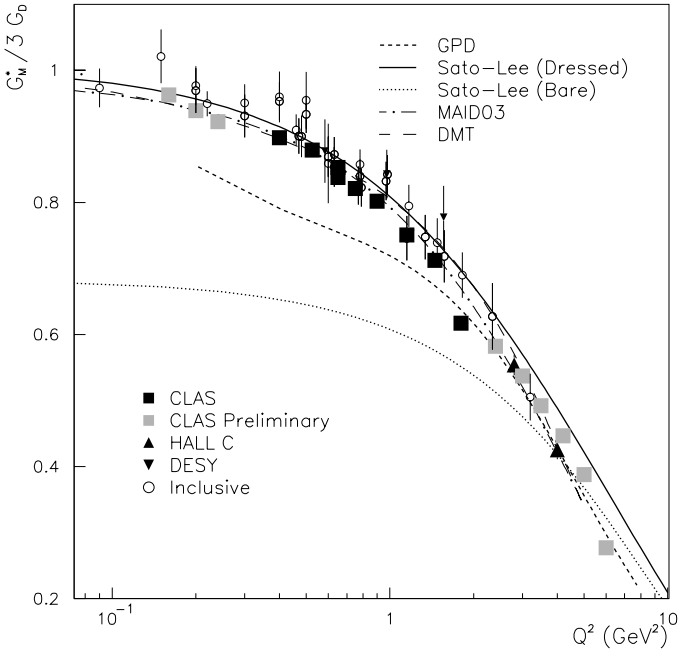


Fig. 13. The data of magnetic form factor G_M^* for the $\gamma N \rightarrow \Delta(1232)$ transition are compared to various models. Results from old single arm electron scattering experiments are labeled “inclusive.” All other results have been obtained from a multipole expansion of exclusive π^0 production from protons.

In Fig. 13, we see that the theoretical predictions of $G_M^*(Q^2)$ at $Q^2 > 4$ (GeV/c) 2 from SL, MAID and DMT models agree well with the new data from Jlab. The prediction by Stoler,¹¹⁸ which is based on a PQCD-motivated model, is also displayed there for comparison. It also agrees well with the data at relatively high Q^2 .

The dotted curve in Fig. 13 is obtained from setting the pion cloud effect, defined by Eq. (84) and illustrated in Fig. 7, to zero within the Sato-Lee model. We see that the pion cloud effect is very large at low Q^2 , but becomes much smaller at high Q^2 . Clearly this Q^2 dependence plays an important role in getting the agreement with the data up to $Q^2 = 6$ GeV 2 . It will be interesting to see whether the predicted pion cloud effect will agree with the data at even higher Q^2 .

In the upper part of Fig. 14, we see that the preliminary CLAS data¹³⁸ for R_{EM} at low $Q^2 < 0.2$ (GeV) 2 are in good agreement with the predictions from the SL and DMT models. On the other hand, the new Jlab data for the ratio R_{SM} (lower part of Fig. 14) in the low $Q^2 < 0.2$ GeV 2 region prefers the prediction from the SL model. The data points at $Q^2 = 0.127$ GeV 2 from MAMI and Bates have a larger magnitude for R_{SM} . These data points were used by DMT in fixing their parameterization for $G_C(Q^2)$. It should be noted that the points from MAMI and Bates are not the result of an independent multipole fit, but are from data sets with a more limited angle coverage fitted to the MAID parametrization. One of the

data sets from MIT-Bates is shown in Fig. 15. Clearly, only very limited angles are covered. Nevertheless, these data are very useful in revealing the non-zero values of the G_E and G_C form factors within the dynamical model, as illustrated in the difference between the solid and dotted curves.

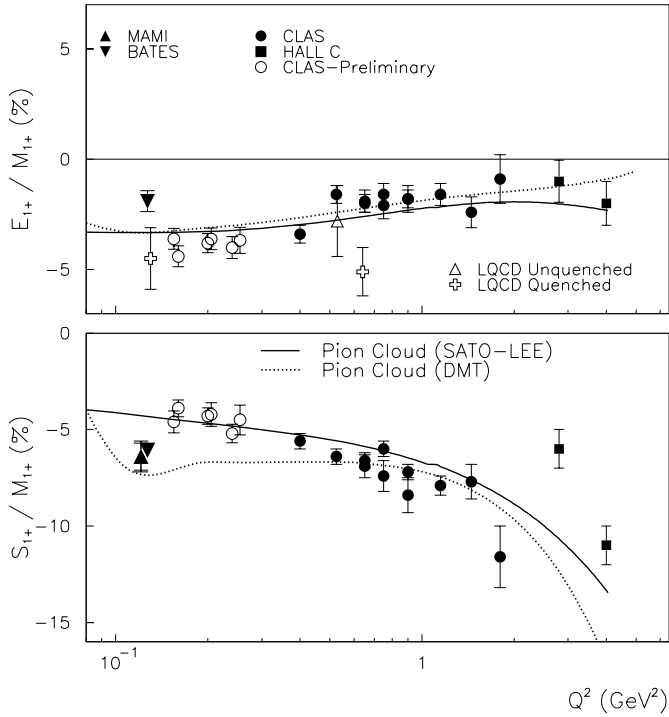


Fig. 14. Ratios R_{EM} (denoted as E_{1+}/M_{1+}) and R_{SM} (denoted as S_{1+}/M_{1+}) for the $\gamma N \rightarrow \Delta(1232)$ transition. These two ratios are related to the $E_{1+}^{3/2}$, $S_{1+}^{3/2}$, and $M_{1+}^{3/2}$ multipole amplitudes of $\gamma^*N \rightarrow \pi N$, as defined in Eqs. (102) and (103). Preliminary data from CLAS at low Q^2 are also included.

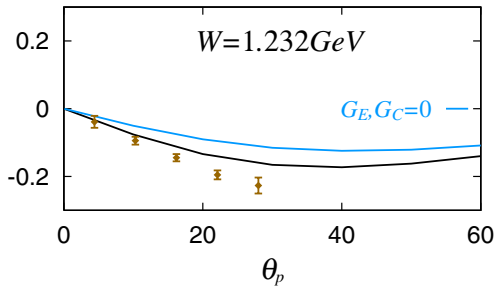


Fig. 15. The data of A_{LT} from MIT-Bates are compared with the results from the Sato-Lee model. The dashed curve is obtained from setting the G_C and G_E of the $\gamma N \rightarrow \Delta$ form factor to zero.

We now note that the ratios R_{EM} and R_{SM} calculated from the dynamical models are very much related to the predicted pion cloud effects. These are illustrated in Fig. 16 from the SL model. We see that the pion cloud effect can strongly enhance the $E_{1+}^{3/2}$ and $S_{1+}^{3/2}$ amplitudes of $\gamma^*N \rightarrow \pi N$ at low Q^2 . As defined in Eqs. (99)–(101), these two amplitudes are related to the $G_E(Q^2)$ and $G_C(Q^2)$ of the $\gamma N \rightarrow \Delta$ transition. The non-trivial pion cloud effects shown in Fig. 16 are clearly verified by the JLab data, as seen in Fig. 14.

To further improve the determination of the $\gamma N \rightarrow \Delta$ form factors, data of polarization observables must be included in the theoretical analyses. Measurements using a polarized electron beam and/or a longitudinally polarized hydrogen target¹³⁶ have yielded data of double spin beam-target asymmetry A_{et} and target asymmetry A_t . Samples of asymmetry data from CLAS are shown in Fig. 17. The double polarization asymmetry A_{et} is largely given by the well determined M_{1+} multipole and is well described by all models. However, significant differences can be seen in the A_t asymmetry which is sensitive to interferences between the

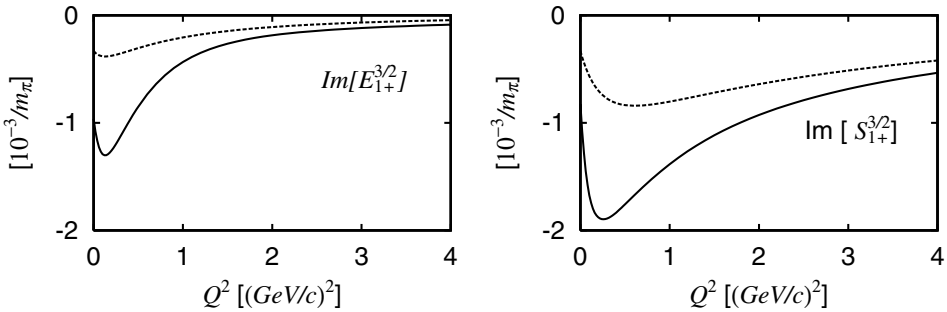


Fig. 16. The imaginary parts (Im) of the $E_{1+}^{3/2}$ and $S_{1+}^{3/2}$ calculated from the Sato–Lee model. The dotted curves are obtained from setting the pion cloud effect to zero.

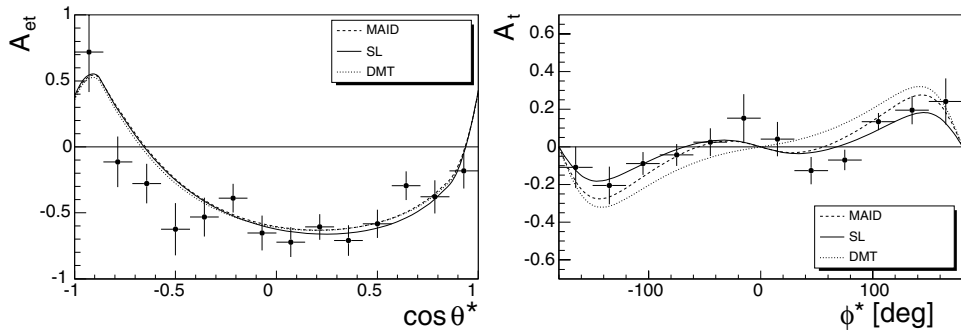


Fig. 17. A_{et} and A_t from JLab at $W = 1.225$ GeV, $Q^2 = 0.46$ GeV² are compared with the predictions from SL, MAID, and DMT models. The left panel is integrated in a range $\phi = (144^\circ, 160^\circ)$. The right panel is integrated in a range $\cos \theta^* = (-0.6, -0.8)$.

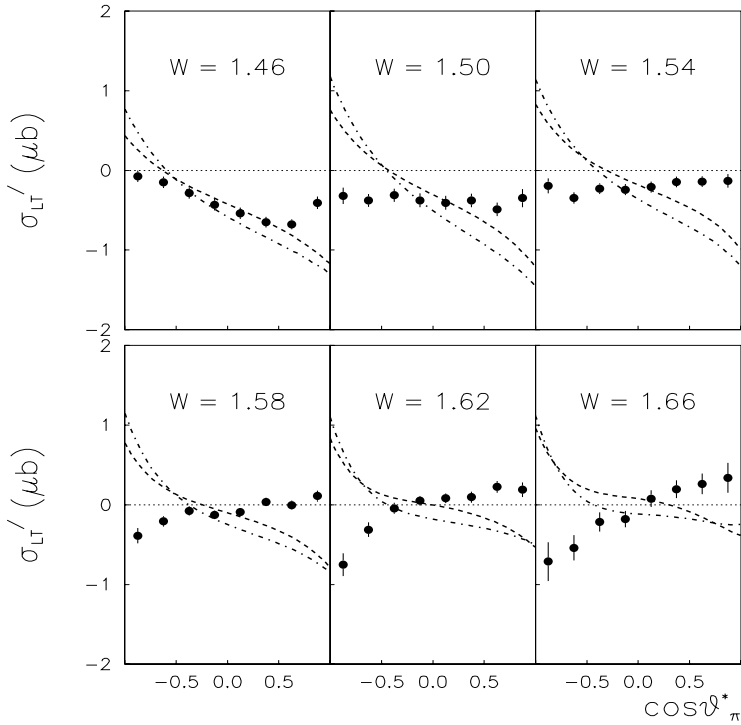


Fig. 18. The data of σ'_{LT} for $\gamma^*p \rightarrow p\pi^0$ in the 2nd resonance region are compared with MAID (dashed) and the DMT (dashed-dotted) predictions.

non-resonant and resonant amplitudes. The discrepancy in the model descriptions can be attributed to their different treatments of the non-resonant amplitudes, as discussed in Sec. 4.

Extensive pion electroproduction data in the second and third resonance regions have also been obtained using CLAS. Some typical results are shown in Fig. 18. Here we see that the displayed theoretical predictions do not agree well with the data at $W > 1.4$ GeV. This is not surprising since the parameters of these single-channel models are fixed by mainly fitting the data at $W < 1.4$ GeV. Recently, fits to these higher W data have been achieved by using a single-channel K-matrix model and fixed- t dispersion relations. In these analyses $p\pi^0$ and $n\pi^+$ data are fitted simultaneously using unpolarized cross-section data as well as beam spin response function results. It has been found that these very different approaches give consistent results, e.g. in the analyses of Aznauryan *et al.*⁵³ It indicates that the model-dependence may be relatively small. Nevertheless, the extracted resonance parameters must be taken with caution before a rigorous investigation of the coupled-channel effect has been carried out. Progress in this direction is being made.⁷⁶ The results of these fits are discussed in Sec. 5.3.

5.2. Photoproduction and electroproduction of η mesons

In contrast to the pion with isospin $I = 1$, the eta is an isoscalar meson with no charged partners. As such it can only couple with nucleons to form $I = 1/2$ resonances. This makes the production of η 's from nucleon targets an ideal tool to separate isospin $\frac{1}{2}$ N^* resonances from isospin $\frac{3}{2}$ Δ^* resonances. The total photoproduction cross-section, shown in Fig. 19, exhibits a rapid rise just above threshold, indicative of a strong s-wave contribution near threshold. This behavior is known to be due to the first negative parity nucleon resonance, the $S_{11}(1535)N_{1/2^-}$, which couples with approximately 55% to the $N\eta$ channel.¹⁴⁰ The nearby $D_{13}(1520)$ has a branching ratio of much less than 1% to this channel.^b The next higher mass nucleon resonance with a significant $N\eta$ coupling is the $P_{11}(1710)$, nearly 200 MeV/ c^2 higher in mass. This fact makes the production of η 's from nucleon targets the reaction of choice for detailed studies of the electromagnetic transition from the ground state to the $S_{11}(1535)$. The $N\eta$ channel effectively isolates this state from other nearby resonances, similar to the $\Delta(1232)$, which is well separated from higher mass resonances in the $p\pi^0$ channel. In distinction to the $\Delta(1232)$, whose electromagnetic transition form factors drop rapidly with increasing photon virtuality Q^2 , the $S_{11}(1535)$ remains a prominent resonance even at the highest Q^2 that are currently accessible.

In the following subsections we discuss the status of the electromagnetic production of η 's from nucleons, and analyses to extract the photocoupling helicity amplitudes for the $\gamma N \rightarrow S_{11}(1535)$ transition, and their Q^2 evolution. We finally compare the results with model predictions. Table 4 gives an overview of the kinematics covered in recent η production measurements.^{141,142,144–147,150–153}

Table 4. Summary of η production data.

Reaction	Observable	W range (GeV)	Q^2 range (GeV ²)	Lab
$\gamma p \rightarrow p\eta$	$d\sigma/d\Omega$	< 2.0		JLab-CLAS
	$d\sigma/d\Omega$	< 1.7		GRAAL
	$d\sigma/d\Omega$	< 2.3		ELSA-CB
	$d\sigma/d\Omega$	< 1.53		MAMI-TAPS
$\gamma(n/p) \rightarrow (n/p)\eta$	$d\sigma_n/d\sigma_p$	< 2.3		GRAAL
$\bar{\gamma}p \rightarrow p\eta$	Σ	< 2.3		GRAAL
$\gamma\bar{p} \rightarrow p\eta$	T	< 2.3		ELSA
$\bar{\gamma}\bar{p} \rightarrow p\eta$	E	< 1.53		MAMI-A2
$ep \rightarrow ep\eta$	$\sigma_{LT}, \sigma_{TT}, \sigma_T + \epsilon\sigma_L$	< 2.2	2.8–4.0	JLab-Hall-C
	$\sigma_{LT}, \sigma_{TT}, \sigma_T + \epsilon\sigma_L$	< 2.2	0.3–4.0	JLab-CLAS

^bEven though the $D_{13}(1520)$ coupling to $N\eta$ is very small, its close proximity to the $S_{11}(1535)$ causes large interferences with the dominant E_{0+} transition amplitude of the S_{11} . This in turn allows a precise determination of the $D_{13}(1520) \rightarrow N\eta$ branching ratio.

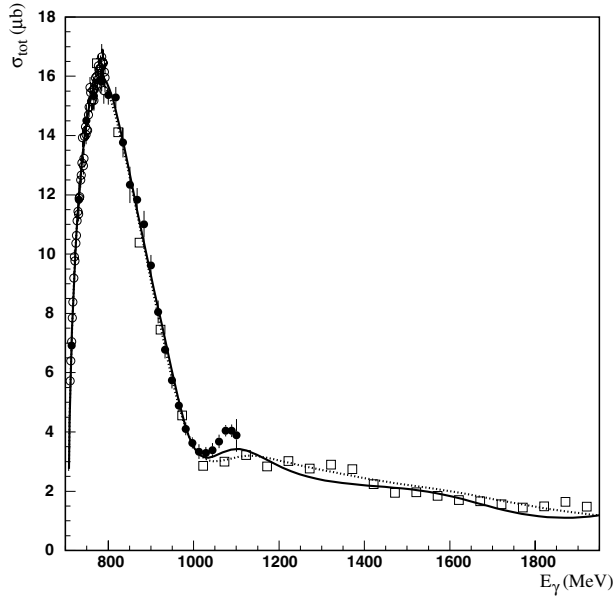


Fig. 19. Total cross-section for η photoproduction from protons. Data from MAMI (open circles), GRAAL (full circles), and CLAS (open squares) are shown. The curves are the fits explained in Sec. 5.2.4.

5.2.1. η photoproduction from protons

With the new measurements in recent years, the data base for η photoproduction reaction has been improved tremendously. The differential cross-section data now cover the $p\eta$ mass range up to $W = 2.3$ GeV, and are available for most of the angular range in the hadronic center-of-mass system. Some of these data are shown in Fig. 20. The data from all three experiments agree well. In the mass region of the $S_{11}(1535)$ resonance the angular distributions are nearly flat, indicating dominant s-wave components with only slight indications of higher partial wave contributions. In the mass region above 1.750 GeV, the angular distributions become increasingly forward-peaked, indicating significant non-resonant behavior presumably due to t-channel processes.

GRAAL has measured the beam asymmetries using laser light backscattered from the 6 GeV electrons to generate high-energy linearly polarized photons. The beam asymmetry Σ_γ is defined as

$$\Sigma_\gamma = \frac{1}{P_\gamma} \frac{\frac{d\sigma}{d\Omega}(\phi = 0^\circ) - \frac{d\sigma}{d\Omega}(\phi = 90^\circ)}{\frac{d\sigma}{d\Omega}(\phi = 0^\circ) + \frac{d\sigma}{d\Omega}(\phi = 90^\circ)}, \quad (117)$$

where P_γ is the photon polarization, ϕ is the azimuthal angle between the plane defined by the linear photon polarization and the hadronic plane defined by the

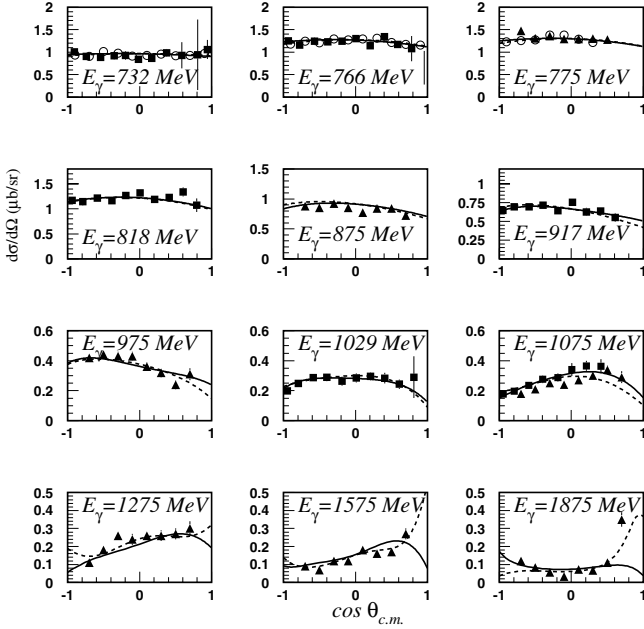


Fig. 20. Differential cross-section for $\gamma p \rightarrow \pi n$ from TAPS, GRAAL, and CLAS are shown for photon energies near threshold to 1.875 GeV. The curves are the fits explained in Sec. 5.2.4. The solid (dotted) line represents the UIM (DR) analysis.

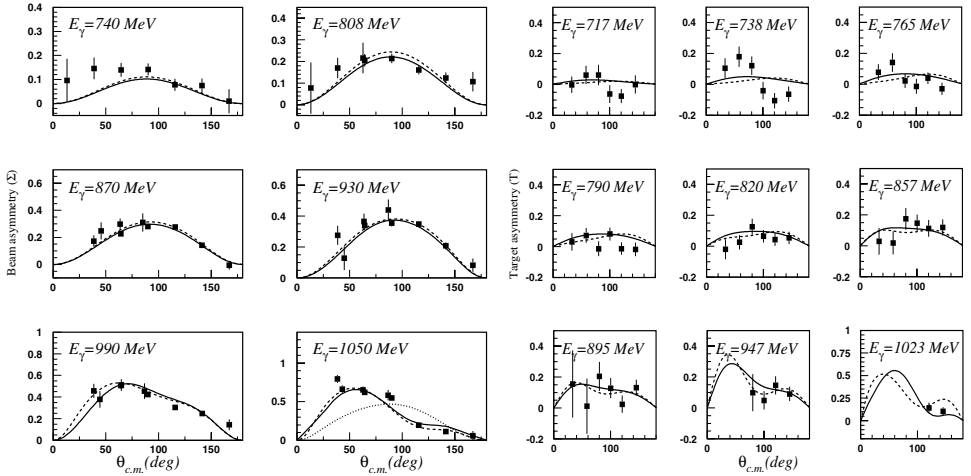


Fig. 21. The fits to the $\gamma p \rightarrow \pi n$ data using the Unitary Isobar Model (solid curves) and Dispersion Relation (short dashed curves) approaches. Left panel: Beam asymmetry measured at GRAAL. The dotted curve in the 1050 MeV panel shows the fit without the $F_{15}(1680)$ resonance. Right panel: Target asymmetry measured at ELSA.

photon beam and the $p\eta$ final state. The measured beam asymmetries are shown in Fig. 21. Just above the η threshold and at the resonance position Σ_γ shows a symmetric angular distribution, approximately following a $\sin^2\theta^*$ behavior, while at higher energies the asymmetry is more forward peaked. The $\sin^2\theta_\eta^*$ behavior near the resonance pole at the lower energies is prominent in the data, and is also reflected in the model descriptions included in Fig. 21.

Asymmetries have also been measured with a transversely polarized proton target at ELSA. The target asymmetry T is given by

$$T = \frac{1}{P_T} \frac{\frac{d\sigma}{d\Omega}(\uparrow) - \frac{d\sigma}{d\Omega}(\downarrow)}{\frac{d\sigma}{d\Omega}(\uparrow) + \frac{d\sigma}{d\Omega}(\downarrow)}. \quad (118)$$

The arrows indicate the direction of the proton polarization relative to the hadronic plane. Results are shown in the right panel in Fig. 21.

5.2.2. $\gamma p \rightarrow S_{11}(1535)$ parameters extracted from global fit to η photoproduction

The $S_{11}(1535)$ has long been known as a strong nucleon resonance with a large branching ratio to the $N\eta$ and $N\pi$ channels. However, there have been assertions that the strong enhancement near this mass is not due to the excitation of a resonance.¹⁵⁴ One model implies that the state is dominantly a dynamically generated $\Sigma\bar{K}$ resonance.¹⁵⁵ On the other hand, recent Lattice QCD calculations^{156,157} show that there is a strong 3-quark state at this mass with the spin-parity $J^P = \frac{1}{2}^-$, indicating that the $S_{11}(1535)$ is indeed an excited state of the nucleon.

The photocoupling amplitudes and their Q^2 dependence are powerful tools in determining the internal resonance structure and will help solve this controversy. For the purpose of this article we consider the $S_{11}(1535)$ as a baryon resonance with well defined quantum numbers. In the following we discuss results obtained in a global analysis of all observables in η photoproduction with the goal to extract the photocouplings amplitudes for resonances coupling to the $p\eta$ channel, especially the $S_{11}(1535)$.

A number of analyses have been performed on the $p\eta$ photoproduction channel.^{53,158,160} Here, we describe the recent global analysis by Aznauryan⁵³ as it allows one to also assess the model-dependence of the results. Differential cross-sections^{151,141} were included as well as polarized beam asymmetries,¹⁵² and polarized target asymmetries.¹⁴⁸ All established N^* resonances above the $N\eta$ threshold were included, i.e. $S_{11}(1535)$, $D_{13}(1520)$, $S_{11}(1650)$, $D_{15}(1675)$, $F_{15}(1680)$, $D_{13}(1700)$, $P_{11}(1710)$, $P_{13}(1720)$. The cross-section data are fitted for photon energies up to 2 GeV, corresponding to invariant masses in the range $W = 1.49$ – 2.15 GeV, i.e. covering the entire resonance region. The polarization data cover only the range up to $W = 1.7$ GeV. Figures 20 and 21 show samples of the fit

Table 5. $S_{11}(1535)$ photocoupling from global fit in units ($10^{-3} \text{ GeV}^{-1/2}$).

Resonance	Mass (MeV)	Γ (MeV)	$A_{1/2}^p$	Model
$S_{11}(1535)$	1527	142	96	Isobar model
	1542	195	119	Dispersion relations
	1520–1555	100–200	60–120	PDG estimate

to the cross-sections and asymmetry data. The Unitary Isobar Model (UIM) and Dispersion-Relations (DR) approaches give consistent results for the $S_{11}(1535)$, $D_{13}(1520)$, and $F_{15}(1680)$ resonances. The first result is the confirmation of a large photocoupling amplitude for the $S_{11}(1535)$, which is determined with good precision. The results are summarized in Table 5. They are compared with the range given by the PDG.²⁴ The new results are within the upper part of the range given by the PDG. The lower range in the PDG value comes from an analysis of pion production data by the George Washington University (GWU) group.¹⁴⁹ We note here that the results from the global fits are also in good agreement with a combined analysis of π and η electroproduction data. We will discuss this in Sec. 5.3.

From the fit to the differential cross-sections one can then also extract the total photo absorption cross-section for η production. The fit results are compared with the experimental data in Fig. 19. All three experiments agree well in the region where the $S_{11}(1535)$ resonance dominates, while there is a discrepancy near 1100 MeV photon energy. Since the angular distributions agree well, this discrepancy must be entirely due to different models used for the extrapolation into the unmeasured angular regions. This emphasizes the importance of measuring complete angular distributions which are now available.¹⁴²

The global analysis also incorporates the beam asymmetry in the fit. To illustrate the sensitivity of Σ to contributions from the $D_{13}(1520)$ we express Σ_γ in the approximation that only S-waves, P-waves, and D-waves with spin $J \leq \frac{3}{2}$ contribute as:¹⁵⁹

$$\Sigma_\gamma \approx \frac{3 \sin^2 \theta \text{Re}[E_{0+}^*(E_{2-} + M_{2-})]}{|E_{0+}|^2}. \quad (119)$$

This expression can be fitted to the measured beam asymmetry Σ_γ . Using E_{0+}^* from fits to the cross-section data, the multipoles E_{2-}^η , M_{2-}^η for the $D_{13}(1520)$ can then be determined. Since the corresponding pion multipoles E_{2-}^π , M_{2-}^π are known with high precision from pion production, the branching ratio $\beta_{\eta N}$ can be extracted. The analysis also allows one to extract the $N\eta$ branching ratio for the $F_{15}(1680)$ by analyzing the forward-backward asymmetry in Σ_γ seen in Fig. 21 at $E_\gamma \approx 1 \text{ GeV}$. The dotted curve in the figure for 1050 MeV (left panel) shows the fit when the small $F_{15}(1680)$ amplitudes are turned off. Clearly, the interference effects strongly enhance this contribution. The results for the $D_{13}(1520)$ and $F_{15}(1680)$ are summarized in Table 6. Both results represent significantly improved values for the branching ratios.

Table 6. Summary of η photoproduction global fit results. The uncertainty in $\beta_{\eta N}$ reflects the model dependence in using the unitary isobar model and dispersion relation approach.

Resonance	Mass (MeV)	Γ (MeV)	$\beta_{\eta N}$ (%)	$\beta_{\pi N}$ (%)
D ₁₃ (1520)	1520	120	0.05 ± 0.02	50–60
F ₁₅ (1680)	1675	130	0.15 ± 0.03	60–70

5.2.3. Eta electroproduction

Eta electroproduction experiments have focussed on the Q^2 evolution of the $S_{11}(1535)$ transverse photocouplings amplitude $A_{1/2}(Q^2)$. Experiments at DESY^{161,162} and Bonn^{163,164} found a very slow falloff with Q^2 . Recent experiments at Jefferson Lab^{140,150,153} have studied this behavior in detail with high statistics, and also extended the kinematics range. Figure 22 shows samples of differential cross-sections measured with CLAS.¹⁵³ Even at the peak of the $S_{11}(1535)$ resonance the angular distributions are not completely flat indicating that higher partial waves are present in addition to the dominant S-wave. Figure 23 shows samples of total cross-sections at fixed Q^2 . In contrast to the $\Delta(1232)$, which rapidly drops with Q^2 , the $S_{11}(1535)$ remains prominent even at the highest Q^2 .

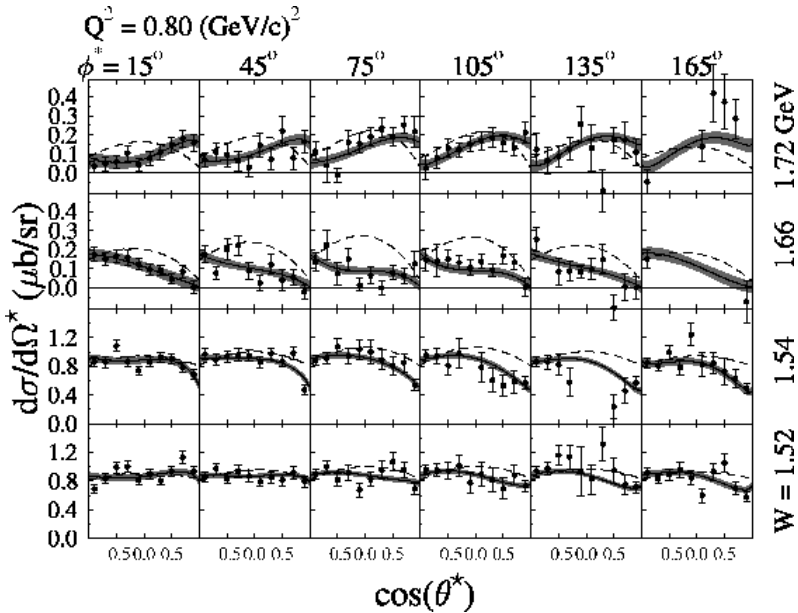


Fig. 22. Samples of differential cross-section for $\gamma^*p \rightarrow p\eta$ from CLAS at fixed $Q^2 = 0.8 \text{ GeV}^2$ and different W and ϕ values. The shaded bands indicate the fit results using 9 Legendre polynomials, as explained in Sec. 5.2.5. The dashed curve represents the predictions of η MAID.

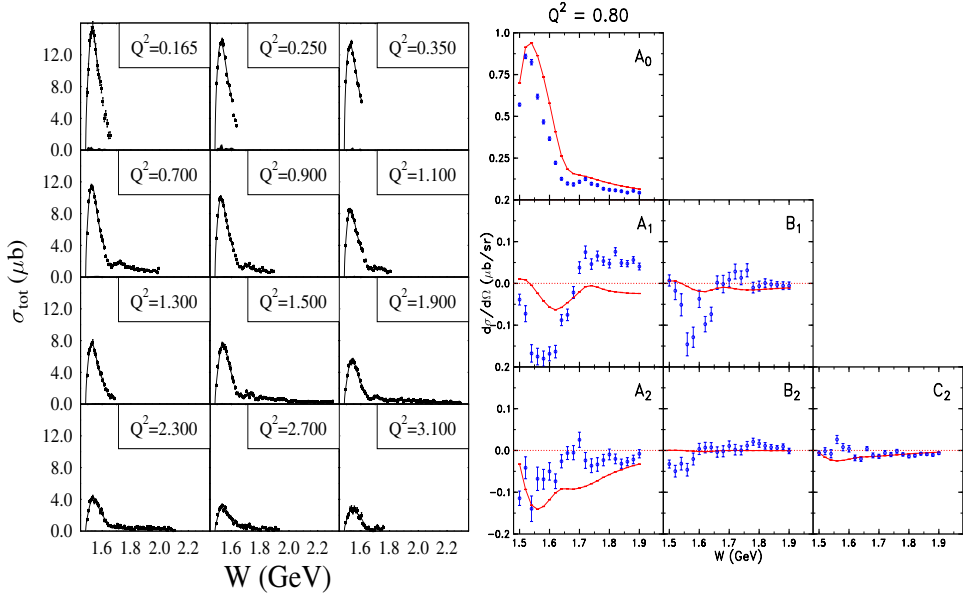


Fig. 23. Left panel: Total cross-section for $\gamma^*p \rightarrow p\eta$ versus W , at various photon virtualities Q^2 . The right panel shows partial wave fit parameters versus W compared to predictions of η MAID. All data are from CLAS.

Most of the published results on the Q^2 dependence of the $S_{11}(1535)$ transition amplitude have been obtained in single resonance fits. This has been justified with the dominant contributions of the $S_{11}(1535)$ to the $\gamma^*p \rightarrow p\eta$ cross-section. It is, however, not a fully satisfactory solution, as higher mass states that couple to $N\eta$ may also contribute in the lower mass region. The results have to be taken with caution. The differential cross-sections are fitted to the expression Eq. (17). The dependence on the η scattering angle (θ_η^*) can be examined by expanding each component of the differential cross-section in terms of Legendre polynomials:

$$\frac{d\sigma_T}{d\Omega_\eta^*} + \epsilon \frac{d\sigma_L}{d\Omega_\eta^*} = \sum_{\ell=0}^{\infty} A_\ell P_\ell(\cos\theta_\eta^*), \quad (120)$$

$$\sqrt{2\epsilon(\epsilon+1)} \frac{d\sigma_{LT}}{d\Omega_\eta^*} = \sum_{\ell=1}^{\infty} B_\ell P'_\ell(\cos\theta_\eta^*), \quad (121)$$

$$\epsilon \frac{d\sigma_{TT}}{d\Omega_\eta^*} = \sum_{\ell=2}^{\infty} C_\ell P''_\ell(\cos\theta_\eta^*). \quad (122)$$

If the expansion is limited to $\ell = 2$, only the coefficients A_0 , A_1 , A_2 , B_1 , B_2 and C_2 are retained. Results from the fit at fixed Q^2 are shown in the right panel of Fig. 23. Strong variations of A_1 and B_1 are seen in the W range from 1.6 to 1.7 GeV,

indicating large interference effects involving s- and p-waves. Possible p-wave candidates are the $P_{11}(1710)$ and $P_{13}(1720)$ states. A_0 is mostly due to the $S_{11}(1535)$ resonance and is by far the largest amplitude. The longitudinal and transverse response functions cannot be separated in this analysis. In earlier experiments^{162,164} the longitudinal and transverse cross-sections were separately determined at some fixed Q^2 values, showing that A_0 is dominated by the transverse amplitude $A_{1/2}^2$ in the Q^2 range of this study. The combined analysis of π and η electroproduction data, to be discussed in the next section, also finds small longitudinal contribution to A_0 . Assuming $\sigma_L = 0$, $|A_{1/2}|$ can be computed from A_0 . Figure 24 shows a compilation of results for the $\gamma p \rightarrow S_{11}(1535)$ photocouplings helicity amplitude $A_{1/2}(Q^2)$. The slow falloff with Q^2 confirms the unusually hard transition form factor that persists to the highest measured values of Q^2 . The solid and dotted curves are the prediction of Close and Li,¹⁷⁶ and of Giannini, Santopinto and Vassallo.¹⁷⁴ It should be noted that the absolute normalization of the data displayed in Fig. 24 is uncertain to the extent that the branching ratio $\beta_{N\eta}(S_{11}) = 0.55$ and a total widths of 150 MeV have been used in extracting $A_{1/2}$. The *Review of Particle Properties 2002* allows a large range of 0.30–0.55 for the branching ratio. However, the recent analysis of Armstrong *et al.*,¹⁴⁰ gives a value of $\beta_{N\eta}(S_{11}) \approx 0.55$. The use of this value is consistent with the values $\beta_{N\eta}(S_{11}) = 0.55$ and $\beta_{N\pi}(S_{11}) = 0.4$ used in the combined analysis of π and η electroproduction which is the subject of the next section.

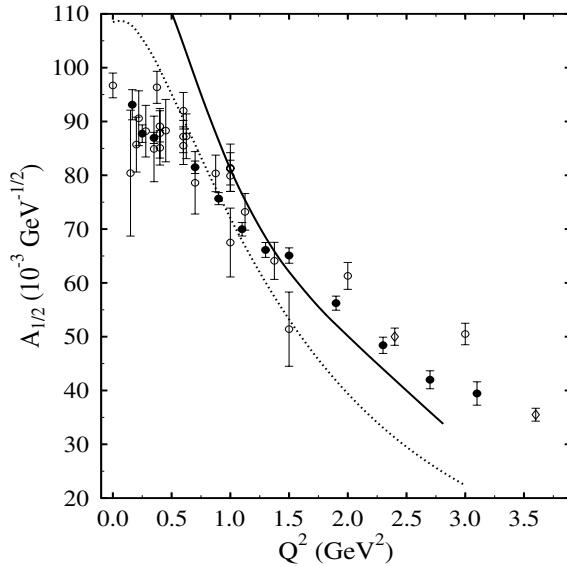


Fig. 24. Q^2 evolution of the $\gamma p \rightarrow S_{11}(1535)$ photocouplings amplitude $A_{1/2}$. The full symbols are the most recent CLAS results. The open diamonds are the JLab data from Hall C, and the open circles are from previous experiments. The solid curve is from Ref. (176), and the dotted curve is from Ref. (174).

5.3. Combined analysis of π and η electroproduction data

The large amount of data taken by the CLAS detector allows simultaneous measurements of cross-sections and polarization observables for several channels, e.g. $p\pi^0$, $n\pi^+$, $p\eta$. Also, the large acceptance provides complete angular distributions, including the full azimuthal dependence. The use of a highly polarized electron beam provides data on the helicity-dependent response function $\sigma_{LT'}$ covering the full angle range. Results of a MAID and DMT analysis of the channel $p\pi^0$ have recently been reported.¹³⁷ Combined analyses of these data in a multi-channel global fit provides much more stringent constraints on resonance parameters than single-channel analyses can. The full set of data taken with a hydrogen target have been analyzed within the unitary isobar model⁵² and the dispersion relation approach⁵³ described in Sec. 4. The data on $\sigma_{LT'}$ are especially sensitive to small resonance contributions in a large non-resonant background. The sensitivity is the result of the interference term that mixes real and imaginary amplitudes:

$$\sigma_{LT'} \sim \text{Im}(L) \cdot \text{Re}(T) + \text{Im}(T) \cdot \text{Re}(L), \quad (123)$$

where L and T represent the longitudinal and transverse amplitudes, respectively. Figure 25 shows the sensitivity of $\sigma_{LT'}$ to the $P_{11}(1440)$ multipoles M_{1-} and S_{1-} . Both channels show sensitivity to changes in the multipoles, however, the effect is much larger in the $n\pi^+$ channel. This is due to a combination of two factors, the stronger coupling of $I = 1/2$ nucleon states to the $n\pi^+$ channel, and the larger

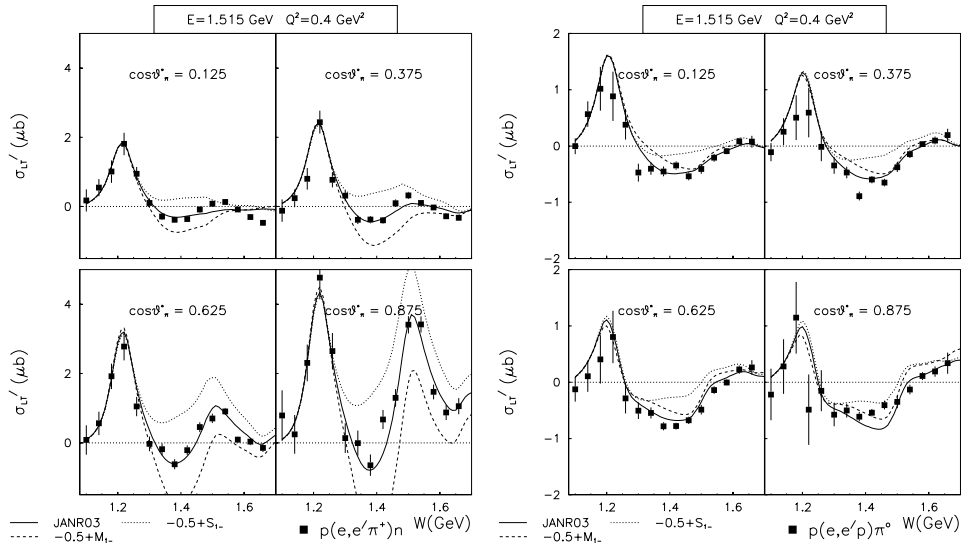


Fig. 25. Sensitivity of CLAS data of $\sigma_{LT'}$ to changes in multipoles $M_{1-}^{1/2}$ (dashed) and $S_{1-}^{1/2}$ (dotted) for the $n\pi^+$ channel (left) and $p\pi^0$ channel (right). Solid line shows best fit using the Unitary Isobar Model. The -0.5 in the legend refers to shifting the Breit-Wigner amplitude by $-0.5 \mu b^{1/2}$.

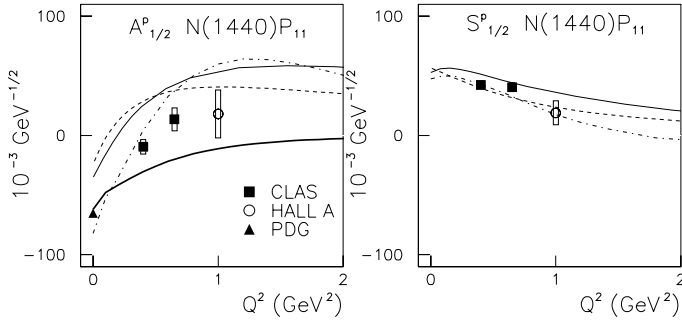


Fig. 26. Results for the $P_{11}(1440)$ amplitudes $A_{1/2}^p$ and $S_{1/2}^p$. CLAS points include the model error. The Hall A point shows MAID03 fit model error. The curves are described in the text.

background terms contributing to this channel. Using pion and eta production to study the same resonances, e.g. the $S_{11}(1535)$ allows tests of possible flavor-dependence of the results which could be significant if rescattering effects, such as those present in the $\Delta(1232)$ region, play an important role also for higher mass states. The use of two conceptually very different approaches also allow one to estimate the model-dependence of the resulting amplitudes. The results for the $P_{11}(1440)$ are shown in Fig. 26. For the first time a consistent trend is emerging: the magnitude of $A_{1/2}(Q^2)$ drops rapidly for $Q^2 > 0$, with a sign change near $Q^2 = 0.5 \text{ GeV}^2$. There is also a strong longitudinal coupling. Bold, solid, dashed and dot-dashed lines are from various calculations.^{170,172,173,175} Nonrelativistic quark models^{171,176} predict large negative $A_{1/2}(Q^2)$ in the entire Q^2 range, and do not describe the data. The hybrid model¹⁷⁰ describes the fast drop of $|A_{1/2}|$ qualitatively, but has no sign change, and predicts $S_{1/2}(Q^2) = 0$, while the data show a sizeable $S_{1/2}$ amplitude. The relativistic models of Capstick and Keister¹⁷² and of Cardarelli and Simula¹⁷³ predict the sign change for $A_{1/2}(Q^2)$ but show a much faster rise than is observed. The magnitudes and trends of both amplitudes are well described by a model that describes the $P_{11}(1440)$ with a small quark core and a $q\bar{q}$ cloud.¹⁷⁵ In this model, the low Q^2 behavior is entirely due to the $q\bar{q}$ contribution while the qqq core defines the high Q^2 behavior. The results for the $S_{11}(1535)$ are depicted in Fig. 27. They show consistent results for $A_{1/2}$ in the $p\eta$ and the $N\pi$ channels for the Unitary Isobar Model (UIM) and Dispersion-Relation (DR) analyses. Also, for the first time, stable results for the longitudinal coupling $S_{1/2}$ have been obtained. The solid and dotted curves in Fig. 27 represent quark model calculations using a harmonic oscillator potential¹⁷⁶ and a hypercentral potential,¹⁷⁴ respectively.

The results of the global fit for $A_{1/2}$, $A_{3/2}$ and $S_{1/2}$ for the $D_{13}(1520)$ are shown in Fig. 28. Both the UIM and DR analyses give consistent results. To summarize, the inclusion of polarization observables in addition to the differential cross-section into a global analysis results in a less model-dependent description of π and η photoproduction and electroproduction processes in the resonance region. There

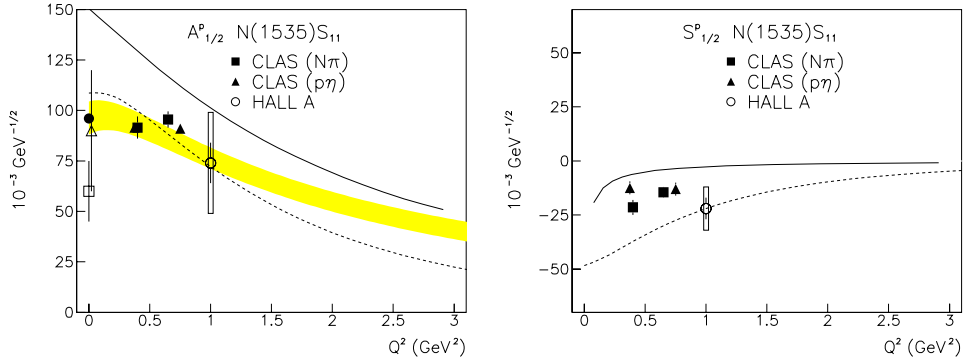


Fig. 27. Q^2 evolution of the $S_{11}(1535)$ photocoupling amplitudes $A_{1/2}(Q^2)$ (left), and $S_{1/2}(Q^2)$ (right). Cross-section data from $p\eta$, $p\pi^0$, and $n\pi^+$ have been used, as well as polarized beam response function $\sigma_{LT}^{\pi^+}$, and $\sigma_{LT}^{\pi^0}$. The shaded band indicates the uncertainties seen in previous analysis using $p\eta$ cross-section data. Solid and dotted lines are from quark model calculations described in the text.

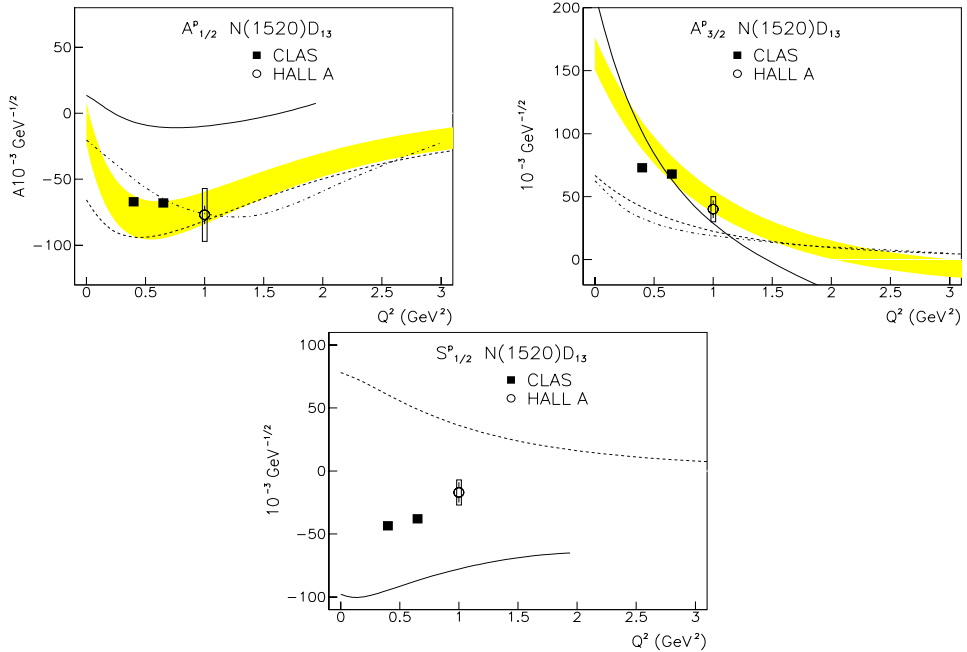


Fig. 28. Q^2 evolution of the $D_{13}(1520)$ photocoupling amplitudes $A_{1/2}$, $A_{3/2}$, and $S_{1/2}$. Cross-section data from $p\pi^0$, and $n\pi^+$ have been used, as well as polarized beam response function $\sigma_{LT}^{\pi^+}$ and $\sigma_{LT}^{\pi^0}$. The shaded bands indicate the uncertainties seen in previous analysis using mostly $p\pi^0$ cross-section data. The theoretical curves are explained in the text.

are several noteworthy results: First, consistent results are obtained for the mass of the $S_{11}(1535)$ for the η and π channel, both for photo- and electroproduction. The mass is in the range $M(S_{11}) = 1531 \pm 5$ MeV. Second, the discrepancy between η and π photoproduction results for $A_{1/2}$ amplitude seems to have been resolved. The analysis of electroproduction data gives also good agreement for the $p\eta$ and $N\pi$ channels and in both UIM and DR approaches. Third, the Q^2 evolution of the $A_{1/2}$ and $S_{1/2}$ amplitudes for the $P_{11}(1440)$ are consistent with the predictions of a meson cloud model. This is in line with what has been found earlier for the $N\Delta(1232)$ transition, that meson cloud effects can be sizeable for some of the resonance transitions.

5.3.1. Analysis of resonance transitions in the single quark transition model

Properties of nucleon resonances such as mass, spin-parity, and flavor fit well into the representation of the $SU(6) \otimes O(3)$ symmetry group, which describes the spin-flavor and orbital wave functions of the 3-quark system. This symmetry group leads to supermultiplets of baryon states with the same orbital angular momentum \vec{L} of the 3-quark system, and degenerate energy levels. Within a supermultiplet the quark spins are aligned to form a total quark spin \vec{s} , with $s = \frac{1}{2}, \frac{3}{2}$, which combines with the orbital angular momentum L to form the total angular momentum $\vec{J} = \vec{L} + \vec{s}$. A large number of explicit dynamical quark models have been developed to describe the electromagnetic transitions between the nucleon ground state and its excited states.^{168,171,172,174} Measurement of resonance transitions and the dependence on the distance scales, given by the virtuality of Q^2 of the photon, provides information on the nucleon wave function. In order to compute the transition, assumptions on the 3-quark potential and the quark-quark interactions have to be made. These are then tested by predicting photocoupling helicity amplitudes which can then be confronted with experimental data. Algebraic relations have been derived for resonance transitions assuming the transition only affects a single quark in the nucleon. The parameters in these algebraic equations can be determined from the experimental analysis.¹⁷⁷ Based on the symmetry properties of the Single Quark Transition Model (SQTM), predictions for a large number of resonances belonging to the same $SU(6) \otimes O(3)$ supermultiplet can be made. The fundamentals of the SQTM are described in Refs. 178 and 179, where the symmetry properties have been discussed for the transitions from the ground state nucleon $[56, 0^+]$ to the $[70, 1^-]$ and the $[56, 2^+]$ supermultiplets. The $[70, 1^-]$ contains states which are prominent in electromagnetic excitations, and it is the only supermultiplet for which sufficient data on resonance couplings of two states are available to extract the SQTM amplitudes and test predictions for other states. The coupling of the electromagnetic current is considered for the transverse photon component, and the quarks in the nucleon are assumed to interact freely with the photon. In such a model the quark transverse current can be written in general as a sum of four terms^{178–180}:

$$J^+ = AL^+ + B\sigma^+L_z + C\sigma_zL^+ + D\sigma^-L^+L^+, \quad (124)$$

where σ is the quark Pauli spin operator, and the terms with A , B , C , D in front operate on the quark spatial wave function changing the component of orbital angular momentum along the direction of the momentum transfer (z -axis). The A term corresponds to a quark orbit flip with $\Delta L_z = +1$, term B to a quark spin flip with $\Delta L_z = 0$, the C and D terms correspond to simultaneous quark orbit and quark spin flip with orbital angular momentum flips of $\Delta L_z = +1$ and $\Delta L_z = +2$, respectively. For the transition from the $[56, 0^+]$ to the $[70, 1^-]$ supermultiplet with $L = 1$, only A , B , and C are allowed. The relationship between the A , B , C amplitudes and the usual helicity photocoupling amplitudes $A_{1/2}$ and $A_{3/2}$ is listed in Table 7. Using the extracted photocoupling amplitudes from the $S_{11}(1535)$ and the $D_{13}(1520)$, the A , B , C amplitudes for the $\gamma + [56, 0^+] \rightarrow [70, 1^-]$ have been extracted.¹⁷⁷ The results are shown in Fig. 29. Knowledge of the three amplitudes and of two mixing angles for the transition to the $[70, 1^-]$ allows predictions for 16 amplitudes of states belonging to the same supermultiplet. If they can be confirmed for some of the amplitudes, one then has a measure of the degree to which electromagnetic transitions of nucleon resonance are dominated by single

Table 7. Helicity amplitudes for the electromagnetic transition from the ground state $[56, 0^+]$ to the $[70, 1^-]$ multiplet as a function of the SQTm amplitudes. θ is the mixing angle relating two $J^P = \frac{1}{2}^-$ states with $s_{3q} = \frac{3}{2}$ and $s_{3q} = \frac{1}{2}$. There is also a small mixing angle for the two $\frac{3}{2}^-$ states resulting in the physical states $D_{13}(1520)$ and $D_{13}(1700)$. We have not included the latter mixing angle in the table. Note that the excitation of the $D_{13}(1700)$ from a proton target is only possible because of $SU(6)$ symmetry breaking leading to the mixing with the lower mass $D_{13}(1520)$.

State	Proton target	Neutron target
$S_{11}(1535)$	$A_{1/2}^+ = \frac{1}{6}(A + B - C) \cos \theta$	$A_{1/2}^o = -\frac{1}{6}(A + \frac{1}{6}B - \frac{1}{3}C)$
$D_{13}(1520)$	$A_{1/2}^+ = \frac{1}{6\sqrt{2}}(A - 2B - C)$ $A_{3/2}^+ = \frac{1}{2\sqrt{6}}(A + C)$	$A_{1/2}^o = -\frac{1}{18\sqrt{2}}(3A - 2B - C)$ $A_{3/2}^o = \frac{1}{6\sqrt{6}}(3A - C)$
$S_{11}(1650)$	$A_{1/2}^+ = \frac{1}{6}(A + B - C) \sin \theta$	$A_{1/2}^o = \frac{1}{18}(B - C)$
$D_{13}(1700)$	$A_{1/2}^+ = 0$ $A_{3/2}^+ = 0$	$A_{1/2}^o = \frac{1}{18\sqrt{5}}(B - 4C)$ $A_{3/2}^o = \frac{1}{6\sqrt{15}}(3B - 2C)$
$D_{15}(1675)$	$A_{1/2}^+ = 0$ $A_{3/2}^+ = 0$	$A_{1/2}^o = -\frac{1}{6\sqrt{5}}(B + C)$ $A_{3/2}^o = -\frac{1}{6}\sqrt{\frac{2}{5}}(B + C)$
$D_{33}(1700)$	$A_{1/2}^+ = \frac{1}{6\sqrt{2}}(A - 2B - C)$ $A_{3/2}^+ = \frac{1}{2\sqrt{6}}(A + C)$	same same
$S_{31}(1620)$	$A_{1/2}^+ = \frac{1}{18}(3A - B + C)$	same

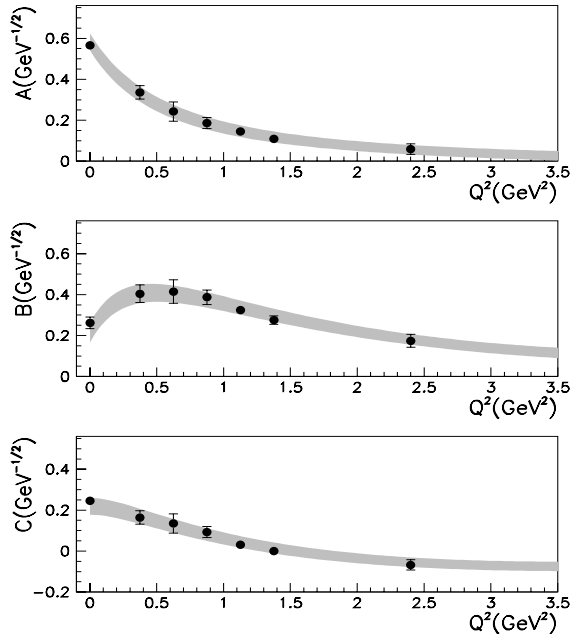


Fig. 29. Single quark transition amplitudes A , B , C as functions of Q^2 . The amplitudes have been extracted from the recent JLab, MAMI, and GRAAL data on the $S_{11}(1535)$ and world data on $D_{13}(1520)$ photocoupling amplitudes. The shaded band is a parameterization of the data from Ref. 177.

quark transitions at the photon point ($Q^2 = 0$) and, using electroproduction data, examine if and how this is changing as a function of the distance scale at increasing photon virtuality. The SQTm predictions for the proton and neutron amplitudes are shown in Fig. 30. There is remarkable agreement between the predictions and the data at the photon point. For electroproduction, there is good agreement where consistent data sets are available, i.e. for the $S_{11}(1650)$. Much improved electroproduction data are needed for more definite conclusions. Most of the states belonging to the $[70, 1^-]$ supermultiplet with masses near 1700 MeV couple strongly to $N\pi\pi$ channels. Studies of these channels require the use of large acceptance detectors and new, sophisticated analysis techniques. Progress made in these areas will be discussed in the next section. There are similar relations for the transition from the nucleon ground state to the members of the $[56, 2^+]$ supermultiplet. In this case four SQTm amplitudes can contribute. Unfortunately, the only state for which the two transverse photocoupling amplitudes have been measured in electroproduction is the $F_{15}(1680)$. This is insufficient to extract the four SQTm amplitudes.

5.4. Two-pion production

Two-pion channels dominate the electromagnetic meson production cross-sections in the second and third resonance regions where we hope to resolve the *missing*

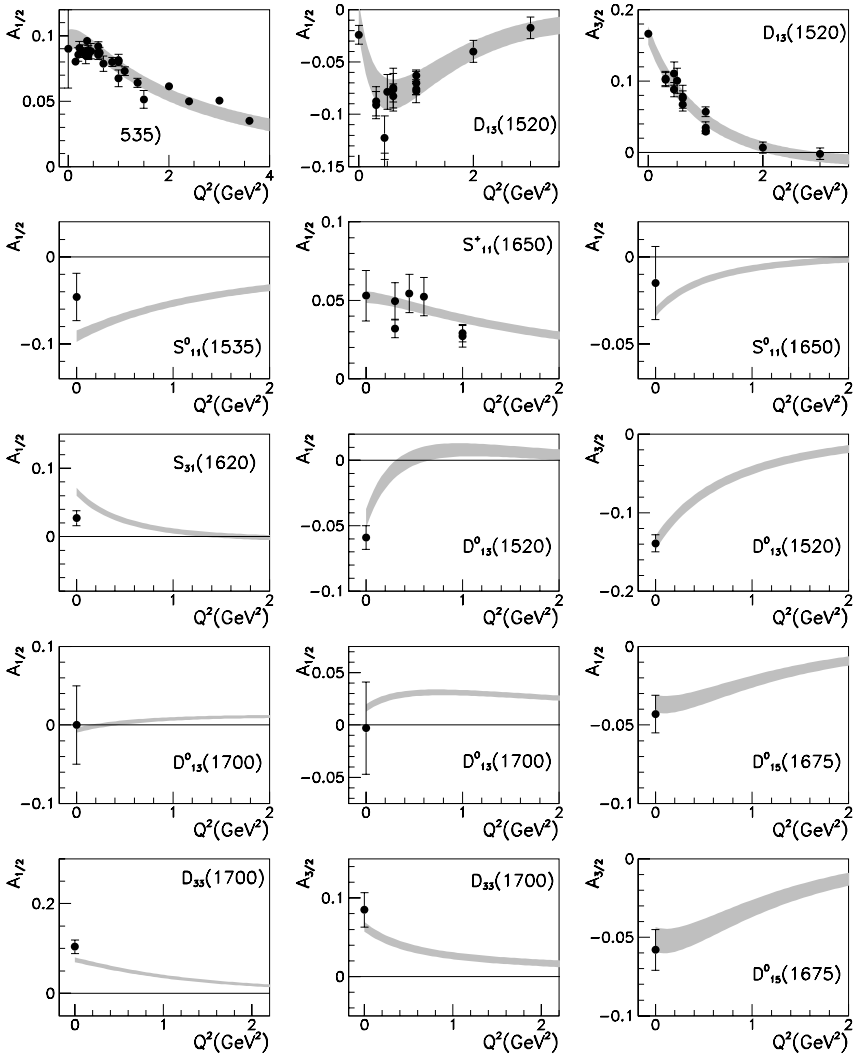


Fig. 30. Single quark model transition prediction for the $[70, 1^-]$ multiplet. The SQTM predictions are shown by the shaded band in comparison with the experimental data. At $Q^2 = 0$ the full circle is the Particle Data Group estimate. For $Q^2 > 0$, measurements from JLab, Bonn, DESY, and NINA in η and π electroproduction are shown. For the $S_{11}(1535)$, the results of an analysis of the world data in η -electroproduction presented in Ref. 150 are also included. The superscript “o” refers to neutron states.

resonance problem¹⁶⁸ and ultimately determine what basic symmetry group²⁰⁵ is underlying the baryon spectrum. Thus, a detailed understanding of two-pion production is very important in the N^* study, and has been pursued very actively in recent years. Very extensive two-pion production data have now been accumulated at JLab, MAMI and ELSA, but have not been fully analyzed and understood the-

oretically. Here we will mainly report on the status of the data and describe some very preliminary attempts to identify N^* states.

The study of $N\pi\pi$ channels requires the use of detectors with nearly 4π solid angle coverage for charged or neutral particle detection. Several such detectors have been in operation for a number of years, and have generated large data sets for the following reactions

$$\gamma p \rightarrow p\pi^0\pi^0, \quad (125)$$

$$\gamma p \rightarrow p\pi^+\pi^-, \quad (126)$$

$$ep \rightarrow ep\pi^+\pi^-. \quad (127)$$

The two-pion channels in the above processes can be projected onto various isobar channels which are more useful in identifying the nucleon resonances from the data. The $p\pi^+\pi^-$ final state is sensitive to the $\Delta^{++}\pi^-$ isobar channel which could have large sensitivity to resonance decays but has also very strong contributions from non-resonant mechanisms. The $p\pi^0\pi^0$ final state has the advantage of high sensitivity to resonance contributions with fewer non-resonant contributions. The $p\pi^+\pi^-$ channel is sensitive to the $p\rho^0$ isobar channel, while the $p\pi^0\pi^0$ channel does not couple to $p\rho^0$. Table 8 gives an overview of recent 2-pion production data obtained at various laboratories.

5.4.1. Analysis of the data with the $p\pi^+\pi^-$ final state

The quality of the recent data with the $p\pi^+\pi^-$ final state is very high. An example is shown in Fig. 31 for the differential cross-sections in one-dimensional projections. The data show evidence for the formation of the $\Delta^{++}\pi^-$, $\Delta^0\pi^+$, and $p\rho^0$ isobar channels. In the real photon case (left panel) the $p\rho^0$ contribution dominates the higher invariant mass (W) region. This contribution drops significantly for virtual photons (right panel). We also see that the π^- angular distribution is much more forward-peaked in the case of real photons, and becomes flatter with increasing Q^2 .

Table 8. Summary of $\gamma p \rightarrow p\pi\pi$ production data.

Reaction	Observable	W range (GeV)	Q^2 range (GeV ²)	Lab.
$\gamma^* p \rightarrow p\pi^+\pi^-$	$\sigma_{\text{tot}}, M_{p\pi^+}, M_{\pi^+\pi^-}, \frac{d\sigma}{d\cos\theta_{\pi^-}}$	< 2.1	0.65–1.3	CLAS ¹⁸³
		< 2.7	1.5–4.0	CLAS ¹⁸¹
$\gamma p \rightarrow p\pi^+\pi^-$	$\sigma_{\text{tot}}, M_{p\pi^+}, M_{\pi^+\pi^-}, \frac{d\sigma}{d\cos\theta_{\pi^-}}$	< 2.0	0	CLAS ¹⁸⁵
$\gamma p \rightarrow p\pi^0\pi^0$	$\sigma_{\text{tot}}, M_{p\pi^0}, M_{\pi^0\pi^0}$	< 1.9	0	GRAAL ¹⁸⁷
		< 1.55	0	MAMI ^{188,189}
$\gamma p \rightarrow p\pi^0\pi^0$	event-by-event analysis	< 2.6	0	CB-ELSA ¹⁸²

This behavior can be qualitatively understood as a consequence of vector meson photon duality. With increasing Q^2 the probability of the photon to fluctuate into a virtual vector meson is reduced leading to reduced diffraction-like scattering.

Although the high quality data of two-pion production are now available, the analysis in terms of extraction of resonance parameters has not been fully developed. The theoretical understanding of these complex processes, mainly based on the tree-diagram isobar approach,⁹⁰ is also very limited and preliminary. Recently, two distinctly different approaches have been applied to analyze the photoproduction and electroproduction data from JLab^{185,190} and CB-ELSA.¹⁸² The first approach is to adjust the parameters of an isobar model¹⁹⁰ to fit the fully extracted cross-section and polarization asymmetry data.^{190,191} The second one is to fit directly the unbinned data event-by-event.¹⁸² We describe them in the remaining part of this subsection.

The first approach makes use of knowledge from hadronic production. The energy-dependence of non-resonant processes is parameterized, and resonance photocouplings and hadronic couplings are fixed, if known, e.g. from single pion processes. Resonances in specific partial waves can be introduced to search for undiscovered states. Model parameters are usually fitted to the one-dimensional projections of the multi-dimensional differential cross-section. Such a model can lead to a qualitatively good description of the projected data as shown in Fig. 31. The method has been used in the analysis of CLAS electroproduction data¹⁸³. In this analysis a significant discrepancy was found near $W = 1.7$ GeV between the data and the resonance parametrizations implemented in the fit model. This discrepancy was attributed to either inaccurate hadronic couplings for the well known $P_{13}(1720)$ resonance determined in the analysis of hadronic experiments, or to an

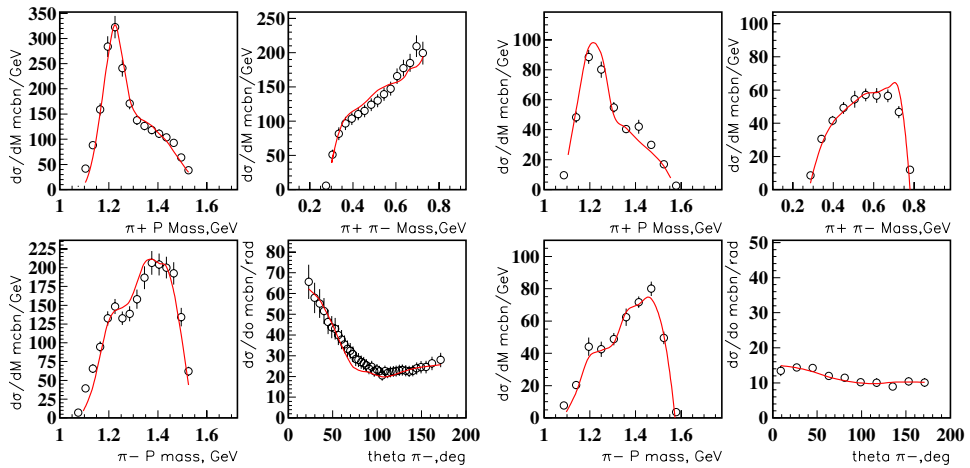


Fig. 31. One-dimensional projections for the $\gamma p \rightarrow p\pi^+\pi^-$ reaction cross-sections. Left: $Q^2 = 0$. Right: $Q^2 = 0.95 \text{ GeV}^2$. Both data set are from CLAS. Curves are explained in the text.

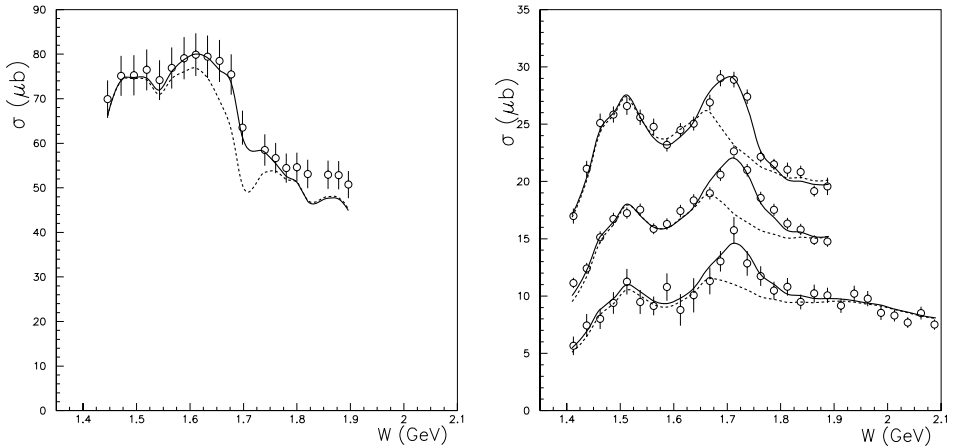


Fig. 32. Total cross-section for photoproduction (left) and electroproduction (right) of $p\pi^+\pi^-$ at $Q^2 = 0.65, 0.95, 1.30\text{GeV}^2$ (from the top). Data sets are from CLAS. Curves are explained in the text.

additional resonance with $J^P = \frac{3}{2}^+$ with either $I = \frac{1}{2}$ or $I = \frac{3}{2}$. The discrepancy is best visible in the total cross-sections for electroproduction, shown in Fig. 32. The dotted line shows the model predictions using resonance parameters from single pion electroproduction and from the analysis of $\pi N \rightarrow N\pi\pi$ data.^{24,58,63} The solid line represents the fit when the hadronic coupling of the $P_{13}(1720)$ to $\Delta\pi$ and $N\rho$ are allowed to vary much beyond the ranges established in the analysis of hadronic data. Alternatively, a new state was introduced with hadronic couplings extracted from the data. Table 9 summarizes results of the analysis using a single P_{13} with modified hadronic couplings, and a new P_{I3} state with undetermined isospin while keeping the PDG $P_{13}(1720)$ hadronic couplings unchanged. In either case, the fit requires a resonance with hadronic couplings that are significantly different from the ones of the $P_{13}(1720)$ state listed by PDG.

The total photoproduction cross-section in the left panel of Fig. 32 shows a W dependence that is very different from the electroproduction data in the right panel. In particular, the photoproduction has a much higher non-resonant contribution largely due to increased non-resonant ρ^0 production at the photon point. Both data are, however, consistent with a strong resonance near $W = 1.72$ GeV in the

Table 9. PDG parameters for the $P_{13}(1720)$ and parameters resulting from fits to $p\pi^+\pi^-$ electroproduction data.

	Mass (MeV)	Γ (MeV)	$\Gamma_{\pi\Delta}/\Gamma$ (%)	$\Gamma_{N\rho}/\Gamma$ (%)
PDG P_{13}	1725 ± 20	114 ± 19	63 ± 12	19 ± 9
PDG	1650–1750	100–200	—	70–85
New P_{I3}	1720 ± 20	88 ± 17	41 ± 13	17 ± 10

P_{13} partial wave.¹⁸⁴ The drawback of the approach described above is that when fitting one-dimensional projections of cross-sections, correlations between the data sets are lost.

The second approach¹⁸⁵ is based on a partial wave formalism starting from the T-matrix at a given photon energy E :

$$\begin{aligned}
 T_{fi}(E) &= \langle p\pi^+\pi^-; \tau_f | T | \gamma p; E \rangle \\
 &= \sum_{\alpha} \langle p\pi^+\pi^-; \tau_f | \alpha \rangle \langle \alpha | T | \gamma p; E \rangle \\
 &= \sum_{\alpha} \psi^{\alpha}(\tau_f) V^{\alpha}(E), \tag{128}
 \end{aligned}$$

where α denotes all intermediate states, and τ_f characterizes the final state kinematics. The decay amplitude $\psi^{\alpha}(\tau_f) = \langle p\pi^+\pi^-; \tau_f | \alpha \rangle$ is calculated using an isobar model for specific decay channel, e.g. $\Delta^{++}\pi^-$, $\Delta^-\pi^+$, or $p\rho^0$. The production amplitude $V^{\alpha} = \langle \alpha | T | \gamma p; E \rangle$ is then fitted at fixed energy using an unbinned maximum likelihood procedure. This method makes use of all information contained in the data, and takes into account all correlations between the variables.

In this analysis a total of 35 partial waves were included in addition to t-channel processes with adjustable parameters. Figure 33 shows intensity distributions in different isobar channels, for the $\frac{5}{2}(m = \frac{1}{2})$, and $\frac{3}{2}(m = \frac{1}{2})$ partial waves. Clear signals of the $F_{15}(1680)$ and the $P_{33}(1600)$ are seen, the latter being a not fully established 3-star resonance. In the final analysis the energy-dependence is fitted to a Breit–Wigner form to determine masses and widths of resonant states. This method is closer to a model-independent approach, and can directly ‘discover’ new resonances in specific partial waves.

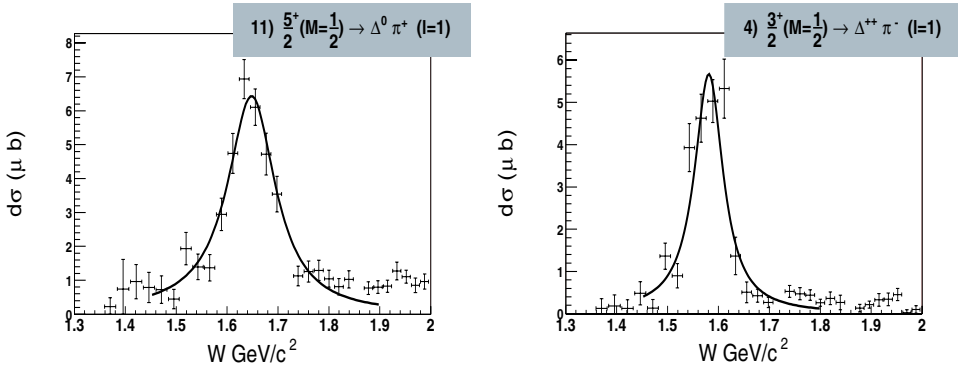


Fig. 33. Preliminary results of a partial wave analysis in the $\gamma p \rightarrow p\pi^+\pi^-$ showing the $m = \frac{1}{2}$ spin projections for the well-known $F_{15}(1680)$ (left), and evidence for the poorly known $P_{33}(1600)$ (right).

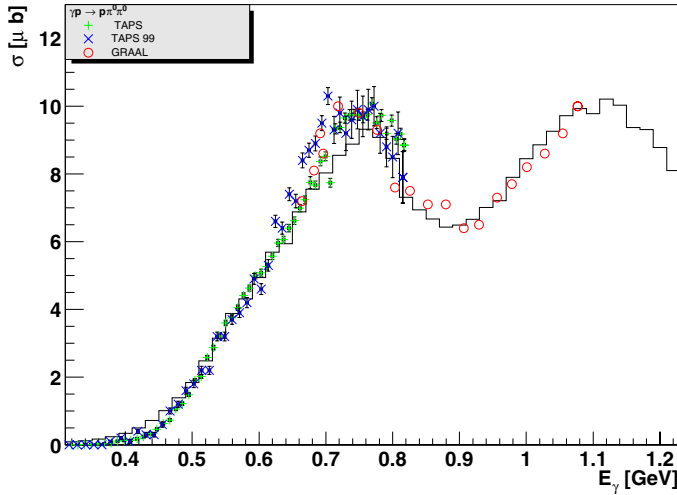


Fig. 34. Total cross-section of $\gamma p \rightarrow p\pi^0\pi^0$ reaction. The connected line is from the preliminary results of a partial wave analysis. The data are from the measurements with TAPS and GRAAL.

5.4.2. Description of $\gamma p \rightarrow p\pi^0\pi^0$ in resonance analyses

The CB-ELSA collaboration has analyzed the $p\pi^0\pi^0$ final state using a more model-dependent version of the partial-wave-analysis described above. Here s-channel Breit–Wigner distributions are fitted to the data on an event-by-event basis, therefore retaining the correlations in the data. However, the fit is constrained by the parametrized energy-dependence of the Breit–Wigner function. In Fig. 34 the total cross-section for $\gamma p \rightarrow \pi^0\pi^0$ is shown as extracted from the integral over all partial waves contributions in comparison to previous data from TAPS¹⁸⁸ and GRAAL.¹⁸⁷

5.5. Kaon production

Production of kaons from nucleons has long been recognized as a potentially very sensitive tool in the search for excited baryon states.¹⁰² Analyses of the $K\Lambda$ and $K\Sigma$ channels include the isospin selectivity; the $K\Lambda$ final state selects isospin $\frac{1}{2}$, similar to the $N\eta$ channel, while $K\Sigma$ couples to both N^* and Δ^* resonances. An important tool in resonance studies is the measurement of polarization observables. The self-analyzing power of the weak decay $\Lambda \rightarrow p\pi^-$ can be utilized to measure the Λ recoil polarization. To make full use of this unique feature large acceptance detectors are needed.

For a long time, the lack of consistent data sets for $K\Lambda$ and $K\Sigma$ production in a wide kinematics range has hampered the use of kaon production in the study of non-strange baryon resonances. Moreover, the interpretation of these data, mainly for charged $K^+\Lambda$ and $K^+\Sigma^0$ channels, in terms of N^* excitation is complicated by the fact that they may be dominated by the non-resonant particle-exchange processes. Another drawback in comparison to $N\pi$ and $N\pi\pi$ is the relatively small cross-

section, and the lack of known strong resonances with a dominant coupling to kaon-hyperon channels. This fact makes it more difficult to use strangeness production as a tool in the study of excited baryons, and specifically in the search for new resonances.

Most of the available theoretical models^{79–84,192–194} for kaon production are based on the tree-diagrams approach, as described in Sec. 4.2. The validity of these tree-diagram models is questionable, as discussed, for example, in a coupled-channel study⁷⁴ of kaon photoproduction. We will therefore mainly focus on the status of the data, not on the results from these theoretical models.

5.5.1. Photoproduction of $K^+\Lambda$ and $K^+\Sigma$

High statistics data of kaon photoproduction covering the resonance region are now available from the SAPHIR¹⁹⁵ and the CLAS¹⁹⁶ collaborations. These new data consist of high statistics angular distributions as well as Λ polarization asymmetries, as summarized in Table 10.

There are significant discrepancies between the CLAS data and the published SAPHIR¹⁸⁶ data, while the new data from SAPHIR¹⁹⁵ are in much better agreement with the CLAS data. We therefore disregard the earlier published data from SAPHIR. Unfortunately, most of the model calculations have been fitted to the published results, and therefore cannot be reliably compared to the new data.

The angular distributions for $K^+\Lambda$ and $K^+\Sigma$ production are shown in Fig. 35. We see that the $K^+\Lambda$ data (left panel) show a strong forward peaking for photon energies greater than 1 GeV, indicating the large t-channel contributions. For the $K^+\Sigma^0$ channel (right panel) the angular distribution are more symmetric or

Table 10. Summary of hyperon photo- and electroproduction data.

Reaction	Observable	W range (GeV)	$\cos \Theta_K^*$ range	Q^2 (GeV ²)	Experiment
$\gamma p \rightarrow \Lambda K$	$d\sigma/d\Omega$	< 2.15	$-0.95+0.95$		SAPHIR ¹⁸⁶
	$d\sigma/d\Omega$	< 2.6	$-0.95+0.95$		SAPHIR ¹⁹⁵
	$d\sigma/d\Omega$	< 2.3	$-0.85+0.85$		CLAS ¹⁹⁶
$\gamma p \rightarrow \Sigma K$	$d\sigma/d\Omega$	< 2.15	$-0.95+0.95$		SAPHIR ¹⁸⁶
	$d\sigma/d\Omega$	< 2.6	$-0.95+0.95$		SAPHIR ¹⁹⁵
	$d\sigma/d\Omega$	< 2.3	$-0.85+0.85$		CLAS ¹⁹⁶
$\gamma p \rightarrow K^+\bar{\Lambda}, \bar{\Sigma}$	P	< 2.3	$-0.85+0.85$		CLAS ¹⁹⁶
	P	< 2.6	$-0.95+0.95$		SAPHIR ¹⁹⁵
$ep \rightarrow eK^+\Lambda, \Sigma$	$\sigma_{LT}, \sigma_{TT}, \sigma_T + \epsilon\sigma_L$	< 2.5	$-1.0+1.0$	< 3	CLAS ¹⁹⁸
$\bar{e}p \rightarrow eK^+\Lambda$	P'_x, P'_z	< 2.15	$-1.0+1.0$	$0.3-1.5$	CLAS ¹⁹⁹

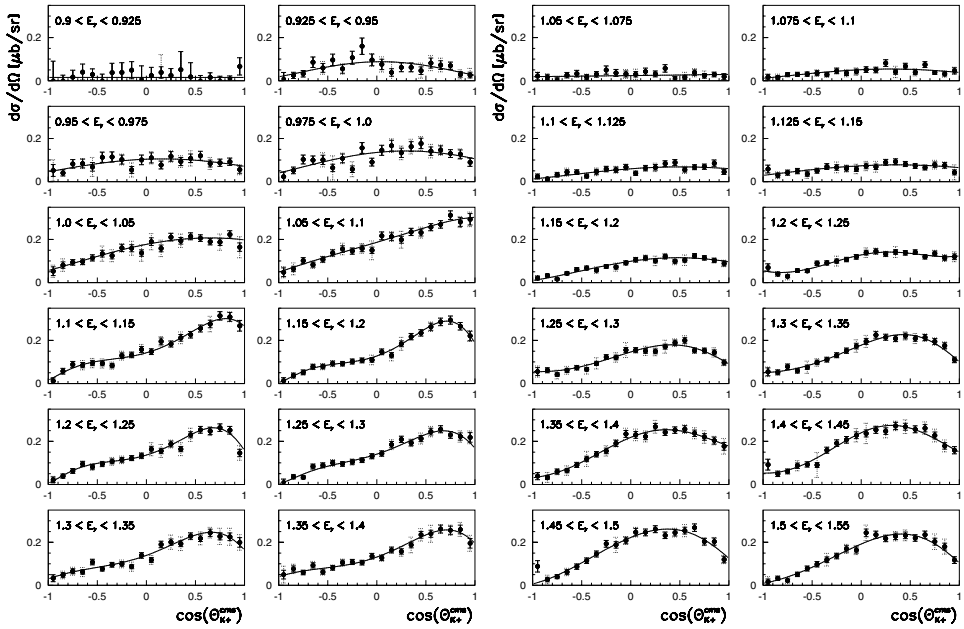


Fig. 35. Left: Angular distributions of $K^+\Lambda$ photoproduction at fixed photon energy E_γ . Right: $K^+\Sigma^0$ angular distributions. Both data sets are from SAPHIR. The lines represent Legendre fits to the data.

“resonance-like” at low energies, but become somewhat more forward-peaked at energies above 1.3 GeV.

The high statistics of these data allows one, for the first time, to identify the structures in the differential cross-section that hint the interference between the resonances and the nonresonant background. The presence of s-channel resonances is particularly evident in the W -dependence of the differential cross-section shown in Fig. 36. At the most forward angles (upper panel), two resonance-like structures are visible at $W \approx 1.7$ GeV, and at $W \approx 1.95$ GeV. The structure at 1.7 GeV could be accommodated by the known states $S_{11}(1650)$, $P_{11}(1710)$, and $P_{13}(1720)$, if the KA coupling of these states is allowed to vary. From hadronic processes these couplings are very poorly known.²⁴ At intermediate angles (middle panel) the data indicate a smoother falloff with W , while at backwards angles (lower panel) another resonance-like structure near $W \approx 1.875$ GeV emerges, overlapping with the structure at the higher mass. These distributions reveal complex processes, indicating contributions from more than a single resonance near $W = 1.9$ GeV.

Samples of the Λ polarization measured with CLAS are shown in Fig. 37. The data show a strong W dependence especially at backward angles (upper panel). Comparing the displayed data at two angles, we can conclude that the angle distributions of the Λ polarization change sign from largely negative at forward angles to positive at backward angles.

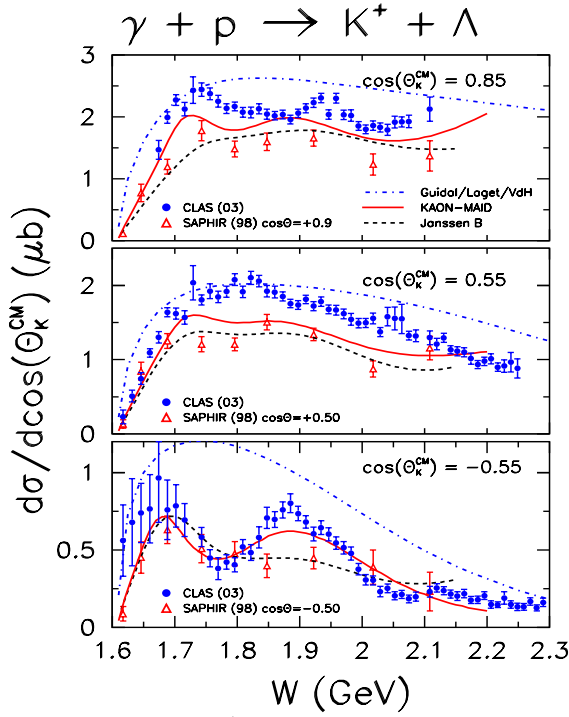


Fig. 36. W -dependence of $K^+\Lambda$ production for several bins in $\cos \theta_K^*$. Points with full circles are from CLAS. The triangles are older data from SAPHIR. The theoretical curves are from Ref. 200 (Guidal/Laget/vdH), Ref. 193 (KAON-MAID), and Ref. 194 (Janssen).

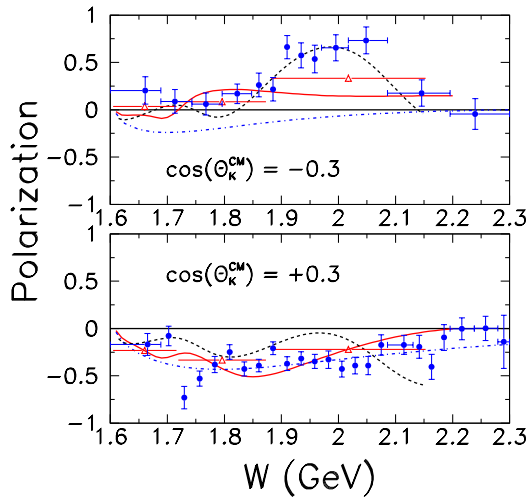


Fig. 37. Λ polarization in $K^+\Lambda$ photoproduction measured with CLAS. The theoretical curves are the same as those displayed in Fig. 36.

The three theoretical results displayed in Figs. 36 and 37 only describe very qualitatively the main features of the data in the region of the nucleon resonance region.

5.5.2. Electroproduction of $K^+\Lambda$ and $K^+\Sigma$

Kaon electroproduction is another tool in the study of non-strange nucleon resonances. While the $K^+\Lambda$ and $K^+\Sigma^0$ photoproduction cross-section exhibits a complex structure of resonant and nonresonant contributions that is difficult to disentangle, some of the resonance contributions in electroproduction may be enhanced at higher Q^2 due to their slower form factor fall-off compared to other resonances, and compared to the background amplitudes. A significant amount of data has become available recently from CLAS.^{197,199} In these experiments the electron beam is polarized, and hence the virtual photon also has a net circular polarization.

Figure 38 shows samples of the $K^+\Lambda$ production cross-sections integrated over either the forward hemisphere (left panel) and backward hemisphere (right panel) at fixed Q^2 . The results reveal resonant behavior near $W = 1.7$ GeV and 1.87 GeV at large angles while at the forward angles the resonant structures are masked by the large non-resonant contributions. The enhancements in the cross-section appear in the same invariant mass W range as in photoproduction, and are likely due to the same resonances contributions.

The data of Λ recoil polarization have been obtained in measurements with polarized electron beams. The measured total Λ recoil polarization can be written as

$$\vec{P}_\Lambda = \vec{P}^\circ \pm P_e \vec{P}', \quad (129)$$

where P_e is the electron beam polarization, \vec{P}° is the *induced* polarization which is present without beam polarization, and \vec{P}' is the *transferred* polarization.

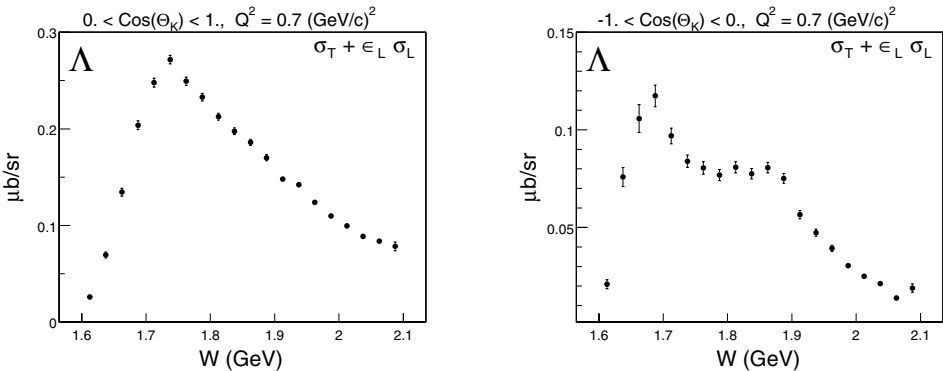


Fig. 38. Cross-section from CLAS for $K^+\Lambda$ electroproduction at $Q^2 = 0.7 \text{ GeV}^2$ integrated over to the forward hemisphere (left panel) and backward hemisphere (right panel) in the center-of-mass angle θ_K^* .

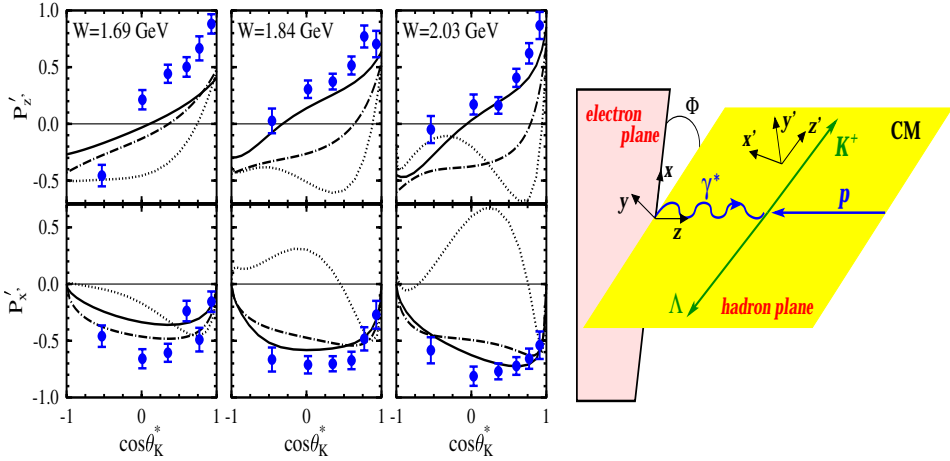


Fig. 39. Left: Transferred Λ polarization in electroproduction from CLAS. The data have been integrated over all ϕ angles. The curves are discussed in the text. Right: Coordinate system defining the Λ polarization projections. The curves are predictions of models in Ref. 81 (dotted), Ref. 193 (solid), and Ref. 194 (dot-dashed).

Figure 39 displays the data of the transferred Λ polarization integrated over all Q^2 for three bins in W . The considered $P'_{x'}$ and $P'_{z'}$ are the projections of the polarization vector \vec{P}' onto the x' and z' axes which are also defined in Fig. 39. The data show that the z' -polarization is large and is rising with $\cos\theta_K^*$, indicating a t-channel mechanism. On the other hand, the x' polarization is large and remains negative throughout the angular range. None of the displayed theoretical results from tree-diagram models^{81,193,194} and a Regge model²⁰⁰ can give an adequate description of the data.

To summarize, production of $K^+\Lambda$ and $K^+\Sigma^0$ from protons exhibit evidence of s-channel nucleon resonance contributions in the mass range where no N^* or Δ^* resonances have been well established. However, resonances are masked by large t-channel processes. In order to extract reliable information on contributing resonances a better understanding of non-resonant processes is needed. Currently, the most important task is to continue experimentally to establish a broad and solid base of consistent data in the strangeness sector, including extensive differential cross-sections, beam and target polarization asymmetries, and polarization transfer measurements. A “complete” measurement of all observables which is needed to unambiguously extract all helicity amplitudes can be achieved.^{202,203} This requires the use of a polarized photon beam and of a polarized target and the measurement of the hyperon recoil polarization. Experimental effort in this direction will continue with a series of new measurements planned at JLab.¹⁴³ On the theoretical side, a dynamical coupled-channel approach, such as that described in Sec. 4.6, must be developed to interpret the extracted N^* parameters.

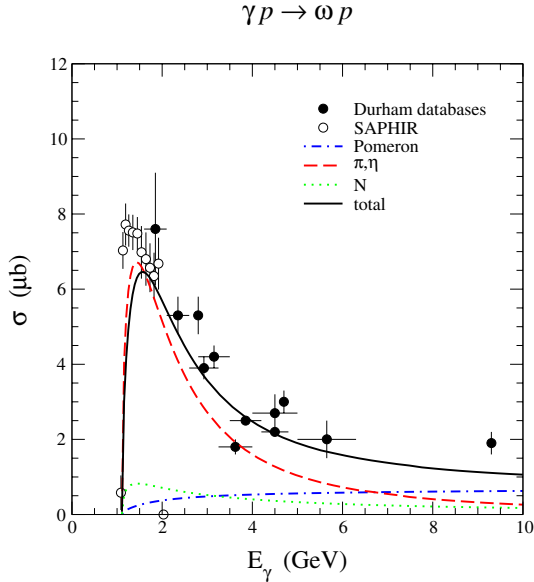


Fig. 40. $\gamma p \rightarrow \omega p$ total cross-sections. The theoretical curves are from the model of Oh, Titov, and Lee.⁸⁶

5.5.3. Photoproduction and electroproduction of vector mesons

The early investigations of photoproduction and electroproduction of vector mesons were mainly in the high energy region where the data can be explained largely by the diffractive Pomeron-exchange mechanism. For the study of nucleon resonances in the $p\omega$ channel, measurements have been performed at ELSA, JLab, and GRAAL to obtain high quality data at energies from production thresholds to $W \sim 2.5$ GeV. In this low energy region, the meson-exchange mechanism plays an important role and must be treated correctly for extracting N^* resonance parameters from the data. This is illustrated in Fig. 40. We see that the diffractive Pomeron-exchange (dash-dotted curve) becomes negligible at energies near ω photoproduction threshold. The s- and u-channel nucleon terms, and π and η exchanges can account for the main part of the total cross-section. The results shown in Fig. 40 are from the tree diagram model described in Sec. 4.2 and no N^* excitations are included.

We will here only describe the status of ω photoproduction in the resonance region ($W < 2.5$ GeV). The ρ production will not be discussed since ρ 's width is very broad and the coupling of the ρN channel to N^* states can be meaningfully defined only in the analysis involving two pion production channels discussed in Sec. 5.4. The ϕ photoproduction will also not be covered here since the ϕ meson has little, if any, contributions from s-channel resonances, as the $s\bar{s}$ quark structure of the ϕ makes $N^* \rightarrow N\phi$ an OZI forbidden decay.

Quark models that also couple to hadronic channels predict that ω photoproduction off protons is a promising tool in the search for undiscovered N^* states.^{101,100}

As in the case of $N\eta$ and $K^+\Lambda$, the $p\omega$ final state, due to the isoscalar nature of the ω , is only sensitive to isospin $\frac{1}{2}N^*$ resonances. Experimentally, $p\omega$ production has been measured in both magnetic detectors and in neutral particle detectors. In magnetic detectors the $p\omega$ channel is usually identified through the $\omega \rightarrow \pi^+\pi^-\pi^0$ decay. This channel has a 89% branching ratio. Detectors with large acceptance for the detection of photons allows to use the $\omega \rightarrow \pi^0\gamma$ channel with an 8.5% branching ratio.

Low energy ω photoproduction data have been obtained at ELSA, JLab, and GRAAL. In Fig. 41 we show preliminary differential cross-sections from CLAS in comparison with predictions using the model of Oh, Titov, and Lee.⁸⁶ The model contains contributions from diffractive production, π^0 exchange, and s-channel N^* contributions with the photocouplings from the constituent quark model of Capstick,¹⁰⁰ and the $N^* \rightarrow p\omega$ couplings predicted in the model by Capstick and Roberts.¹⁰¹ At high W and forward angles the cross-section is completely dominated by the t-channel processes, i.e. diffractive and pion-exchange contributions. Resonance contributions are evident at larger angles, and they seem to play an important role in the entire mass range covered by the data. The quark model perhaps underestimates the resonance contributions.

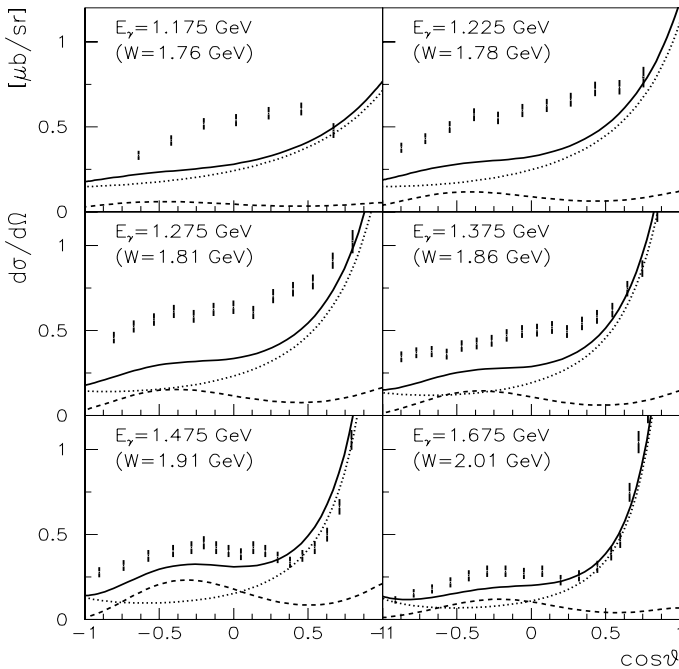


Fig. 41. Differential cross-section for $\gamma p \rightarrow p\omega$ in comparison with model predictions of Oh, Titov, and Lee.⁸⁶ The dotted curves include diffractive production and the $\omega \rightarrow \pi^0\gamma$ vertex. The dashed curves are s-channel resonance contributions using the quark model predictions of Capstick and Roberts.

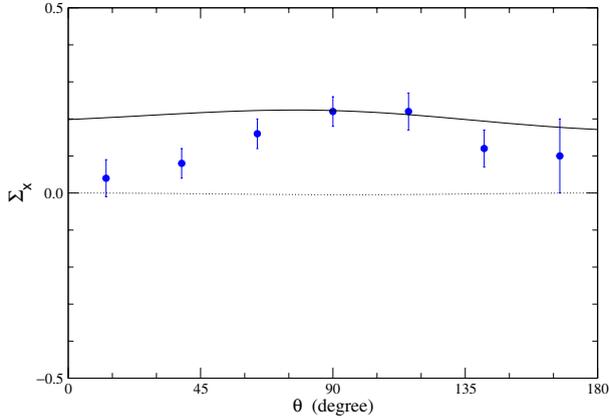


Fig. 42. Photon asymmetry of ω photoproduction at 1.125 GeV. The data (with the sign convention of Ref. 87) are from GRAAL. The dotted curve is from a tree-diagram calculation. The solid curve includes the one-loop coupled-channel effect calculated in Ref. 87.

The theoretical models for investigating low energy ω production are still in the developing stage. Most of the calculations, such as those displayed in Figs. 40 and 41, are based on tree-diagrams models. It has been recognized that coupled-channel effects must be accounted for before the model can be used reliably to extract resonance parameters from the data. The importance of the coupled-channel effects on ω photoproduction has been demonstrated in a one-loop calculation⁸⁷ based on the dynamical coupled-channel formulation Eqs. (52)–(59). As illustrated in Fig. 42, the photon asymmetry at $E_\gamma = 1.125$ GeV can be changed drastically if the coupling with the πN channel is included in the calculation. The K-matrix coupled-channel model of the Giessen group,⁶⁰ based on Eq. (71), has also been used to investigate the data from GRAAL. More effort is needed to improve these theoretical approaches.

5.6. Comments on the search for “missing” baryon resonances

The search for all baryon states predicted by the $SU(6) \otimes O(3)$ constituent quark model is without question of the highest importance for the field. This model has the largest number of excitation degrees of freedom of any quark model based on constituent quarks and must form the basis for this search. Hints of possible new states, even claims of discovery, have been presented in the analyses of single channel processes^{84,160,183,184,201,206} as well as in a coupled-channel analysis.⁶⁰

The analysis of the Giessen group is currently the most extensive in searching for new states. They employ a coupled-channel K-matrix model, as described in Sec. 4.4.2, and include all available pion and real photon induced reaction channels, γN , πN , $N\pi\pi$, $N\eta$, $K\Lambda$, $K\Sigma$, $N\omega$. This analysis finds evidence for several new states. While there are clear indications of new resonances near 1900 MeV in some data sets, various analyses do not allow one to draw definite conclusions on the partial

waves that are needed to explain the data. The Giessen model may be the most promising approach in the search for new states. However, the large amount of data fitted simultaneously with many fit parameters involved makes it difficult to assess the systematic uncertainties in the fit. The dynamical model approaches should be complemented by more experiment-oriented techniques as the one described in Sec. 5.4. Here the binning of data and the evaluation of one-dimensional projections of the multi-dimensional parameter space is replaced by an event-by-event analysis in specific partial waves that retains the correlations in the data for all variables. Theoretical efforts are needed to provide realistic background amplitudes that could strengthen the reliability of these techniques.

6. Concluding Remarks and Outlook

In the past few years, we have witnessed very significant progress in the study of N^* physics. We now have fairly extensive data for π , η , K , ω and $\pi\pi$ production channels. Much more data will soon be available. The theoretical models for interpreting these new data and/or extracting the N^* parameters have also been developed accordingly.

From the analyses of the single pion data in the Δ region, quantitative information about the $\gamma N \rightarrow \Delta$ transition form factors have been obtained. With the development of dynamical reaction models, the role of pion cloud effects in determining the Δ excitation has been identified as the source of the long-standing discrepancy between the data and the constituent quark model predictions. Moreover, the Q^2 -dependence of the $\gamma N \rightarrow \Delta$ form factors has also been determined up to about $Q^2 \sim 6$ (GeV/c)² and found to be in good agreement with the predictions from a dynamical model. The extracted M1, E2 and C2 $\gamma N \rightarrow \Delta$ transition form factors should be considered along with the proton and neutron form factors as benchmark data for testing various hadron models as well as Lattice QCD calculations.

The combined analyses of the π and η production data had led to a rather quantitative, perhaps nearly model independent, determination of several N^* parameters in the second resonance region. However, a correct interpretation of the extracted N^* parameters in terms of the current hadron model predictions requires a rigorous investigation of the dynamical coupled-channel effects which are not included in the employed amplitude analyses based on either the K-matrix isobar model or the dispersion relations approach.

The analyses of the K , $\pi\pi$ and ω channels are still in the developing stage. So far, most of the analyses are based on the tree-diagram models with the isobar parameterization for the N^* excitations. The final state interactions, as required by the unitarity condition, are either neglected completely or calculated perturbatively using effective Lagrangians. The coupled-channel K-matrix effective Lagrangian model, pioneered by the Giessen Group, looks very promising for extracting the N^* parameters from a combined analysis of all channels. But much work is needed to

reduce the uncertainties in their non-resonant parameters and to account for the $\pi\pi N$ unitarity condition. For a rigorous interpretation of the extracted resonance parameters in terms of predictions from hadron models or Lattice QCD calculations, the analyses based on the dynamical coupled-channel model, as given in Sec. 4, are indispensable. Progress is being made in this direction.

In the search for new baryon states, progress is being made in developing partial wave analysis procedures that make full use of correlations in the multi-dimensional phase space presented in the complex final states. This effort must be supported by the development of the theory to obtain improved descriptions of background contributions to specific partial waves.

To end, we mention that the progress we have made in the past decade resulted from rather close collaborations between experimentalists and theorists. With much more complex data to be analyzed and interpreted, such collaborations must be continued and extended in order to bring the study of N^* physics to a complete success.

Acknowledgments

This work was supported in part by the U.S. Department of Energy, Office of Nuclear Physics, under Contract No. W-31-109-ENG-38, and in part under Contract No. DE-AC05-84ER40150.

References

1. See, for example, J. F. Donoghue, E. Golowich and B. R. Holstein, *Dynamics of the Standard Model* (Cambridge University Press, Cambridge, 1992).
2. See, for example, H. J. Rothe, *Lattice Gauge Theories: An Introduction*, World Scientific Lecture Notes in Physics, Vol. 59 (World Scientific, Singapore, 1997).
3. J. Gasser and H. Leutwyler, *Phys. Reports* **87** (1982) 77.
4. N. Isgur and G. Karl, *Phys. Lett.* **B72** (1977) 109; *Phys. Rev.* **D19** (1979) 2653, *ibid.* **D23** (181) 817; and earlier references therein.
5. S. Capstick and N. Isgur, *Phys. Rev.* **D34** (1986) 2809.
6. D. B. Leinweber, A. W. Thomas, K. Tsushima and S. V. Wright, *Phys. Rev.* **D61** (2000) 074502.
7. S. Aoki *et al.*, *Phys. Rev.* **D60** (1999) 114508; Yoshinobu Kuramashi for the CP-PACS collaboration, hep-lat/9904003.
8. D. B. Leinweber, D. H. Lu and A. W. Thomas, *Phys. Rev.* **D60** (1999) 034014.
9. Y. Chen, S. J. Dong, T. Draper, I. Horváth, F. X. Lee, K. F. Liu, N. Mathur and J. B. Zhang, hep-lat/0306199 (2004).
10. C. Alexandrou *et al.*, arXiv:hep-lat/0307018 (2003).
11. L. Ya. Glozman and D. O. Riska, *Phys. Rept.* **268** (1996) 263.
12. L. Ya. Glozman, Z. Rapp and W. Plessas, *Phys. Lett.* **B381** (1996) 311; B. F. Wagenbrunn *et al.*, *ibid.* **B511** (2001) 33.
13. A. Amghar, B. Desplanques and L. Theussl, *Nucl. Phys.* **A714** (2003) 213.
14. F. Coester and D. O. Riska, *Nucl. Phys.* **A728** (2003) 439; B. Julia-Diaz, D. O. Riska and F. Coester, *Phys. Rev.* **C69** (2004) 035212.
15. S. Boffi *et al.*, *Eur. Phys. J.* **A14** (2002) 17.

16. A. Chodos, R. L. Jaffe, K. Johnson, C. B. Thorn and V. F. Weisskopf, *Phys. Rev.* **D9** (1974) 3471; *ibid.* **D10** (1974) 2599.
17. G. E. Brown and M. Rho, *Phys. Lett.* **B82** (1979) 177; G. E. Brown, M. Rho and V. Vento, *ibid.* **B94** (1979) 383.
18. S. Theberge, A. W. Thomas and G. A. Miller, *Phys. Rev.* **D22** (1980) 2838; *ibid.* **D24** (1981) 216.
19. R. Bijker, F. Iachello and A. Leviatan, *Ann. Phys.* (N.Y.) **236** (1994) 69.
20. R. Friedberg and T. D. Lee, *Phys. Rev.* **D15** (1977) 1694; *ibid.* **D16** (1977) 1096.
21. H. B. Nielsen and A. Patkos, *Nucl. Phys.* **B195** (1982) 137; H. J. Pirner, *Prog. Part. Nucl. Phys.* **29** (1992) 33.
22. G. Eckart and B. Schwesinger, *Nucl. Phys.* **A458** (1980) 620.
23. See review by P. Maris and C. D. Roberts, *Int. J. Mod. Phys.* **E12** (2003) 297.
24. S. Eidelman *et al.*, *Phys. Lett.* **B592** (2004) 1.
25. M. Aguilar-Benitez *et al.* (Review of Particle Physics 1986), *Phys. Lett.* **B170**, 1–350 (1986).
26. H. Feshbach, *Theoretical Nuclear Physics: Nuclear Reactions* (Wiley, New York, 1992).
27. H. A. Grunder, *et al.*, *Nucl. Phys.* **A478** (1988) 831; H. A. Grunder, *ibid.* **A623** (1997) 10.
28. J. Alcorn, *et al.*, *Nucl. Instr. Meth.* **A522** (2004) 294.
29. B. Mecking *et al.*, *Nucl. Instr. Meth.* **A503** (2003) 513.
30. J. Friedrich, H. Herminghaus and T. Walcher, *Phys. Bl.* **47** (1991) 291; T. Walcher, *Prog. Part. Nucl. Phys.* **50** (2003) 503.
31. K. I. Blomqvist *et al.*, *Nucl. Instr. Meth.* **A403** (1998) 263.
32. D. Lohmann *et al.*, *Nucl. Instr. Meth.* **A343** (1994) 494; J. Ahrens (A2 Collaboration), *Int. Workshop on Physics with GeV Electrons and Gamma Rays*, Sendai, Japan, 13–15 February, 2001.
33. S. M. Dolfini *et al.*, *Nucl. Instr. Meth.* **A344** (1994) 571.
34. F. Ghio *et al.*, *Nucl. Instr. Meth.* **A404** (1998) 71.
35. A. D’Angelo *et al.* (for the GRAAL collaboration), *Int. Conf. Structure of Baryons* (BARYONS2002), eds. C. Carlson and B. Mecking, Newport News, Virginia, 3–8 March, 2002 (World Scientific, Singapore, 2002).
36. C. E. Thorn *et al.*, *Nucl. Instr. Meth.* **A285** (1989) 447.
37. A. M. Sandorfi *et al.* (LEGS Spin Collaboration), *AIP Conf. Proc.*, Vol. 675 (2003), pp. 651–655.
38. T. Nakano (LEPS Collaboration), *Mod. Phys. Lett.* **A18** (2003) 208.
39. E. Paul *et al.*, *Prog. Part. Nucl. Phys.* **34** (1995) 201.
40. U. Thoma, in “Excited Nucleons and Hadronic Structure,” *Proc. NSTAR 2000 Conf.*, eds. V. Burkert, L. Elouadrhiri, J. Kelly and R. Minehart (World Scientific, Singapore, 2000).
41. Bjorken and Drell, *Relativistic Quantum Mechanics* (McGraw-Hill, 1964).
42. A. S. Raskin and T. W. Donnelly, *Ann. Phys.* (N.Y.) **191** (1989) 78.
43. W.-T. Chiang, S. N. Yang, L. Tiator and D. Drechsel, *Nucl. Phys.* **A700** (2002) 429.
44. G. Knöchlein, D. Drechsel and L. Tiator, *Z. Phys.* **A352** (1995) 327.
45. M. Pichowsky, C. Savkli and F. Tabakin, *Phys. Rev.* **C53** (1996) 593.
46. A. Donnachie, *High Energy Physics*, Vol. 5, ed. E. H. S. Burhop (Academic Press, 1972), pp. 1–185.
47. F. Chew, M. Goldberger, F. Low and Y. Nambu, *Phys. Rev.* **106** (1957) 1345.
48. R. L. Walker, *Phys. Rev.* **182** (1969) 1729.

49. F. A. Berends, A. Donnachie and D. L. Weaver, *Nucl. Phys.* **B4** (1967) 1; *ibid.* **B4** (1967) 54; *ibid.* **B4** (1967) 103.
50. O. Hanstein, D. Drechsel and L. Tiator, *Nucl. Phys.* **A632** (1998) 561.
51. I. G. Aznauryan, *Phys. Rev.* **C57** (1998) 2727.
52. I. G. Aznauryan, *Phys. Rev.* **C67** (2003) 015209.
53. I. G. Aznauryan, *Phys. Rev.* **C68** (2003) 065204.
54. M. G. Olsson and E. T. Osypowski, *Nucl. Phys.* **B87** (1975) 399; *Phys. Rev.* **D17** (1978) 174.
55. R. M. Davidson and N. C. Mukhopadhyay, *Phys. Rev.* **D42** (1990) 20; R. M. Davidson, N. C. Mukhopadhyay and R. S. Wittman, *ibid.* **D43** (1991) 71.
56. R. A. Arndt, I. I. Strakovsky, R. L. Workman and M. M. Pavan, *Phys. Rev.* **C52** (1995) 2120; R. A. Arndt, I. I. Strakovsky and R. L. Workman, *ibid.* **53** (1996) 430; R. A. Arndt, I. I. Strakovsky and R. L. Workman, *Int. J. Mod. Phys.* **A18** (2003) 449.
57. D. Drechsel, O. Hanstein, S. S. Kamalov and L. Tiator, *Nucl. Phys.* **A645** (1999) 145.
58. D. M. Manley, *Int. J. Mod. Phys.* **A18** (2003) 441.
59. D. M. Manley and E. M. Saleski, *Phys. Rev.* **D45** (1992) 4002.
60. F. Feuster and U. Mosel, *Phys. Rev.* **C58** (1998) 457; *ibid.* **C59** (1999) 460; G. Penner and U. Mosel, *ibid.* **C66** (2002) 055211; *ibid.* **C66** (2002) 055212.
61. R. E. Cutkosky, C. P. Forsyth, R. E. Hendrick and R. L. Kelly, *Phys. Rev.* **D20** (1979) 2839.
62. M. Batinic, I. Slaus and A. Svarc, *Phys. Rev.* **C51** (1995) 2310.
63. T. P. Vrana, S. A. Dytman and T.-S. H. Lee, *Phys. Rept.* **328** (2000) 181.
64. H. Tanabe and T. Ohta, *Phys. Rev.* **C31** (1985) 1876.
65. S. N. Yang, *J. Phys.* **G11** (1985) L200.
66. S. Nozawa, B. Blankenleider and T.-S. H. Lee, *Nucl. Phys.* **A513** (1990) 459.
67. F. Gross and Y. Surya, *Phys. Rev.* **C47** (1993) 703; Y. Surya and F. Gross, *ibid.* **C53** (1996) 2422.
68. T. Sato and T.-S. H. Lee, *Phys. Rev.* **C54** (1996) 2660.
69. T. Yoshimoto, T. Sato, M. Arima and T.-S. H. Lee, *Phys. Rev.* **C61** (2000) 065203.
70. T. Sato and T.-S. H. Lee, *Phys. Rev.* **C63** (2001) 055201.
71. S. S. Kamalov and S. N. Yang, *Phys. Rev. Lett.* **83** (1999) 4494.
72. G.-Y. Chen, S. S. Kamalov, S. N. Yang, D. Drechsel and L. Tiator, *Nucl. Phys.* **A723** (2003) 447.
73. S. S. Kamalov, S. N. Yang, D. Drechsel, O. Hanstein and L. Tiator, *Phys. Rev.* **C64** (2001) 032201(R).
74. W.-T. Chiang, F. Tabakin, T.-S. H. Lee and B. Saghai, *Phys. Lett.* **B517** (2001) 101.
75. M. G. Fuda and H. Alharbi, *Phys. Rev.* **C68** (2003) 064002.
76. T.-S. H. Lee, A. Matsuyama and T. Sato, in preparation.
77. N. Kaiser, P. B. Siegel and W. Weise, *Nucl. Phys.* **A594** (1995) 325; N. Kaiser, T. Waas and W. Weise, *ibid.* **A612** (1997) 297.
78. E. Oset and A. Ramos, *Nucl. Phys.* **A635** (1998) 99.
79. R. A. Adelseck, C. Bennhold and L. E. Wright, *Phys. Rev.* **C32** (1985) 1681.
80. R. A. Adeleck and B. Saghai, *Phys. Rev.* **C42** (1990) 108.
81. R. A. Williams, C. R. Ji and S. R. Cotanch, *Phys. Rev.* **C46** (1992) 1617.
82. J. C. David, C. Fayard, G. H. Lamot and B. Saghai, *Phys. Rev.* **C53** (1996) 2613.
83. Z. Li and B. Saghai, *Nucl. Phys.* **A644** (1998) 345.
84. T. Mart and C. Bennhold, *Phys. Rev.* **C61** (2000) 12201.

85. Q. Zhao, Z. Li and C. Bennhold, *Phys. Rev.* **C58** (1998) 2393; Q. Zhao, *ibid.* **63** (2001) 025203.
86. Y. Oh, A. Titov and T.-S. H. Lee, *Phys. Rev.* **C63** (2001) 025201.
87. Y. Oh and T.-S. H. Lee, *Phys. Rev.* **C66** (2002) 045201.
88. M. Guidal, J. M. Laget and M. Vanderhaeghen, *Nucl. Phys.* **A627** (1997) 645.
89. W.-T. Chiang, S. N. Yang, L. Tiator, M. Vanderhaeghen and D. Drechsel, *Phys. Rev.* **C68** (2003) 045202.
90. J. C. Nacher and E. Oset, *Nucl. Phys.* **A674** (2000) 205.
91. M. Ripani *et al.*, *Nucl. Phys.* **A672** (2000) 220; V. Mokeev *et al.*, *Phys. Atomic Nucl.* **64** (2001) 1292.
92. T.-S. H. Lee, unpublished.
93. A. Kiswandhi, S. Capstick and S. A. Dytman, *Phys. Rev.* **C69** (2004) 025205.
94. M. Goldberger and K. M. Watson, *Collision Theory* (Robert E. Krieger Publishing Company, 1975).
95. C. T. Hung, S. N. Yang and T.-S. H. Lee, *Phys. Rev.* **C64** (2001) 034309.
96. T. deForest and J. D. Walecka, *Adv. Phys.* **15** (1966) 1.
97. E. Amaldi, S. Fubini and G. Furlan, *Springer Tracts in Modern Physics*, Vol. 83 (Springer Verlag, Berlin, 1979).
98. D. H. Lu, S. N. Yang and A. W. Thomas, *Nucl. Phys.* **A684** (2001) 296.
99. M. Araki and I. R. Afnan, *Phys. Rev.* **C36** (1987) 250.
100. S. Capstick, *Phys. Rev.* **C46** (1992) 2864.
101. S. Capstick and W. Roberts, *Phys. Rev.* **C49** (1994) 4570; *ibid.* **D57** (1998) 4301.
102. S. Capstick and W. Roberts, *Phys. Rev.* **D58** (1998) 074011.
103. O. Krehl, C. Hanhart, S. Krewald and J. Speth, *Phys. Rev.* **C62** (2000) 025270.
104. D. Schwela and R. Weizel, *Z. Phys.* **221** (1969) 71.
105. J. B. Bell, *Phys. Rev.* **124** (1961) 2014.
106. R. Omnes, *Nuovo Cim.* **8** (1958) 316.
107. R. L. Crawford, *Nucl. Phys.* **B97** (1975) 125.
108. F. Foster and G. Hughes, *Rept. Prog. Phys.* **46** (1983) 1445.
109. B. Krusche and S. Schadmand, *Prog. Part. Nucl. Phys.* **51** (2003) 399.
110. G. Blanpied *et al.*, *Phys. Rev.* **C61** (2000) 024604.
111. R. Beck *et al.*, *Phys. Rev. Lett.* **78** (1997) 606; R. Beck *et al.*, *Phys. Rev.* **C61** (2000) 035204.
112. J. Ajaka *et al.*, *Phys. Lett.* **B475** (2000) 372; O. Bartalini *et al.*, *ibid.* **B544** (2002) 113.
113. J. Ahrens *et al.*, *Phys. Rev. Lett.* **84** (2000) 5950.
114. J. Ahrens *et al.*, *Phys. Rev. Lett.* **88** (2002) 232002.
115. A. Arndt *et al.*, NSTAR 2001, *Proceedings of the Workshop on the Physics of Excited Nucleons*, eds. D. Drechsel and L. Tiator (World Scientific, Singapore, 2001), p. 467.
116. V. Frolov *et al.*, *Phys. Rev. Lett.* **82** (1999) 45.
117. G. Laveissière *et al.*, nucl-ex/0308009 (2003).
118. P. Stoler *et al.*, JLab Experiment E-01-002 (2002); P. Stoler, *Phys. Rev. Lett.* **91** (2003) 172303.
119. H. Breuker *et al.*, *Z. Phys.* **C13** (1982) 113; H. Breuker *et al.*, *Nucl. Phys.* **B146** (1978) 285.
120. J. C. Alder *et al.*, *Nucl. Phys.* **B99** (1975) 1.
121. E. Evangelides *et al.*, *Nucl. Phys.* **B71** (1974) 381.
122. H. Breuker *et al.*, *Z. Phys.* **C17** (1983) 121.

123. J. V. Morris *et al.*, *Phys. Lett.* **B73** (1978) 495; J. V. Morris *et al.*, *ibid.* **B86** (1979) 211.
124. H. Egiyan *et al.* (CLAS Collaboration), *Workshop on the Physics of Excited Nucleons*, Pittsburgh, Pennsylvania, 9–12 October, 2002, eds. S. A. Dytman and E. S. Swanson (World Scientific, Singapore, 2002); H. Egiyan *et al.* (CLAS collaboration), to be submitted to *Phys. Rev. C*, (2004).
125. K. Joo *et al.* (CLAS collaboration), *Phys. Rev. Lett.* **88** (2002) 122001.
126. K. Joo *et al.* (CLAS collaboration), *Phys. Rev.* **C68** (2003) 032201.
127. P. Bartsch *et al.*, *Phys. Rev. Lett.* **88** (2002) 142001.
128. C. Kunz *et al.* (OOPS collaboration), *Phys. Lett.* **B564** (2003) 21.
129. K. Joo *et al.* (CLAS collaboration), *International Conference on the Structure of Baryons* (BARYONS2002), Newport News, Virginia, 3–8 March, 2002, eds. C. Carlson and B. Mecking (World Scientific, Singapore 2002).
130. R. Gothe, *Workshop on the Physics of Excited Nucleons*, Pittsburgh, Pennsylvania, 9–12 October, 2002, eds. S. A. Dytman and E. S. Swanson (World Scientific, Singapore, 2002).
131. V. Burkert, R. Minehart, P. Stoler, M. Taiuti *et al.*, JLab experiment E01-002 (2001).
132. P. Bosted, V. Frolov, M. Jones, V. Kubarovski, P. Stoler *et al.*, JLab experiment E99-107 (1999).
133. S. Frullani, J. Kelly, A. Sarty *et al.*, JLab experiment E99-011 (1991).
134. R. De Vita *et al.* (CLAS Collaboration), *Phys. Rev. Lett.* **88** (2002) 082001-1.
135. A. Biselli *et al.*, *Phys. Rev.* **C68** (2003) 035202;
136. A. Biselli *et al.* (CLAS collaboration), to appear in *Proc. NSTAR2004 Workshop*, Grenoble, France, March 24–27, 2004.
137. L. Tiator *et al.*, nucl-th/0310041
138. L. C. Smith (for the CLAS collaboration), talk presented at the NSTAR2004 workshop, March 24–27, 2004, Grenoble, France.
139. I. Aznauryan, V. Burkert, H. Egiyan, K. Joo, R. Minehart and L. C. Smith, nucl-th/0407021 (2004).
140. C. S. Armstrong *et al.*, *Phys. Rev.* **D60** (1999) 052004.
141. M. Dugger *et al.* (CLAS collaboration), *Phys. Rev. Lett.* **89** (2002) 222002.
142. V. Crede *et al.* (CB-ELSA collaboration), arXiv:hep-ex/0311045 (2003).
143. F. Klein *et al.*, JLab Experiment E02-112.
144. D. Rebreyend, *Proceedings of NSTAR 2002*, Pittsburg, 2002, eds. S. A. Dytman and E. S. Swanson (World Scientific, Singapore, 2003).
145. V. Kuznetsov, private communication.
146. J. Ahrens *et al.* (A2 collaboration), *Eur. Phys. J.* **A17** (2003) 241.
147. B. Krusche *et al.*, *Phys. Rev. Lett.* **74** (1995) 3736.
148. A. Bock *et al.*, *Phys. Rev. Lett.* **81** (1998) 534; J. Price *et al.*, *Phys. Rev.* **C51** (1995) 2283.
149. R. A. Arndt, I. I. Strakovsky and R. L. Workman, *Phys. Rev.* **C53** (1996) 430.
150. R. Thompson *et al.* (CLAS collaboration), *Phys. Rev. Lett.* **86** (2001) 1702.
151. F. Renard *et al.*, *Phys. Lett.* **B258** (2002) 215.
152. J. Ajaka *et al.*, *Phys. Rev. Lett.* **81** (1998) 1797.
153. H. Denizli *et al.*, *Int. Conf. Structure of Baryons* (BARYONS2002), Newport News, Virginia, 3–8 March, 2002, eds. C. Carlson and B. Mecking (World Scientific, Singapore, 2002).
154. G. Höhler, *PiN Newslett.* **14** (1998) 168.
155. N. Kaiser, P. B. Siegel and W. Weise, *Phys. Lett.* **B362** (1995) 23.
156. S. J. Dong *et al.*, arXiv:hep-ph/0306199 (2003).

157. *Workshop on the Physics of Excited Nucleons*, Pittsburgh, Pennsylvania, 9–12 October, 2002, eds. S. A. Dytman and E. S. Swanson (World Scientific, Singapore, 2002).
158. W.-T. Chiang *et al.*, *Phys. Rev.* **C68** (2003) 045202.
159. W.-T. Chiang, S. N. Yang, L. Tiator and D. Drechsel, *Nucl. Phys.* **A700** (2002) 429.
160. B. Saghai and Z. P. Li, *Eur. Phys. J.* **A11** (2001) 217.
161. J.-C. Alder *et al.*, *Nucl. Phys.* **B91**(1975) 386.
162. W. Brasse *et al.*, *Nucl. Phys.* **B139** (1978) 37; *Z. Phys.* **C22** (1984) 33.
163. U. Beck *et al.*, *Phys. Lett.* **B51** (1974) 103.
164. H. Breuker *et al.*, *Phys. Lett.* **B74** (1978) 409.
165. R. A. Arndt, I. I. Strakovsky and R. L. Workman, *Phys. Rev.* **C53** (1996) 430.
166. R. A. Arndt, W. J. Briscoe, I. I. Strakovsky and R. L. Workman, *Phys. Rev.* **C66** (2002) 055213.
167. R. Workman, A. R. Arndt and I. I. Strakovsky, *Phys. Rev.* **C62** (2000) 048201.
168. P. Koniuk and N. Isgur, *Phys. Rev.* **D21** (1980) 1868.
169. P. Koniuk and N. Isgur, *Phys. Rev. Lett.* **44** (1980) 845.
170. Z. P. Li, V. Burkert and Zh. Li, *Phys. Rev.* **D46** (1992) 70.
171. Y. M. Warns, H. Schröder, W. Pfeil and H. Rollnik, *Z. Phys.* **C45** (1990) 627.
172. S. Capstick and B. D. Keister, *Phys. Rev.* **D51** (1995) 3598.
173. F. Cardarelli and S. Simula, *Phys. Rev. Lett.* **62** (2000) 06520.
174. M. Giannini, E. Santopinto and A. Vassallo, *Prog. Part. Nucl. Phys.* **50** (2003) 263.
175. F. Cano and P. Gonzalez, *Phys. Lett.* **B431** (1998) 270.
176. F. E. Close and Z. P. Li *Phys. Rev.* **D42** (1990) 2194.
177. V. Burkert, R. De Vita, M. Battaglieri, V. Mokeev and M. Ripani, *Phys. Rev.* **C67** (2003) 035204.
178. A. J. G. Hey and J. Weyers, *Phys. Lett.* **48B** (1974) 69.
179. W. N. Cottingham and I. H. Dunbar, *Z. Phys.* **C2** (1979) 41.
180. F. E. Close, *An Introduction to Quarks and Partons*, Academic Press/London (1979).
181. V. Burkert *et al.* (CLAS Collaboration), JLab experiment E099-108 (1999).
182. U. Thoma, *Workshop on the Physics of Excited Nucleons*, Pittsburgh, Pennsylvania, 9–12 October, 2002, eds. S. A. Dytman and E. S. Swanson (World Scientific, Singapore, 2002).
183. M. Ripani, V. D. Burkert, V. Mokeev *et al.* (CLAS Collaboration), *Phys. Rev. Lett.* **91** (2003) 022002.
184. V. I. Mokeev *et al.*, *Proc. NSTAR2004 Conference*, Grenoble, March 24–27, 2004, to be published in World Scientific.
185. M. Bellis *et al.* (CLAS collaboration), to appear in *Proc. NSTAR2004 Workshop*, March 24–27, 2004, Grenoble, France.
186. M. Q. Tran *et al.*, *Phys. Lett.* **B445** (1998) 20.
187. Y. Assafiri *et al.*, *Phys. Rev. Lett.* **90** (2003) 222001.
188. M. Wolf *et al.*, *Eur. Phys. J.* **9** (2000) 5.
189. F. Harter *et al.*, *Phys. Lett.* **B401** (1997) 229.
190. V. Mokeev *et al.*, *Phys. Atom. Nucl.* **64** (2001) 1292.
191. V. Burkert *et al.*, *Phys. Atom. Nucl.* **66** (2003) 2149.
192. H. Haberzettl, C. Bennhold and W. Mart, *Phys. Rev.* **C58** (1998) 40.
193. W. Mart, C. Bennhold and H. Haberzettl, *PiN Newslett.* **16** (2002) 86.
194. S. Janssen, J. Ryckebusch, D. Debruyne and T. V. Cauteren, *Phys. Rev.* **C65** (2001) 015201.
195. K. H. Glander *et al.*, *Eur. Phys. J.* **A19** (2004) 251.

196. J. W. C. Mc Nabb *et al.* [CLAS Collaboration], *Phys. Rev.* **C69** (2004) 042201, arXiv:nucl-ex/0305028.
197. G. Niculescu (CLAS Collaboration), *International Conference on the Structure of Baryons* (BARYONS2002), Newport News, Virginia, 3–8 March, 2002, eds. C. Carlson and B. Mecking (World Scientific, Singapore, 2002).
198. M. Mestayer *et al.* (CLAS Collaboration), *Proceedings of PANIC'99*, Uppsala, 10–16 June, 1999, eds. G. Fäldt, B. Höistad and S. Kullander (Elsevier, 1999).
199. D. S. Carman *et al.* (CLAS Collaboration), *Phys. Rev. Lett.* **90** (2003) 131804.
200. M. Guidal, J. M. Laget and M. Vanderhaeghen, *Phys. Rev.* **C68** (2003) 058201.
201. B. Saghai and Z. P. Li, *Workshop on the Physics of Excited Nucleons*, Pittsburgh, Pennsylvania, 9–12 October, 2002, eds. S. A. Dytman and E. S. Swanson (World Scientific, Singapore, 2002), arXiv:nucl-th/0305004.
202. I. S. Barker, A. Donnachie and J. K. Storrow, *Nucl. Phys.* **B79** (1974) 431.
203. I. S. Barker, A. Donnachie and J. K. Storrow, *Nucl. Phys.* **B95** (1975) 347.
204. P. Eugenio, F. Klein, L. Todor *et al.*, JLab Experiment E02-112.
205. M. Kirchbach, *Mod. Phys. Lett.* **A12** (1997) 3177; M. Kirchbach, *Int. J. Mod. Phys.* **A15** (2000) 1435; M. Kirchbach, M. Moshinsky and Yu. F. Smirnov, *Phys. Rev.* **D64** (2001) 114005; M. Kirchbach, arXiv:nucl-th/0303049 (2003).
206. D. G. Ireland, S. Janssen and J. Ryckebusch, *Phys. Lett.* **B562** (2003) 51.
207. M. F. M. Lutz and E. E. Kolomeritsev, *Nucl. Phys.* **A700** (2002) 193.